



UNIVERSITA' DEGLI STUDI DI FIRENZE
Facoltà di Scienze Matematiche, Fisiche e Naturali
Dipartimento di Astronomia e Scienza dello Spazio

Dottorato di Ricerca in Astronomia (FIS05)
XX ciclo (2005-2007)

**SUSPENSION THERMAL
NOISE ISSUES FOR
ADVANCED GW
INTERFEROMETRIC
DETECTORS**

Matteo Lorenzini

Supervisore

Prof. Ruggero Stanga

Co-Supervisore

Dott. Giovanni Losurdo

Coordinatore del Dottorato

Prof. Claudio Chiuderi

Contents

Introduction	vii
1 Detection of gravitational waves	1
1.1 Gravitational waves	1
1.1.1 Einstein's equation	1
1.1.2 Gravitational waves	2
1.1.3 Emission and luminosity	4
1.1.4 The binary pulsar PSR1913+16	6
1.2 Detection of gravitational waves	7
1.2.1 Resonant bar detectors	10
1.2.2 Interferometric detectors	11
1.3 Sources of gravitational waves	14
1.3.1 Neutron stars	15
1.3.2 Coalescing binaries	16
1.3.3 Supernovae	18
1.3.4 Cosmological background	19
1.4 The Virgo interferometer	20
1.4.1 Noise sources	23
1.4.2 The future generations of detectors	25
Virgo+	26
Advanced Virgo	27
The third generation	28
2 Thermal noise	31
2.1 Fluctuation and dissipation	32
2.1.1 Application to GW interferometers	35
2.2 The loss angle	36
2.3 Harmonic oscillator	38
2.4 The standard anelastic solid	40
2.4.1 Thermoelastic losses	43
2.4.2 Structural losses	45
Phonons and electrons relaxation	46

	Point defects and dislocations	47
2.4.3	Surface effects	48
2.5	Other losses	50
2.5.1	Recoil losses	50
2.5.2	Air losses	51
2.6	Thermal noise in a GW detector	52
2.6.1	Suspension wires	52
	Pendulum mode	52
	Violin and bouncing modes	54
2.6.2	Mirrors	56
2.6.3	Thermal noise budget	58
3	Fused silica fibres	59
3.1	Fused silica suspensions	59
3.1.1	Production of fused silica fibres	61
3.1.2	Characterization of fused silica fibres	66
	A three segments model of the fibres	67
	Bending point measurement	70
	Other mechanical parameters	75
3.2	Conclusions	75
4	Silicon suspensions for third generation detectors	77
4.1	Silicon properties	77
4.1.1	Thermomechanical properties of silicon	78
4.1.2	Micro-pulling down technique	82
	Growth process	83
	Seeding and growth procedure	83
4.2	Loss angle measurement description	86
4.2.1	Measurement principle	86
4.2.2	Experimental apparatus	87
	Vacuum system	87
	Clamping stand	88
	Excitation system	90
	Read-out system	92
	Measurement procedure	92
4.3	Fibre modeling	94
4.3.1	Profile measurement apparatus	94
4.3.2	Modeling the fibre with ANSYS	98
	Profiles	98
	Shadow-projection correction	99
4.4	Etching procedure	101
4.5	Experimental results	104

4.5.1	Loss angle measurements	106
4.5.2	Parameters extraction	109
	Young's modulus	109
	Linear thermal expansion coefficient	110
	Thermal conduction coefficient	111
4.6	Investigation on clamps performances	112
4.6.1	Bending clamp	114
4.6.2	Compensating clamp	119
4.7	Conclusions	121
5	Thermal conductivity measurements	123
5.1	Thermal conductivity of silicon	124
5.2	A thermal conductivity measurement facility	126
5.2.1	Experimental apparatus	127
	Cryostat and vacuum system	127
	Measurement stage	130
	Circuitry and acquisition line	132
5.3	Facility test measurements	133
5.4	The silicate bonding technique	136
5.4.1	Chemistry of the silicate bonding	136
5.4.2	Silicate bonding characteristics	137
5.5	Silicate bonded disks	138
5.5.1	Modified apparatus	139
	Heat sink and support	139
	Temperature sensors	141
	Heater block	142
5.5.2	Measurements	143
5.5.3	Effects of inhomogeneities	144
5.6	Simulations on suitable geometry samples	147
5.7	A facility for the measurement of small displacements	149
5.7.1	Setup	152
5.7.2	Controller Design	155
5.8	Conclusions	162
	Bibliography	163

Introduction

More than 30 years ago, in 1975, R. A. Hulse and J. H. Taylor discovered the binary pulsar PSR1913+16, offering the first indirect observation of the existence of gravitational radiation. In the meanwhile, the interest and the efforts to detect directly the gravitational waves coming from the cosmos have continuously grown, and today several resonant detectors are active and the first generation of interferometric detector is operative. Scientific runs have been already performed from the LIGO and Virgo interferometers, and a simultaneous period of data acquisition has been recently completed.

The interest in directly revealing gravitational radiation is manifold. A very immediate reason is, following the sentence by S. Bonazzola and E. Gourgoulhon, 'because they are there' [1], which in its turn mocks the answer of G. Mallory to the question why to climb Everest. Furthermore, the characteristics of such emission would provide a confirmation to the validity of the General Relativity with respect to alternative gravity theories. Thirdly, the possibility to observe the Universe in a completely new spectrum would permit the birth of a gravitational astronomy, which would complement the traditional channels of observation of the sky, providing direct information about black holes and compact objects in general.

The gravitational waves interferometric detector Virgo [2], realized by a joint Italian-French collaboration, together with LIGO (USA) [3], GEO600 (United Kingdom and Germany) [4] and TAMA (Japan) [5] represent the technological success of the first generation of interferometric detectors. These interferometers will be soon (2009) upgraded exploiting the existing technology to Enhanced LIGO and Virgo+ and will hopefully provide the first detection of gravitational waves coming from astrophysical objects.

In order to reach the conditions for the birth of a gravitational waves astronomy, a further step is needed. The present detectors will be up-

graded with substantial improvements aimed to obtain a reduction of the noise in the whole detection band by a factor 10; the advanced versions of Virgo and LIGO will represent the second generation of gravitational waves detectors. A third generation of completely new interferometers will follow, enhancing further the detection range; the European gravitational waves community is now working on a design study for a gravitational detector called Einstein Telescope. To accomplish each step on this path, the development of new technologies and new ideas must be pursued.

Among the various noise sources entering the sensitivity band of gravitational waves interferometers, thermal noise dominates in a wide frequency interval ranging from about 10 Hz up to 1 kHz; the reduction of this noise contribution requires a careful study of the dissipative characteristics of the materials used for the optics and for the optics suspensions.

This thesis presents the results of experimental activities aimed to develop new optics suspensions with very low thermal noise. In view of Virgo+ and Advanced Virgo, the realization of monolithic fused silica suspensions is a main issue in thermal noise reduction: we present our results concerning the production and characterization of suitable fused silica fibres. The third generation of detectors will adopt a cryogenic approach; silicon monolithic suspensions will optimally fit the requirements for cryogenic conditions. We performed measurements of the thermomechanical behaviour of silicon specimens in order to enhance our knowledge of the possibilities offered by silicon.

In the first chapter of the thesis, the problem of detection of gravitational waves coming from astrophysical objects by interferometric, ground-based interferometers is presented, paying a particular attention to the case of Virgo. A brief review of the foreseen upgrades of Virgo and of the main characteristics of the second and third generations is also given. The main features of the mechanical thermal noise, from the fluctuation-dissipation theorem to the noise contributions in Virgo, are discussed in the second chapter. The activity on fused silica fibres is presented in chapter three. In chapter four, an experimental study of the dissipative behaviour of silicon fibres to be used as suspensions elements is described. Finally, thermal conductivity measurements in silicon and in silicon to silicon silicate bonded samples, relevant for a cryogenic suspension assembly, are reviewed and discussed in the last chapter.

Chapter 1

Detection of gravitational waves

In this chapter, the theoretical framework for the study of the gravitational waves is presented. In the second part of the chapter, the two main ground-based methods for the detection of gravitational waves, i.e. interferometers and resonant bars, are treated, and a review of the possible astrophysical sources is given. Finally, the case of the Virgo interferometer is faced, with a sketch of the improving schemes of its second and third generation descendants.

1.1 Gravitational waves

1.1.1 Einstein's equation

Since the beginning of physics and experimental science, the geometrical characteristics of space have been thought as absolute; the cartesian frame in three-dimensional space was originally conceived as an hosting structure for the phenomena, having no interactions with them. Apart, a similar absolute, non interacting time coordinate has been introduced. In this picture, two aspects are present at the same time: on one hand, a formal geometrical parametrization of the place and time of the event, on the other hand, a quantitative description of the interactions involved in the event by means of force laws.

The Einstein's General Relativity Theory (1916) postulates instead a geometric approach to the gravitational interactions and in this respect it operates a synthesis among the two aspects.

In Einstein's theory, the equation of motion for a free point-like mass

in any coordinate framework or *variety* is represented by the system of geodetic equations:

$$\frac{d^2 x^\mu}{ds^2} + \Gamma_{\nu\rho}^\mu \frac{dx^\rho}{ds} \frac{dx^\nu}{ds} = 0 \quad (1.1)$$

where x^μ is the position four-vector, and:

$$\Gamma_{\beta\gamma}^\alpha = \frac{1}{2} g^{\alpha\epsilon} (\partial_\beta g_{\epsilon\gamma} + \partial_\gamma g_{\epsilon\beta} - \partial_\epsilon g_{\beta\gamma}) \quad (1.2)$$

are called *Christoffel symbols* or *connections*. The known quantity in these equations is the metric tensor $g_{\mu\nu}$ of the variety, which defines the infinitesimal length interval:

$$ds^2 = g_{\mu\nu} dx^\mu dx^\nu \quad (1.3)$$

Since the geometry of the variety inherits the characteristics of the gravity field, the metric tensor is related to the dynamical properties of the field. The Einstein field equation allows the metric tensor in the form of the Einstein tensor $G_{\mu\nu}$ to be linked to the dynamical sources represented by the stress-energy tensor $T_{\mu\nu}$ of the matter:

$$G_{\mu\nu} = \frac{8\pi G}{c^4} T_{\mu\nu} \quad (1.4)$$

where $G = 6.673 \times 10^{-11} \text{ m}^3\text{s}^{-2}\text{kg}^{-1}$ is the Newtonian gravitational constant. The Einstein tensor is defined as:

$$G_{\mu\nu} = R_{\mu\nu} - \frac{1}{2} g_{\mu\nu} R \quad (1.5)$$

where $R_{\mu\nu}$ and R are obtained on contraction of the Riemann tensor:

$$\begin{aligned} R_{\beta\gamma\delta}^\alpha &= \partial_\gamma \Gamma_{\beta\delta}^\alpha - \partial_\delta \Gamma_{\beta\gamma}^\alpha + \Gamma_{\gamma\epsilon}^\alpha \Gamma_{\beta\delta}^\epsilon - \Gamma_{\delta\epsilon}^\alpha \Gamma_{\beta\gamma}^\epsilon \\ R_{\mu\nu} &= R_{\mu\alpha\nu}^\alpha \\ R &= R_{\mu\mu} \end{aligned} \quad (1.6)$$

1.1.2 Gravitational waves

According to the Special Relativity, any signal cannot carry information at a speed greater than the speed of light c . Therefore, the local perturbations of the metric structure of space-time cannot propagate instantaneously; they are carried by gravitational waves [6] which travel at

the speed of light¹. The shape of such waves can be calculated in the General Relativity framework if the far field hypothesis is assumed.

The effect of the gravity field in vacuum, far from the source, is small enough for a perturbative approach to be pursued (as for example in [7]) of the Einstein field equations (*Weak Field Approximation* or WFA). Consider thus a small perturbation $h_{\mu\nu}$ to the flat Minkowski metric tensor $\eta_{\mu\nu}$:

$$g_{\mu\nu} = \eta_{\mu\nu} + h_{\mu\nu} \quad |h_{\mu\nu}| \ll 1 \quad (1.7)$$

On substituting the expression (1.7) in the field equations in vacuum $G_{\mu\nu} = 0$, then solving at the first order in $h_{\mu\nu}$, one finds:

$$0 = \partial_{\beta\alpha} h_{\delta}^{\alpha} - \partial_{\alpha} h_{\delta\beta} + \partial_{\delta} h_{\alpha\beta} - \partial_{\beta\delta} h_{\alpha}^{\alpha} \quad (1.8)$$

The latter expression can be simplified by operating a gauge transformation. It is convenient indeed to move to a coordinate system in which a freely falling mass (that is, a mass which experiences gravitational forces only) is at rest; in this frame the solution for the metric tensor $h_{\delta\beta}$ is transverse and traceless (*gauge TT* or *Transverse Traceless gauge*), so that:

$$\square h_{\delta\beta} = 0 \quad (1.9)$$

A general solution for this equation can be written in the form:

$$h_{\delta\beta} = A_{\delta\beta} \exp^{ik^{\alpha}x_{\alpha}} \quad (1.10)$$

where $k^{\alpha} = k n^{\alpha}$ is the wave vector. On substituting this solution in equation (1.9) one has:

$$n_{\alpha} n^{\alpha} = 1 - |\vec{n}|^2 = 0 \quad (1.11)$$

showing that the gravitational waves travel at the speed of light. The transverse and traceless gauge choice leads for the tensor $A_{\delta\beta}$ to the form:

$$A_{\delta\beta} = \begin{pmatrix} 0 & 0 & 0 & 0 \\ 0 & h_{+} & h_{\times} & 0 \\ 0 & h_{\times} & -h_{+} & 0 \\ 0 & 0 & 0 & 0 \end{pmatrix} \quad (1.12)$$

¹The assumption that General Relativity holds leads to a massless radiation propagating at c , while alternative gravity theories would rely on massive field mediators leading thus to a radiation with a velocity lower than c

In this expressions, only two free components appear, h_+ and h_\times , corresponding to two possible polarization states of the gravitational wave. Consequently, the wave can be rewritten as:

$$A_{\delta\beta} = h_+ e_{\delta\beta}^+ + h_\times e_{\delta\beta}^\times \quad (1.13)$$

defining the polarization vectors:

$$e^+ = \begin{pmatrix} 0 & 0 & 0 & 0 \\ 0 & 1 & 0 & 0 \\ 0 & 0 & -1 & 0 \\ 0 & 0 & 0 & 0 \end{pmatrix}, \quad e^\times = \begin{pmatrix} 0 & 0 & 0 & 0 \\ 0 & 0 & 1 & 0 \\ 0 & 1 & 0 & 0 \\ 0 & 0 & 0 & 0 \end{pmatrix} \quad (1.14)$$

Consider now a monochromatic wave with angular frequency ω and polarization h_+ , impinging orthogonally on the plane $z = 0$ of a cartesian coordinate system $0xyz$. Near the origin, the deformation pattern induced by the traveling wave is given by:

$$\begin{cases} x = x_0(1 + \frac{h_+}{2} \cos(\omega t)) \\ y = y_0(1 - \frac{h_+}{2} \cos(\omega t)) \end{cases} \quad (1.15)$$

The effect of such deformation on a material ring of radius R centered in the origin is shown in figure (1.1). The pattern of deformation induced by the polarization h_\times is obtained rotating the previous one by an angle $\pi/4$. By superposition of the two polarizations is possible to obtain circular or linear polarization states.

1.1.3 Emission and luminosity

As the emission of electromagnetic waves is due to the acceleration of charged particles, the emission of gravitational radiation is associated with an accelerating mass. Nevertheless, conservation laws for the mass and for the momentum imply that monopole and dipole terms in the gravitational potential energy do not give rise to wave emission.

The first term to generate a gravitational wave is the quadrupole moment [7], [8]:

$$Q_{ij} = \int_V \rho(\vec{x}) \left(x_i x_j - \frac{1}{3} \delta_{ij} r^2 \right) dV \quad (1.16)$$

As a consequence of the quadrupole nature of the gravitational radiation, a spherical distribution of mass cannot produce gravitational waves. This

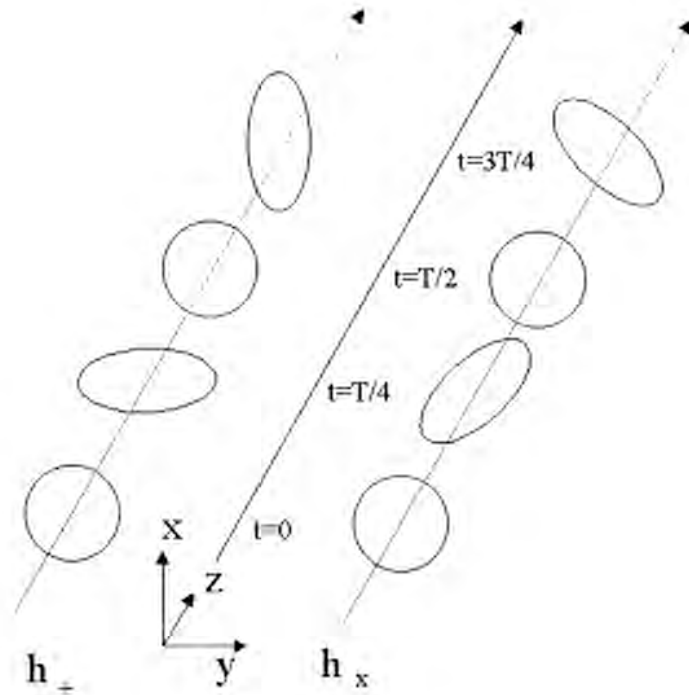


Figure 1.1: Effect of the two polarizations of a monochromatic gravitational wave on a circular mass distribution close to the origin.

is in accord with the Birkhoff's theorem which states that out of a spherical mass distribution, even not stationary, the metric tensor is steady and it is equal to the one produced by the same amount of mass concentrated at the center of the distribution.

The power emitted as gravitational waves (*luminosity*) depends on the third-order time derivative of the quadrupole tensor of the source, according to:

$$\mathcal{L} = \frac{1}{5} \frac{G}{c^5} \langle \ddot{Q}_{ij} \ddot{Q}_{ij} \rangle \quad (1.17)$$

where $\langle \dots \rangle$ indicates the averaged value over period and polarizations.

Equation (1.17) can be used to compute an approximated expression for the gravitational luminosity of a source with mass M and characteristic radius R , having a typical evolution timescale T . The mass distribution asymmetry is measured by a deformation parameter ϵ defined in terms of the principal moments of inertia:

$$\epsilon = \frac{I_{xx} - I_{yy}}{I_{zz}} \quad (1.18)$$

Therefore, the quadrupole moment is:

$$Q \sim \epsilon MR^2 \quad (1.19)$$

and the luminosity:

$$\mathcal{L} \sim \epsilon^2 \frac{G}{c^5} \frac{M^2 R^4}{T^6} = \epsilon^2 \frac{c^5}{G} \left(\frac{R_S}{R}\right)^2 \left(\frac{v}{c}\right)^6 \quad (1.20)$$

In the previous expression a characteristic velocity $v = R/T$ has been introduced; the length scale $R_S = 2GM/c^2$, the Schwarzschild radius, measures the object compactness. An efficient source of gravitational waves, thus, should be highly compact ($\sim R_S$), should possess an high grade of anisotropy ($\epsilon \sim 1$) and evolve at a relativistic rate ($v \sim c$).

The amplitude of the emitted wave at a distance r from the source is:

$$h_{ij} = \frac{2}{r} \frac{G}{c^4} \frac{d^2}{dt^2} Q_{ij} \left(t - \frac{r}{c}\right) \sim \frac{G}{c^4} \frac{E_{SOURCE}}{r} \quad (1.21)$$

being $E_{SOURCE} = \epsilon MR^2/T^2$.

1.1.4 The binary pulsar PSR1913+16

The prediction of the existence of metric deformation waves traveling at the speed of light and originated by mass acceleration was first made by Einstein in 1916 within the General Relativity.

However, the discovery of the binary pulsar PSR1913+16 in 1974 by R. Hulse and J. Taylor [7], [8] provided to the scientific community the first proof, though not direct, of the existence of gravitational waves.

PSR1913+16 binary system includes a pulsar orbiting at high speed (~ 400 Km/s) in the gravity field of a dark companion, with a period of $7^h 45^m$. The system shows the required characteristics for emitting a strong gravitational radiation, therefore it has been studied purposely with the aim of highlighting relativistic effects.

During the observations [9], Hulse and Taylor measured with accuracy the variation of the orbital period P with time. In a classic system, obeying the Keplerian dynamics, the orbital period is a constant of the motion and it constitutes together with the eccentricity and the major orbital axis the Keplerian set of system parameters. Taking into account the relativistic nature of PSR1913+16, other post-Keplerian parameters must be introduced; among them, the period variation rate \dot{P} . The fact that $\dot{P} \neq 0$ indicates that the bonding energy of the two stars flows away by means of some sort of efficient mechanism. One can make the guess that this energy flow is due to the emission of gravitational radiation; it is possible then to predict how should the consequent period variation behave according to the General Relativity.

In figure (1.2) the variation of the orbital period of PSR1913+16 is compared with the prediction based on the Einstein's theory. The very good agreement found provides then a striking evidence of the existence of gravitational radiation, being also a positive test of the General Relativity.

1.2 Detection of gravitational waves

Despite the evidence provided by the study of PSR1913+16 period, up to now no direct observation of gravitational radiation has been obtained.

The simplest way for testing the General Relativity predictions and detecting gravitational waves would definitively be that of producing such waves in a controlled way, in a laboratory. If that would be possible, the radiation characteristics could be optimized for the detection, making the latter as easy as possible.

Imagine thus using as source a massive body realized with two 1 ton masses joined by a 2 m long shaft. The gravitational signal produced when such body rotates around its center at a frequency of 1 kHz turns out [8] to have an amplitude lower by 16 orders of magnitude than the one

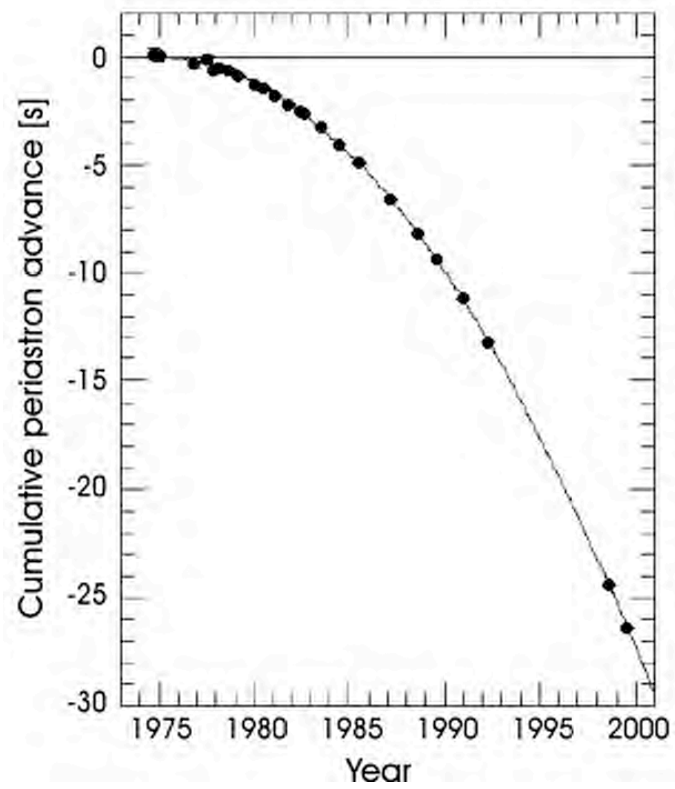


Figure 1.2: Time variation of the orbital period of the binary system PSR1913+16: measured (dots) and General Relativity prediction (line).

predicted to come from astrophysical objects in the near Universe. By all means, the emission of this body would be absolutely not detectable with the presently available techniques.

There are two ways of interpreting phenomenologically the effect of a metric variation h , basically equivalent as long as the linear dimension L of the considered region is negligible with respect to the wavelength of the gravitational signal. These two approaches are related to the chosen local gauge; it is therefore possible to move from the one to the other by gauge transformations.

A first possible choice is that of the TT gauge. In this frame, freely falling bodies are at rest. Consider the variation of distance among two freely falling masses, when a gravitational wave with wavelength λ and polarization h_+ passes. The two masses are placed initially at a distance $L \ll \lambda$ the one from the other, and $L/2$ from the origin. The effect of the wave impinging orthogonally on the $z = 0$ plane where the masses lie is such that:

$$L' \simeq |g_{11}(t, \vec{r} = \vec{0})|^{\frac{1}{2}} L \simeq (1 + \frac{1}{2}h_+(t, \vec{r} = \vec{0})) L \quad (1.22)$$

Therefore, the variation of the distance among the masses is:

$$\Delta L = L \frac{h_{LL}}{2} \quad (1.23)$$

Otherwise, one can use the so called *proper reference frame*, that is, a frame in which the coordinates are fixed with respect to perfectly rigid rules. In this case, the distance among the freely falling masses will vary, provided that the coordinates of the masses vary; a passing gravitational wave makes the masses accelerate, and eventually a tidal force appears according to [7], [8]:

$$F_{tid} = m\ddot{x} = \frac{1}{2} m L \frac{\partial^2 h_{LL}}{\partial t^2} \quad (1.24)$$

The latter is in perfect agreement with equation (1.23), anyway this approach allows a description of the wave effect in terms of forces.

It must be underlined clearly the fact that, while in the TT gauge the coordinates of freely falling objects do not change even when the local metric is changing, in the proper reference frame the observed masses move with respect to the coordinates ticks drawn on perfectly rigid rules.

Following this twofold scheme, the strategies for the detection of gravitational waves belong to two main classes.

1.2.1 Resonant bar detectors

In a resonant bar detector the effect of a gravitational wave is described in terms of a force which is counteracted by the internal elastic forces of the solid bar [10], [11]. The system is therefore similar to a forced harmonic oscillator. Such a detector can be roughly modeled by means of two masses m placed at a distance $2L$ and linked by a spring with elastic constant k . In presence of a monochromatic gravitational wave $h(t) = h_0 \cos(\omega t)$ the equation of motion is:

$$\begin{aligned} m\ddot{x} &= -k(x - L) - \gamma\dot{x} + \frac{1}{2}mL\frac{\partial^2 h}{\partial t^2} \\ &= -k(x - L) - \gamma\dot{x} + \frac{1}{2}mL\omega^2 h_0 \sin(\omega t) \end{aligned} \quad (1.25)$$

In the previous equation, a viscous-like force with coefficient γ has been included.

Bar detectors are made with solid cylinders with very low level of internal friction (see further, chapter (2)), insulated from the environment and left free to vibrate when excited by a gravitational wave; the maximum response is obtained at the mechanical resonance frequency of the bar. The bar vibrations are read by suitable (usually capacitive) sensors. Resonant bars are subject to high levels of noise introduced by the thermal excitation of internal degrees of freedom; thus, resonant cylinders are cooled down at cryogenic temperatures. The sensitivity of such detectors is maximum in a narrow band (few Hz) around the resonance which is usually in the proximity of 1 kHz. Bar detectors have been active in Italy (AURIGA, NAUTILUS, EXPLORER) for many years (and still are), and all around the world (ALLEGRO, NIOBE and others).

Among the resonant bar detectors, a specific case is that of the dual detectors. In this class of detectors, there are two resonant elements, for example a cylinder inserted in a coaxial hollow cylinder. The two elements are characterized by the relevant frequencies ν_1 and ν_2 of their first quadrupole modes. Between the two cylinders, a narrow interspace is left. A gravitational wave with frequency within the interval $[\nu_1, \nu_2]$ causes the two elements to move in phase opposition; in this condition, the amplitude of the thickness variation of the interspace is doubled. This variation is read in a suitable pattern of points making use of capacitive or optical (Fabry-Perot cavities) transducers. An example of such kind of resonant detectors is DUAL [12].

1.2.2 Interferometric detectors

When the gravitational emission is considered in the TT gauge framework, a natural suggestion is to measure ΔL by measuring the travel time of a laser beam between two freely falling bodies.

An interferometric detector of gravitational waves is basically a transducer converting the length variations in a phase variations of the output light. Since the length is measured by the travel time of light among two test masses, the best way for detecting very small displacements is to use a Michelson interferometer with orthogonal arms. The mirrors at the arms ends keep the role of test masses and, to attain the condition of freely falling within the detection frequency range, they are hung to a chain of pendula with low characteristic frequencies, acting as a low-pass filter and assuring an efficient mechanical insulation from the environment. The same trick is used for the beam splitter mirror. In these conditions, General Relativity equations valid for freely falling particles can be applied to the mirrors, thus the travel time τ of the laser beam in an interferometer arm can be computed. Chose then a frame in which the two arms of length L are disposed along the axes x and y , and an impinging gravitational wave has the wave vector along the z axis, that is, $\vec{k} = (0, 0, -k)$. For the sake of simplicity, consider a wave with + polarization and $h_{xx} = -h_{yy} = h \exp^{2\pi i f_g t}$, therefore:

$$\begin{aligned} \tau_x &\simeq \frac{1}{c} \int_0^L dx \left[1 - \frac{1}{2} h_{xx} \left(\frac{x}{c} \right) \right] - \frac{1}{c} \int_L^0 dx \left[1 - \frac{1}{2} h_{xx} \left(\frac{2L-x}{c} \right) \right] \\ &= \tau_0 - \frac{hL}{2\pi i f_g c \tau_0} (\exp^{2\pi i f_g c \tau_0} - 1) \end{aligned} \quad (1.26)$$

where $\tau_0 = 2L/c$ is the classical travel time. Along the y arm, where $h_{yy} = -h_{xx}$, one has:

$$\tau_y \simeq \tau_0 + \frac{hL}{2\pi i f_g c \tau_0} (\exp^{2\pi i f_g c \tau_0} - 1) \quad (1.27)$$

The difference in the travel time among the two arms is the effect of the passing gravitational wave²:

$$\Delta\tau(t) = h(t) \frac{2L}{c} \frac{\sin(\pi f_g \tau_0)}{\pi f_g \tau_0} \quad (1.28)$$

²Actually, the gravitational redshift of the beam light should be also taken into account; nevertheless, in the considered case this effect turns out to be negligible with respect to the metric variation.

For a laser with wavelength λ , the time delay corresponds to a phase lag:

$$\Delta\Phi(t) = h(t) \frac{4\pi L}{\lambda} \text{sinc}(f_g \tau_0) \quad (1.29)$$

The output phase lag depends on the wave frequency f_g ; at low frequencies $f_g \ll 1/\tau_0$ the interferometer response is approximately white:

$$\frac{\Delta\Phi(t)}{h(t)} = \frac{4\pi L}{\lambda} \quad (1.30)$$

At high frequencies, though, the transfer function results in a fading of the signal, depending on an average effect over the wave period. If $L \gg \lambda$, during the light travel across the arm, several waves pass through the detector with a null average effect. On the other hand, the interferometer overall sensitivity increases with increasing L , as in equation (1.23). It is thus necessary to find a tradeoff among the average effect and the high sensitivity request. This leads to a design in which the arms are about 100 km long; such design is unfeasible for ground-based detectors, due both to the prohibitive cost and to the Earth curvature.

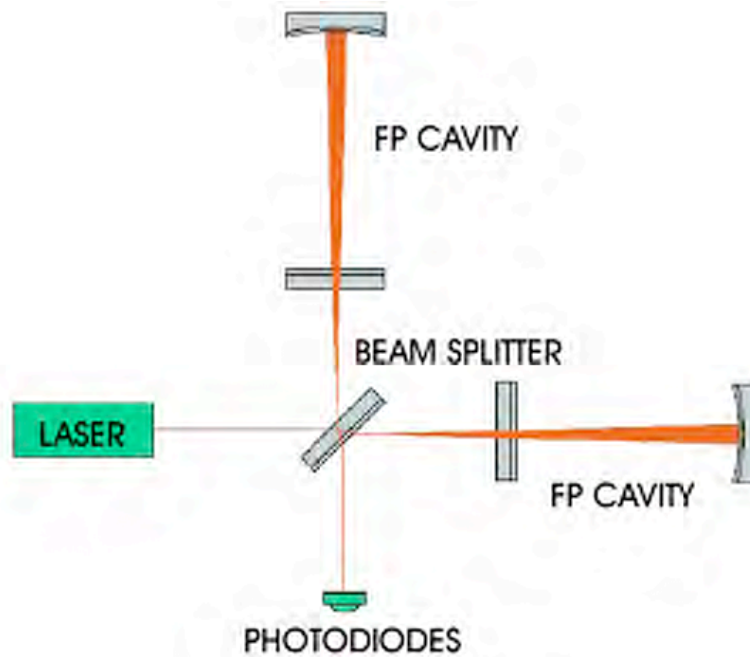


Figure 1.3: Scheme of a Michelson interferometer with Fabry-Perot cavities.

The adopted solution consists in folding the optical path in such a way that affordable arms dimensions are obtained. A specific technique

relies on inserting resonant optical Fabry-Perot (or FP) cavities in place of the classic arms. Two semitransparent mirrors are placed at the input ports of the arms (figure (1.3)). The two cavities are maintained at the resonance condition with the laser frequency; the photons entering the cavities are trapped inside and cover the arm length on average $N = 2F/\pi$ times. The parameter F is called *finesse* and is fixed by the reflectivity r_i of the cavity mirrors:

$$F = \frac{\pi\sqrt{r_1 r_2}}{1 - r_1 r_2} \quad (1.31)$$

or, in the simpler case of a perfect far mirror ($r_2 = 1$):

$$F = \frac{\pi\sqrt{r_1}}{1 - r_1} \quad (1.32)$$

The finesse is related to the cavity storage time, that is, the time needed for the power in an arm, once the laser is switched off, to decrease its value by a factor $1/e$:

$$\tau_s = \frac{1}{4} \frac{2L}{c} \frac{2F}{\pi} \quad (1.33)$$

Using a folding technique, the required optical path can be achieved by arms of few kilometers. The phase transfer function is modified by the introduction of Fabry-Perot cavity; at low frequencies $f_g \ll 1/\tau_0$:

$$\left| \frac{\delta\Phi}{h} \right| = \frac{4\pi L}{\lambda} \frac{2F}{\pi} \frac{1}{\sqrt{1 + (4\pi f_g \tau_s)^2}} \quad (1.34)$$

The folding strategy using Fabry-Perot cavities represents a significative improvement of the interferometric detection technique; nonetheless, it makes the use of an active mirrors positioning control necessary for keeping the cavities at the resonance.

For a displacement $\Delta L = hL/2$ due to a gravitational wave, the light power modulation at the output port of the interferometer is:

$$P_{OUT} = P_{IN} \cos^2 \left(\frac{4r_1}{1 - r_1} k \Delta L \right) \quad (1.35)$$

being $k = 2\pi/\lambda$. To maximize the contrast, defined as:

$$C = \frac{P_{MAX} - P_{MIN}}{P_{MAX} + P_{MIN}} \quad (1.36)$$

the working point of the interferometer is chosen by satisfying:

$$k\Delta L = \frac{\pi}{2} + n\pi \quad (n \in \mathbb{N}) \quad (1.37)$$

that is, in the dark fringe. A control loop acting on mirrors position is realized for locking the interferometer output to the dark fringe. In this condition, though, the sensitivity of the interferometer for a fringe displacement is at its minimum:

$$P_{OUT} = 0 \Rightarrow \frac{\partial P_{OUT}}{\partial \Delta L} = 0 \quad (1.38)$$

To avoid this situation, a heterodyne phase modulation is commonly used: through a small asymmetry in the length of the two arms, it permits to have $\partial P_{OUT}/\partial \Delta L \neq 0$. Then, the detection signal is obtained by the feedback signal of the fringe locking.

Ground-based gravitational waves interferometric detectors have been realized in several countries; the two LIGO interferometers, built at Hanford and Livingston (USA), have 4 km arms, while a third one with 2 km arms is co-located with the main one at Hanford. The Japan experiment TAMA has 300 m arms, GEO600 at Hannover (Germany) has 600 m arms, while the Virgo project in Cascina (PI) representing the joint French-Italian effort, has 3 km arms.

The limit imposed by the phase transfer function to the optical path depends on the chosen detection frequency band. A very long arms detector would possess an high sensitivity at very low frequencies. The LISA project is aimed to realize an interferometric detector with three test masses orbiting in space, near the Earth; the masses will be placed at the vertices of a huge triangle with 1.5×10^6 km side. LISA detection band will range from 10^{-4} Hz up to about 1 Hz.

A network of ground and space based interferometric detector will boost the detection capabilities, while ground-based interferometers and bars will work together in the same frequency region allowing a coincidence analysis of the gravitational signals.

1.3 Sources of gravitational waves

As discussed in section (1.1.3), in order to efficiently emit gravitational radiation, astrophysical objects must be compact, asymmetric and highly relativistic. The Universe provides a variety of such objects.

From an observational point of view it is convenient to group the sources in three classes, depending on the characteristics of the emitted signal. Periodic sources produce a sinusoidal signal with almost constant amplitude over long timescales; typically they are compact, rapidly rotating stars such as neutron stars. Transient sources last for a short period

and represent the effect of catastrophic events like binary stars or black holes coalescence or supernovae. Stochastic sources provide a fluctuating background coming from unresolved transient events and quantum gravity effects; a cosmological gravitational background is also expected to come from the first instants of the Universe.

In the following, the characteristics of the sources which are expected to enter the sensitivity band of ground-based and space-based interferometric detectors are briefly reviewed. A resume of the main sources and their spectra is displayed in figure (1.4).

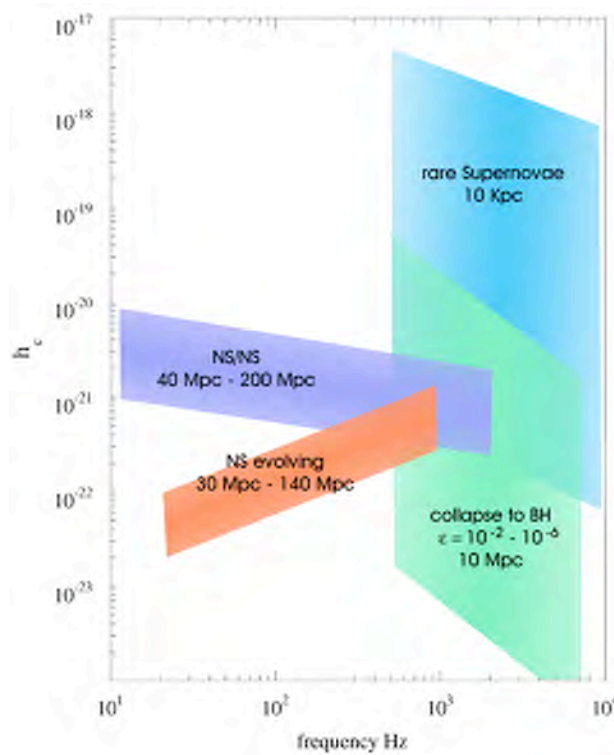


Figure 1.4: Spectrum of gravitational waves astrophysical sources [13]. The abbreviations are: BH, collapse to a black hole; NS/NS, neutron stars coalescence; NS evolving, secular evolution of a non axisymmetric neutron star.

1.3.1 Neutron stars

Neutron stars are compact and rapidly rotating objects, remnants of the catastrophic death of a star (supernova). Typical densities of neutron stars are $\rho \sim 10^{15} \text{ g/cm}^3$, that is, the order of magnitude of the nuclear matter. The typical radius is few tens of km. The magnetic field on

the star reaches very high values and the rotation period is very short, ranging from few seconds down to tens of ms.

A feature of neutron stars is the directional, collimated emission of radio waves, due to the presence of intense magnetic fields in small regions of the surface; together with the rapid rotation, it produces the well known pulsating signal which is at the root of the name *pulsar*.

Within quasi-regular intervals, the period suddenly varies (glitches); this behaviour is thought to be due to quick deformations of the crust of the stars when the object seeks for more symmetrical configurations. This seems to suggest that, at least at the beginning, pulsars do have high conformation asymmetries. The deformation parameter for a common neutron star is expected to be $\epsilon \simeq 10^{-6}$.

The frequency of gravitational radiation expected from such objects is doubled with respect to the rotational frequency (this is an effect of the quadrupole nature of the emission) and the amplitude is given by:

$$h_0 = 4 \times 10^{-24} \left(\frac{1 \text{ ms}}{T} \right) \left(\frac{1 \text{ kpc}}{R} \right) \left(\frac{I}{10^{38} \text{ kg m}^2} \right) \left(\frac{\epsilon}{10^{-6}} \right) \quad (1.39)$$

where ϵ represents the non-axisymmetric ellipticity.

The observed spindown of radio pulsars is presumed to be due primarily to the emission of energetic particles and low frequency electromagnetic waves, nevertheless, the radio waves coming to Earth carry too little energy; therefore, there is room for the possibility that the gravitational emission contributes a significant amount to the spindown process. By entirely addressing the spindown rate to gravitational radiation to set an upper limit to h , one finds that for the Crab pulsar it is of the order of 10^{-24} [14].

Accreting neutron stars can also emit strong gravitational wave signals. Two ways have been suggested for this emission to happen: excitation of unstable normal modes of the rotating neutron star [15], or exchange of precession through the accretion of angular momentum not aligned with the star spin.

1.3.2 Coalescing binaries

A relevant fraction of stars is part of a binary system. A close binary made by two compact stars in fast orbits (white dwarves, neutron stars or black holes) emit a strong gravitational radiation at high frequencies. Consider then a simple model of this system, where the stars are represented by two point-like masses M at a distance $2r_0$, rotating around the

center of mass with angular frequency $\omega = 2\pi f$. One finds [8] that the gravitational emission of the binary system in a direction z orthogonal to the orbital plane, at a distance R , is:

$$h_{xx} = -h_{yy} = \frac{32\pi^2 G}{Rc^4} Mr_0^2 f^2 \cos[2(2\pi f)t] \quad (1.40)$$

$$h_{xy} = h_{yx} = \frac{-32\pi^2 G}{Rc^4} Mr_0^2 f^2 \sin[2(2\pi f)t] \quad (1.41)$$

Note that the angular frequency of the emitted wave is doubled with respect to the orbital angular frequency.

Binary compact stars lose energy by radiating gravitational waves. This implies a shortening of the distance among the two stars and an enhancement of the orbital frequency. Therefore, the two stars spiral toward the common center of mass, giving rise to the coalescence phase; in a time τ called coalescence time the two stars collide and merge together, eventually leaving a single object with radius similar to that of the parent stars. In the final phase of the coalescence the rotation velocity can reach significative fractions of c .

In such extreme conditions, gravitational radiation becomes very strong. The pattern of emission can be computed directly only at the beginning of the coalescence phase, when a Newtonian approximation with two point-like particles can be assumed. The characteristic signal expected in the first phase, called *chirp*, consists in a pulsating signal whose amplitude goes on growing, showing also a frequency sweep. One finds:

$$h_+ = 2(1 + \cos^2(i)) \frac{G\mu M^{\frac{2}{3}}}{Rc^4} \omega^{\frac{2}{3}}(t) \cos(2\omega(t)t) \quad (1.42)$$

$$h_\times = 4 \cos(i) \frac{G\mu M^{\frac{2}{3}}}{Rc^4} \omega^{\frac{2}{3}}(t) \sin(2\omega(t)t) \quad (1.43)$$

In these formulae, i is the angle formed by the line of sight and the orbital plane, M and μ are the total mass and the reduced mass respectively, R is the distance from the source. The orbital angular frequency changes getting closer to the instant t_c when the merging phase starts:

$$\omega(t) = \frac{1}{8} \left(\frac{G\mu M^{\frac{2}{3}}}{5c^5} \right)^{-\frac{3}{8}} (t_c - t)^{-\frac{3}{8}} \quad (1.44)$$

A rough estimation of a chirp signal detected on Earth by a binary system with masses of the order of the Chandrasekhar mass, at a distance $R = 10$ Mpc gives values around 10^{-20} .

An important deduction can be made from the previous expressions. If one measures the time dependence of both frequency and amplitude, the masses can be eliminated thus obtaining an estimation of R [16], [17]. Therefore, binary systems in the coalescing phase can be used as standard candles.

Unfortunately, systems such the one described above are quite rare, and few are the ones known or studied. The recent discovery and observation [18], [19] of the binary pulsars system PSRJ0737-3039 allowed a better knowledge of the physical properties of binary stars close to the coalescence. Presently, about $10 \div 15$ events of such kind per year are expected to take place within a radius of 100 Mpc around the Milky Way. In the case of a double neutron star merging, the expected detection rate for the present day interferometric detectors ranges from about one event every 100 years [20] to about one every ten years [21]. In the case of a pair of black holes, the most optimistic estimations give a rate of the order of one event per year [22].

1.3.3 Supernovae

A transient gravitational signal can be emitted during catastrophic events such stellar explosions or supernovae. The emission is conditioned by the geometry of the explosion: if indeed the matter is expelled in a spherical symmetrical burst the Birkhoff's theorem prevents any metric modification and no gravitational waves are radiated. The emission is possible only if the explosion is asymmetric.

There are mainly three suggested mechanisms [23] for producing a gravitational emission.

The so called *boiling* consists in a temporary instability within the outer layers of the neutron star formed by the supernova event. In this case, about ten gravitational bursts cycles are expected, with an amplitude $h \sim 10^{-24}$ if the source is located at 10 Mpc.

An axisymmetric collapse is expected to produce gravitational waves with low efficiency and intensity $h \sim 3 \times 10^{-24}$ at a distance of 10 Mpc, with a complex frequency spectrum ranging from 200 Hz up to 1 kHz.

A collapse without an axisymmetric component 10 Mpc far from Earth is much more efficient ($h \sim 10^{-21}$).

In terms of amplitude, if a burst of gravitational waves is emitted by a supernova event at a distance R carrying a total energy E predominantly

at a frequency f and spread over a timescale τ one finds [14]:

$$h = 5 \times 10^{-22} \left(\frac{E}{10^{-3} M_{\odot} c^2} \right)^{\frac{1}{2}} \left(\frac{\tau}{1 \text{ ms}} \right)^{-\frac{1}{2}} \times \left(\frac{f}{1 \text{ kHz}} \right)^{-1} \left(\frac{R}{15 \text{ Mpc}} \right)^{-1} \quad (1.45)$$

Supernova events are expected within 10 Mpc with a rate of few per year. If only 1 % of collapses produce a gravitational waves burst carrying 1 % of the available energy, then the present interferometers should see roughly one of such events per year.

1.3.4 Cosmological background

A background of gravitational radiation is predicted by the currently accepted cosmological theories, in analogy with the cosmic microwaves background [13]. The gravitational cosmic background has been produced much before the recombination time, therefore it would carry information about a cosmological time up to now unattained by observations. The gravitational interaction with matter is very weak due to the very low value of the Newtonian constant: even confronting with neutrinos, one has $\sigma_g/\sigma_{\nu} \sim (G/G_F)^2 \sim 10^{-67}$! Therefore, a gravitational fossile background would come from the very early times of the Universe, of the order of Plank time $t \sim 10^{-43}$ s.

A parametrical amplification of gravitational radiation background has been suggested in the inflation period; if there was no enhancement process, the background would be fixed by the condition of thermal equilibrium at the Plank era. This would imply that today the redshifted fossile radiation would have an amplitude as low as $h \sim 10^{-35}$ that is completely undetectable.

Nevertheless, if the early universe contained an initial inhomogeneity with amplitude h_g [13], today it should result:

$$h \sim 10^{-20} \frac{h_g}{f} \quad (1.46)$$

The limit set to h_g by the cosmic microwave observations is $\sim 10^{-5}$. This would imply for the cosmological background an amplitude $\sim 10^{-21}$ at 10^{-4} Hz, which would be accessible to space antennas like LISA.

Observational limits to the gravitational cosmological background at low frequencies can be obtained by binary pulsar systems like PSR1913+16, as discussed in [13].

1.4 The Virgo interferometer

First generation gravitational waves detector Virgo possesses the general design characteristics discussed in section (1.2.2). The design sensitivity curve of Virgo is displayed in figure (1.5); all the main sources of noise are included, as they will be described further on, in section (1.4.1).

A scheme of the functional parts of Virgo is shown in figure (1.6). A peculiar feature of Virgo is the attention paid to filtering the seismic noise. Such a result is obtained by a particular optics suspension strategy; the mirrors are hung to a complex system basically realized with a chain of six pendula fixed at the top to the upper platform of an inverted pendulum. This mechanical filter, called *superattenuator* or SA [24], allows both an active and passive filtering of the seismic noise with an attenuation of about fifteen orders of magnitude at 10 Hz. A picture of the SA is in figure (1.7). The last suspension stage is realized with wires directly attached to the test mass. The mechanical part supporting the last suspension stage is called *marionetta* and hosts part of the actuators for the active positioning of the mirrors when the feedback loop is closed.

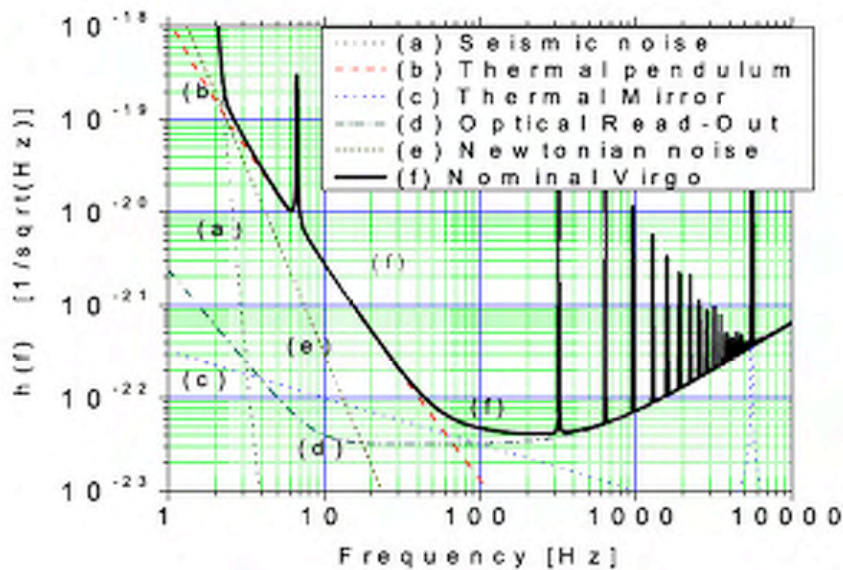


Figure 1.5: Virgo nominal sensitivity curve.

The laser used in the interferometer is a Nd:YVO₄ with wavelength $\lambda = 1064$ nm and power of about 20 Watts. The output is a TEM₀₀

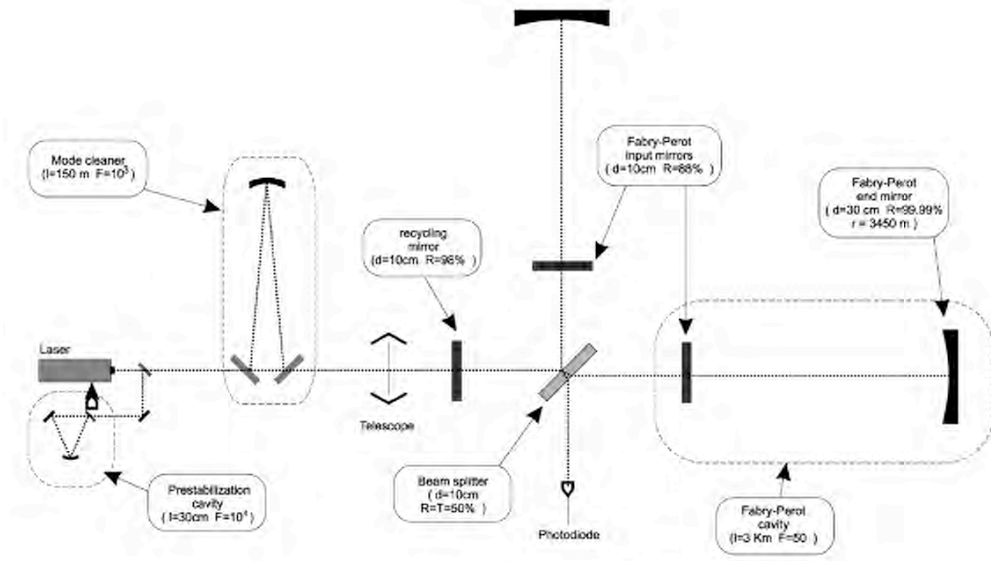


Figure 1.6: A schematic representation of the Virgo optical layout.

mode and the stability requirements are, in power:

$$\frac{\delta P}{P} < \begin{cases} 3 \times 10^{-5}/\sqrt{\text{Hz}} & \text{for } f = 10 \text{ Hz} \\ 3 \times 10^{-7}/\sqrt{\text{Hz}} & \text{for } 110 < f < 1 \text{ kHz} \end{cases} \quad (1.47)$$

and in frequency:

$$\frac{\delta \nu}{\nu} < \begin{cases} 10^{-4}/\sqrt{\text{Hz}} & \text{for } f = 10 \text{ Hz} \\ 10^{-6}/\sqrt{\text{Hz}} & \text{for } 110 < f < 1 \text{ kHz} \end{cases} \quad (1.48)$$

The beam injection is accomplished by an injection bench hung to a SA which holds a triangular reference cavity for the laser frequency pre-stabilization, the input and output mirrors of the mode cleaner and the expansion and alignment optotronics.

The mode cleaner is a triangular 144 m long cavity with the intermediate mirror suspended to a short SA.

After the input bench, the whole laser path is maintained under vacuum, at required residual pressures different for the various gases, ranging from 10^{-9} for hydrogen to 10^{-14} for hydrocarbons. The limit on hydrocarbons is more stringent because of the capability they have to stick on the mirrors surfaces degrading their quality. The high vacuum prevents interactions between the laser beam and matter which would result in power losses and scattering, causing the output noise to increase.

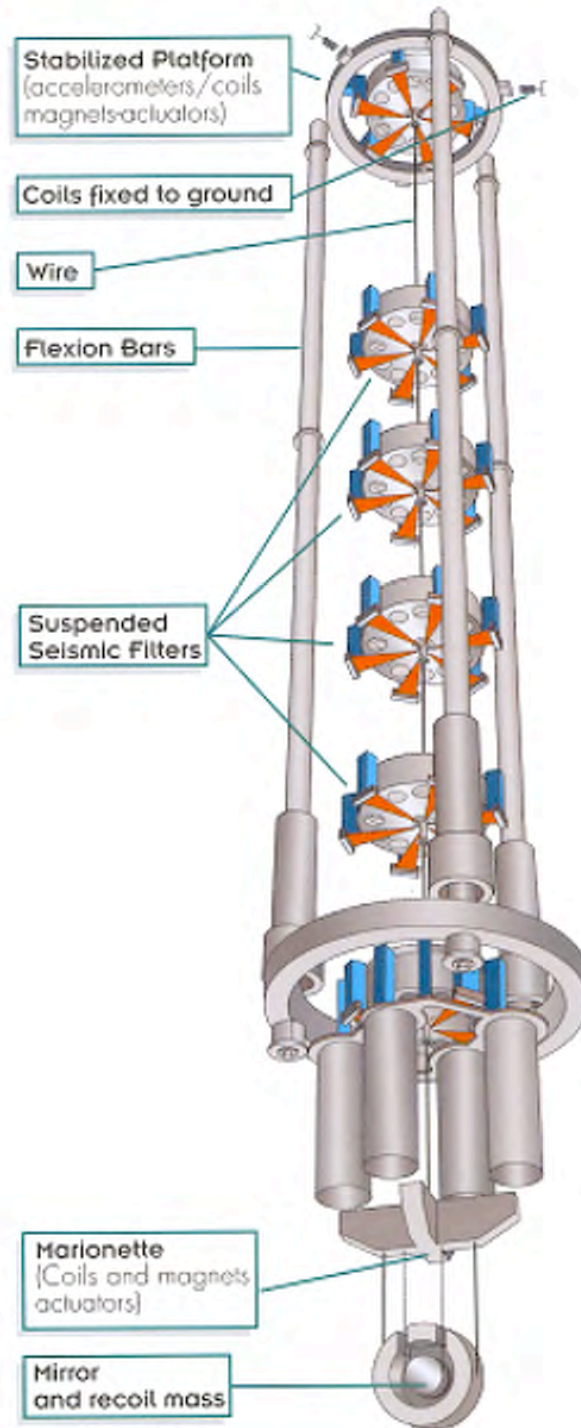


Figure 1.7: A schematic representation of the Virgo superattenuator. A chain of 5 filters (with a horizontal resonant frequency $f_h = 0.45$ Hz and a vertical one $f_v = 0.4$ Hz) is attached to the top of a big tripod, that acts as an inverted pendulum (with $f_h = 30$ mHz). The mirror is hanged through a device called marionette that allows a fine control of its position along the three relevant degrees of freedom.

The Fabry-Perot cavities in Virgo are 3 km long and their finesse is $F = 50$.

The power recycling mirror redirects to the beam splitter part of the light reflected back to the laser increasing the beam power up to a factor 50. This technique permits a reduction of the laser shot noise which limits the sensitivity at high frequencies.

The read-out system is realized with an output mode cleaner in series to the collimating optics delivering the beam onto the acquisition photodiodes.

1.4.1 Noise sources

The Virgo detection system must be designed in such a way to minimize all the possible noise sources which could introduce a spurious contribution to the output, mocking a gravitational signal, or totally cover the physically interesting signals.

Therefore, a large effort has been done in recognizing and understanding the noise sources and in studying their characteristics. The origin of the various kinds of noise can be identified as due to a fluctuation of the mirror position or to the signal read-out noise. The sum of all the power spectra coming from the noise sources expected in Virgo defines the limit to the amplitude of detectable events, and constitutes the sensitivity curve of the detector. These noise contributions are briefly reviewed below.

- **Optical read-out noise**

The optical read-out noise is originated by the sum of two effects related to the quantum behaviour of the light.

The corpuscular nature of light causes the output signal to be affected by shot noise. The shot noise can be treated in analogy with the simple case of the current noise in a diode; it basically depends on the laser input power P_{in} . Call Φ the phase at the output port of the interferometer, and $\delta\Phi$ the phase lag due to a true gravitational signal. Having a SNR of order unity requires that:

$$\delta\Phi \geq 2\sqrt{\frac{h\nu}{\eta P_{in}} \frac{1 + \cos \Phi}{\sin^2 \Phi}} \quad (1.49)$$

being η the efficiency of the photodiode and ν the laser frequency. This expression also confirm that working in dark fringe condition

is convenient: in this case, the right side of the equation is minimum. The shot noise then shows a white frequency spectrum with amplitude:

$$\tilde{h}_{SN} = \frac{1}{4\pi L} \sqrt{\frac{2h\lambda c}{\eta P_{in}}} \quad (1.50)$$

Note that increasing the injected power results in decreasing the shot noise level.

A quantum effect conjugate to the shot noise, the *radiation pressure noise*, is also present, adding its contribution to the overall noise. A mirror reflecting a beam with power P sustains an average force given by $\bar{F} = 2P/c$. Since the beam is constituted by particles (the photons) this force fluctuates. The corresponding fluctuation spectral density is:

$$\delta\bar{F} = \sqrt{\frac{8hP}{\lambda c}} \quad (1.51)$$

inducing a noise at the output equal to:

$$\tilde{h}_{RP} = \frac{1}{ML} \sqrt{\frac{hP_{in}}{2\pi^4 c \lambda}} \frac{1}{f^2} \quad (1.52)$$

where M is the mirror mass. Clearly, the radiation pressure noise can be reduced by reducing the laser power. Nonetheless, recall that the opposite happens to the shot noise; thus, an optimal laser power can be found depending on frequency.

The optical folding by Fabry-Perot cavities modifies the form of expressions (1.50) and (1.52). In this case [8], the total read-out noise is given by:

$$\tilde{h}_{tot}^{FP} = \sqrt{\left(\frac{\pi}{2F}\right)^2 \tilde{h}_{SN}^2 + \left(\frac{2F}{\pi}\right)^2 \tilde{h}_{RP}^2} \quad (1.53)$$

- **Thermal noise**

A fundamental limit to the sensitivity in a wide region just in the middle of the detection band is represented by the *thermal noise* [25]. It is caused by thermal fluctuations of the mechanical degrees of freedom of the suspensions system and of the test mass itself. The next chapter is devoted to a description of the main features and theoretical points regarding the thermal noise, therefore we will not discuss it further in this section.

- **Seismic noise**

Even in the most quiet site, ground movements are far from being null. Seismic solicitations of natural origin or due to the human activity are transmitted to the test masses through the suspensions system, thus injecting noise. Within a good approximation, the displacement spectral density associated to the seismic movements follows the empirical law:

$$S_x^{seismic}(f) = A \cdot \frac{f_0^2}{f^2} \quad (1.54)$$

when $f > 1$ Hz, where $f_0 \simeq 1$ Hz. The constant in equation (1.54) is of the order of $A \sim 10^{-6} \text{ m}\sqrt{\text{Hz}}$. This displacement noise is filtered by the SA over 10 Hz, while below it represents a severe detection limit.

- **Newtonian noise**

The human activity in the proximity of the detector site, as well as seismic waves in the Earth crust, will have another effect on the test masses motion. In fact, moving masses around the detector modify the local gravitational field and this modification is directly transmitted to the mirrors by the field itself. Obviously, this action is not prevented by the suspensions insulation. This purely Newtonian effect is believed to represent a primary contribution to the overall noise at very low frequencies [26].

- **Creep**

The term *creep* refers to the phenomenon of sudden mechanical micro-release of internal stresses in the structures supporting the mirrors. Events of micro-release can simulate gravitational bursts signals.

1.4.2 The future generations of detectors

The first Virgo science run (VSR1) started on May 2007 in coincidence with the last period of the fifth LIGO science run. The achieved sensitivity during the run is presented in figure (1.8); in the frequency region 300 Hz ÷ 5 kHz the goal sensitivity has been reached and it is equal to the LIGO one. Therefore, a joint data analysis among the two interferometers has started. The duty cycle over the run was 81 %. The detector sensitivity expressed as the distance at which a coalescence of

two 1.4 solar masses neutron stars is detectable, averaged on the source direction, attained 4 Mpc.

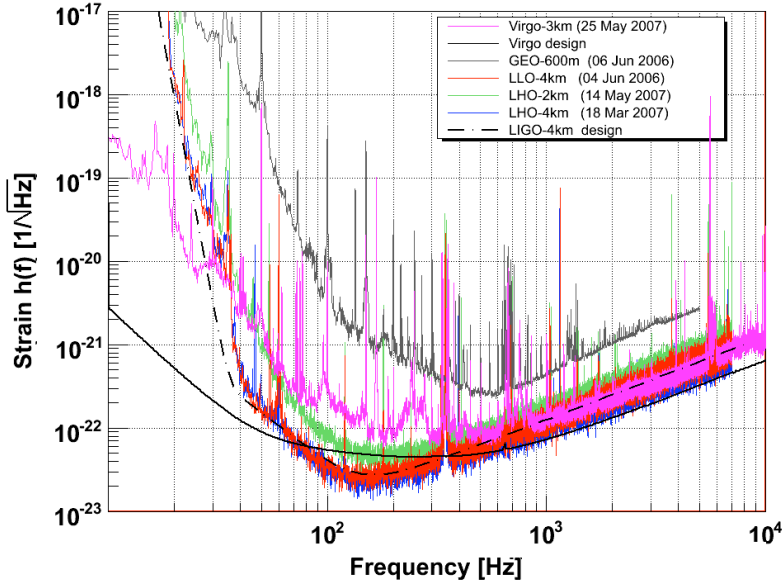


Figure 1.8: Plot of the Virgo sensitivity curve during VSR1 (May 2007), compared with the design one and with the sensitivities of LIGO and GEO600. The design sensitivity of LIGO is also shown.

The sensitivity of current interferometric gravitational waves detectors, though making a first detection possible, would not permit detection statistics. The expected detection rates presented in section (1.3.2) for a double neutron star merging or those for a double black hole coalescence are still quite low, reaching in the most optimistic case one event per year. The first generation detectors performances must be enhanced in order to open the era of gravitational waves astronomy.

The foreseen upgrade of Virgo and the main features of the second generation detector Advanced Virgo are shortly presented here. Also, a general description of a third generation interferometer is given.

Virgo+

An improvement of the current Virgo apparatus doubling the sensitivity will allow an increment of a factor ~ 10 in the detection rate which is proportional to the observable volume.

Virgo has planned a first set of upgrades of the detector, the so called *Virgo+*, to be performed at mid 2009. A similar upgrade (*Enhanced LIGO*) is planned for the LIGO detectors. Since the seismic isolation provided by the SA is compliant with the sensitivity improvement, the main upgrade will concern [27]:

- the installation of a system for the thermal compensation of the heating deformation of mirrors induced by the laser absorption;
- the improvement of the power laser up to 50 Watts by using a new laser amplifier, with the sake of reducing the shot noise at high frequency;
- the installation of new control system electronics;
- the increase of cavity finesse up to 150 with new mirrors;
- the installation of fused silica monolithic suspensions (see chapter (3)).

Advanced Virgo

A more substantial upgrades campaign will take place at the beginning of the next decade when an almost new, second generation detector called *Advanced Virgo* (AdV) will be installed in place of the present one [28]. The aim of AdV is to improve the present sensitivity by one order of magnitude, therefore increasing the detectable events rate by three orders of magnitude.

An higher power laser (200 Watts) will be employed for shot noise reduction. In order to keep the radiation pressure noise at a low level, heavier mirrors (42 kg) will be used. The laser spot on the mirrors will be enlarged in such a way that the thermal noise resulting from the vibrations of the mirror surface will be averaged over a larger area, offering a better performance.

The AdV interferometer dual recycled baseline will include a signal recycling mirror placed at the output port, increasing the power stored in the cavities.

The current research activity on coating thermal noise (see section (2.6.2)) will allow an improvement of the coatings mechanical characteristics, enhancing the sensitivity in the intermediate frequency region. The thermal noise features of AdV will be reviewed further on, in section (2.6.3).

A new control strategy of the SA will be implemented, in order to reduce the impact of bad weather conditions on the detector. In the same frequency region, the suspensions thermal noise will be sensibly reduced by using the monolithic suspension scheme developed for Virgo+.

Finally, the output phase modulation will be replaced by a DC detection scheme. A possible sensitivity curve for AdV is shown in figure (2.3).

The third generation

The plans for realizing a third generation of gravitational waves interferometric detectors are aimed to find strategies for reaching a further reduction (a factor ~ 100 with respect to the present detectors) of noise levels beyond the second generation detectors expectations. The design study of an european observatory called *Einstein Telescope* (ET) is being developed; the main issues are:

- new mirrors, suspensions and coating materials.
- cryogenic approach. Since the thermal noise depends directly on temperature, it can be reduced by cooling the test masses and the suspensions.
- seismic noise and Newtonian noise reduction by choosing a suitable underground location.
- enhancement of the arms length up to 30 km. Different arms geometries are also under consideration.
- higher power lasers and new optic techniques for the suppression of the read-out quantum noise.

Part of the experimental work presented in this thesis is devoted to match the aim of the first two items of this list. A comparative view of the future generations detectors performances is given in figure (1.9).

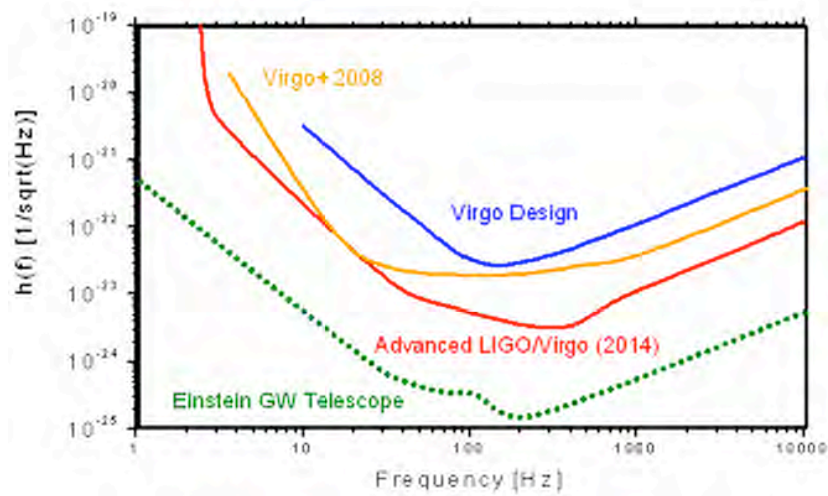


Figure 1.9: Comparative view of the sensitivity curves of future generations detectors. The curve drawn for Advanced Virgo is one among several possible curves depending on the design options. For the Einstein Telescope, a possible curve based on design study considerations is displayed.

Chapter 2

Thermal noise

Thermal excitation of the mechanical degrees of freedom of the test masses, as well as those of the last suspension stage, results in a spurious contribution to the output of an interferometric detector, setting a limit to the sensitivity of first generation GW interferometers in a wide band between few Hz and few 100 Hz. Such contribution has a stochastic nature, so its description is given in terms of power spectra. Thermal noise is a very general fact: it is related to the stability of the thermodynamical equilibrium of a system. The so called fluctuation-dissipation theorem [29], [30], [31], [32] states that, in a linear system, thermally activated equilibrium fluctuations are determined by its dissipative characteristics. Application of this result leads to the evaluation of thermal noise curves for GW interferometers, provided that the dissipation parameters of the materials the masses and suspensions are made of are known. Energy loss measurements are thus needed, together with the characterization of new materials aimed at reducing the thermal noise sensitivity limit.

In this chapter, the theory of thermal noise is briefly reviewed, as it is strictly linked to dissipation in bodies. Therefore, energy dissipation is also discussed; standard models of the behaviour of materials which deviate from pure elasticity are described, together with an overview of the energy loss mechanisms relevant for the argument. Finally, the main thermal noise features for an interferometric GW detector are summarized.

2.1 The fluctuation-dissipation theorem

The attainment of thermodynamical equilibrium in a gas is related to the collisional terms in the dynamic equations; collisions are responsible for the momentum interlinking of the whole system, so they bring the fluid to equilibrium and keep it stable. Such action results in a fluctuation of state variables around equilibrium values, so that their root mean square levels are related to the equipartition energy $k_B T$. Collisions are at the root of viscosity forces in a gas flow, where the frictional momentum transfer is acted by the gas. It turns out naturally that the same process gives rise to equilibrium fluctuations and dissipation; furthermore, the momentum transfer is determined by the velocity distribution of the gas molecules, that is by the temperature.

Brownian motion is a good example [33], [34], [35]. During microscope observations, the eighteenth century botanist R. Brown noticed that pollen grains suspended in water moved with a continuous jittery motion. Such motion, called Brownian in his honour, is proper of small particles immersed in a fluid. It is likely determined by a randomly fluctuating force, due to collisions of the particle with the fluid molecules. Assuming that such unknown force has a constant spectral density¹, it is possible to write the velocity distribution of the particle; equating the resulting energy with the equipartition value, one is able to work out the force.

However, for the Brownian motion as well as in the general case, the spectral density of the fluctuations of a given quantity can be more conveniently obtained by exploiting the discussed link between fluctuation and energy loss. Viscous drag in the fluid, for instance, is the dissipative counterpart of the Brownian jitter. The fluctuation-dissipation theorem allows the spectral density of generalized fluctuating quantities to be determined by knowing the dissipative behaviour of the system. Its formulation correlates an equilibrium property with irreversible processes.

Consider therefore a system² which is dissipative - that is, it can absorb energy if undergoing time-periodic solicitations - and linear, in the sense that the energy lost per unit time is proportional to the square of the solicitation amplitude. The system is supposed to be acted upon

¹Actually, such assumption is somewhat rough, becoming false at high frequencies.

²The following considerations are taken from the original demonstration of the theorem by Callen and Welton [29].

a generalized force \mathcal{V} such that the relevant term in the Hamiltonian is:

$$H_{int} = \mathcal{V}\mathcal{Q} \quad (2.1)$$

\mathcal{Q} being a suitable generalized lagrangian coordinate. The linearity can thus be expressed by introducing the impedance $\mathcal{Z}(\omega)$ as the ratio between the solicitation \mathcal{V} and the system response $\mathcal{R} := \dot{\mathcal{Q}}$ in the frequency domain:

$$\tilde{\mathcal{V}}(\omega) = \mathcal{Z}(\omega)\tilde{\dot{\mathcal{Q}}}(\omega) \quad (2.2)$$

where \tilde{X} indicates the Fourier transform of X .

First look at the dissipation. Suppose the system receives a small monochromatic solicitation $\mathcal{V}(\omega, t) = V_0 \sin(\omega t)$; the Hamiltonian (2.1) can be regarded as a perturbation, and the state of the system can be expanded on the set of unperturbed eigenfunctions. If the energy levels are densely distributed with density $\rho(E)$, the amount of energy lost per unit time (the negative power P) can be computed following the perturbation theory:

$$P = \frac{1}{2}\pi V_0^2 \omega \int_0^\infty \{ |\langle E + \hbar\omega | \mathcal{Q} | E \rangle|^2 \rho(E + \hbar\omega) + |\langle E - \hbar\omega | \mathcal{Q} | E \rangle|^2 \rho(E - \hbar\omega) \} \rho(E) e^{-\frac{E}{k_B T}} dE \quad (2.3)$$

where the temperature T is taken into account by the Boltzmann exponential factor $f(E) = \exp(-E/k_B T)$. On the other hand, the impedance allows the instantaneous power $P_t = \mathcal{V} \dot{\mathcal{Q}} \Re[\mathcal{Z}(\omega)]/|\mathcal{Z}(\omega)|$ to be computed and hence the average power dissipated as:

$$P = \frac{1}{2} V_0^2 \frac{\Re[\mathcal{Z}(\omega)]}{|\mathcal{Z}(\omega)|^2} \quad (2.4)$$

Collecting (2.3) and (2.4) one obtains:

$$R/|\mathcal{Z}|^2 = \pi\omega \int_0^\infty \{ |\langle E + \hbar\omega | \mathcal{Q} | E \rangle|^2 \rho(E + \hbar\omega) + |\langle E - \hbar\omega | \mathcal{Q} | E \rangle|^2 \rho(E - \hbar\omega) \} \rho(E) f(E) dE \quad (2.5)$$

being $R = \Re[\mathcal{Z}]$ the resistance.

Refer now to above considerations about thermodynamical equilibrium. As discussed, in that condition $\dot{\mathcal{Q}}$ undergoes spontaneous fluctuations, which can be thought as being due to a spontaneous fluctuating

force whit a spectral density \mathcal{S}_V^2 to be determined. By means of a calculation of $\langle \dot{Q}^2 \rangle$ on the energy eigenfunctions of the unperturbed Hamiltonian H_0 , one finds:

$$\begin{aligned} \langle E_n | \dot{Q}^2 | E_n \rangle &= \sum_m \langle E_n | \dot{Q} | E_m \rangle \langle E_m | \dot{Q} | E_n \rangle = \\ &= \hbar^{-2} \sum_m \langle E_n | H_0 Q - Q H_0 | E_m \rangle \langle E_m | H_0 Q - Q H_0 | E_n \rangle = \\ &= \hbar^{-2} \sum_m (E_n - E_m)^2 |\langle E_m | Q | E_n \rangle|^2 \quad (2.6) \end{aligned}$$

Introducing $\omega = |E_n - E_m|/\hbar$ and replacing the sum with an integral over ω , then weighting with the Boltzmann factor, one has:

$$\begin{aligned} \langle \dot{Q}^2 \rangle &= \int_0^\infty \hbar \omega^2 \left[\int_0^\infty \rho(E) f(E) \{ |\langle E + \hbar\omega | Q | E \rangle|^2 \rho(E + \hbar\omega) + \right. \\ &\quad \left. + |\langle E - \hbar\omega | Q | E \rangle|^2 \rho(E - \hbar\omega) \} dE \right] d\omega \quad (2.7) \end{aligned}$$

hence, using (2.2):

$$\begin{aligned} \langle \mathcal{V}^2 \rangle &= \int_0^\infty |\mathcal{Z}|^2 \hbar \omega^2 \left[\int_0^\infty \{ |\langle E + \hbar\omega | Q | E \rangle|^2 \rho(E + \hbar\omega) + \right. \\ &\quad \left. + |\langle E - \hbar\omega | Q | E \rangle|^2 \rho(E - \hbar\omega) \} \rho(E) f(E) dE \right] d\omega \quad (2.8) \end{aligned}$$

The integral expressions included both in (2.5) and in (2.6) make evident the fact that dissipation and fluctuation are intimately related, having the same physical origin. Confronting the two equations, by means of some algebra one obtains the mean square value of the generalized fluctuating force:

$$\langle \mathcal{V}^2 \rangle = \frac{2}{\pi} \int_0^\infty R(\omega) \left\{ \frac{1}{2} \hbar \omega + \hbar \omega \left[\exp \frac{\hbar \omega}{k_B T} - 1 \right]^{-1} \right\} d\omega \quad (2.9)$$

At high temperatures ($k_B T \gg \hbar \omega$) this expression becomes:

$$\langle \mathcal{V}^2 \rangle = \frac{2}{\pi} k_B T \int_0^\infty R(\omega) d\omega \quad (2.10)$$

Since one is usually interested in the power spectral density, the latter must be differentiated with respect to frequency, so that, putting $\omega = 2\pi f$:

$$\boxed{\mathcal{S}_V^2 = 4k_B T R(f)} \quad (2.11)$$

which is the classic form of the fluctuation-dissipation theorem. It must be emphasized that in (2.11) the dissipation is represented by the resistance R . Making use of the definition of impedance (2.2), the power spectral density for the \mathcal{Q} coordinate is also computed:

$$\mathcal{S}_Q^2 = \frac{k_B T}{\pi^2 f^2} \Re\left[\frac{1}{Z(f)}\right] \quad (2.12)$$

While the mean square values $\langle \mathcal{V}^2 \rangle$ and $\langle \mathcal{Q}^2 \rangle$ are related to the equipartition energy, the fluctuation-dissipation theorem provides information on the spectral distribution of thermal fluctuations. Clearly, the integral over the frequency of the fluctuation energy must be equal to the equipartition value $k_B T$.

2.1.1 Case of a gravitational waves interferometer

The fluctuation-dissipation theorem applies widely to almost all the fields of physics, from the brownian motion to the electric dipole radiation. In the case of gravitational waves interferometers, \mathcal{Q} represents the mirrors position, fluctuating under the effect of the force \mathcal{V} . However, finding the mechanical impedance of the system constituted by mirror and suspension fibres is not trivial, involving an infinite number of degrees of freedom. Basically two ways of applying the fluctuation-dissipation theorem to such a system are currently used for overcoming this problem.

The set of normal vibrations of the mirror and of the suspensions, being the modes nearly orthogonal, can be split in single one-dimensional harmonic oscillators with suitable proper frequency and effective mass [36]. As described in the following, the application of the theorem to a simple oscillator is straightforward. The contributions to the thermal noise from each oscillator are thus added up to a certain number of modes. As long as the materials of mirrors and fibres are homogeneous, this approach leads to a correct estimation of the noise spectrum. That is the case for the suspending fibres contributions.

In presence of energy loss inhomogeneities, such as in the mirrors coatings, the harmonic decomposition fails [37]. Thus, a direct application of the theorem has been developed by Levin [38]. The mirror is supposed being acted in a point \mathbf{r} of the reflecting surface by a force $F(\mathbf{r}, t) = F_0 \cos(\omega t)P(\mathbf{r})$, where $P(\mathbf{r})$ is a weighting factor which takes in account the profile of the readout system, that is the laser. Once the mean dissipated power resulting from such action, W_0 , is computed, the

dissipation-fluctuation theorem can be rewritten in the form:

$$\mathcal{S}_X^2 = \frac{2k_B T W_0}{\pi^2 f^2 F_0^2} \quad (2.13)$$

The discussion henceforth will focus on suspension fibres issues; therefore, in the following only the harmonic decomposition will be considered in detail.

2.2 Hooke's law and loss angle

In order to find out the dynamics of a mechanical system, one must consider both the external forces \mathbf{f} per unit mass acting on it and the inner elastic stresses \mathbf{f}_e , so that the equation of motion for the system displacement vector $\mathbf{U}(\mathbf{r}, t)$ is:

$$\frac{\partial^2 \mathbf{U}}{\partial t^2} + \mathbf{f}_e = \mathbf{f} \quad (2.14)$$

The inner stresses are described by the constitutive equation of the body, the Hooke's law, in terms of strain and stress tensors ϵ_{ij} and σ_{ij} :

$$\epsilon_{ij} = C_{ijkl} \sigma_{kl} \quad (2.15)$$

where C_{ijkl} is called compliance tensor. For the sake of simplicity, henceforth a homogeneous, isotropic body will be considered, therefore equation (2.15) can be written in simple scalar form:

$$\sigma = Y \epsilon \quad (2.16)$$

and the real coefficient Y is the Young's modulus of the material.

In order to describe energy losses in the body, the constitutive law must be modified, in such a way that in equation (2.14) a term giving rise to power dissipation appears. Once the energy loss is formally included in (2.16) by means of a suitable parameter, the simple case of one-dimensional oscillator can be handled and the harmonic decomposition can be performed. The matter of what is the physical origin of such dissipation, can be thus regarded as a somehow independent problem.

With the aim of introducing a clever and suitable dissipative parameter in (2.16), one is led to evaluate the power loss in a simple linear system. By making use of the admittance \mathcal{Y} , defined as the inverse of

the impedance, the mean power lost by the system under a periodic solicitation $F_0 \cos(\omega t)$ is computed as:

$$\bar{P} = \frac{1}{2T} \int_{-T}^T F_0^2 |\mathcal{Y}| \cos(\omega t) \cos(\omega t + \psi) dt \quad (2.17)$$

Here $T = 2\pi/\omega$ and ψ is the phase of \mathcal{Y} . If such phase is $\pm\pi/2$, clearly \bar{P} is zero; the dissipation is only present if the admittance has a non vanishing real part. This result has two important implications.

First, let us consider the system response to a step input. The resulting displacement will in general exhibit a relaxation, taking a certain time to reach the final equilibrium position. It can be readily shown that such relaxation happen only if $\Re[\mathcal{Y}]$ is not zero. Thus, dissipation and relaxation are strictly interlaced.

Then, consider the frequency response \mathcal{T} defined by:

$$\tilde{Q}(\omega) = \mathcal{T}(\omega) \tilde{V}(\omega) \quad (2.18)$$

Admittance and frequency response are simply related, being $\mathcal{Y} = i\omega\mathcal{T}$. For the above considerations, the dissipation appears as a non vanishing imaginary part of the frequency response, so that a phase lag exists between the soliciting force and the corresponding displacement of the system.

By analogy with the latter argument, the constitutive law can be rewritten in the frequency domain by introducing a small, non vanishing imaginary part in the complex Young's modulus [39], [40]:

$$\tilde{\sigma}(\omega) = [Y_r(\omega) + iY_i(\omega)] \tilde{\epsilon}(\omega) \quad (2.19)$$

The phase lag is then:

$$\phi(\omega) \approx \frac{Y_i}{Y_r} \ll 1 \quad (2.20)$$

The quantity ϕ , called *loss angle*, is the key feature in modeling the dissipation in a linear system. To a good approximation³, one can therefore put the Hooke's law in presence of energy loss in the form:

$$\tilde{\sigma}(\omega) = Y[1 + i\phi(\omega)] \tilde{\epsilon}(\omega) \quad (2.21)$$

³The prescription of causality for the system response requires the real and imaginary parts of the admittance to be linked by the so called Kramers-Kronig relations [39], [41], so that Y_r and Y_i depend the one on the other. However, as long as the loss angle is small, Y_r is almost equal to Y .

The loss angle is strictly related to the amount of energy lost in a cycle of periodic motion. Imagine the system being excited with a time periodic strain $\epsilon = \epsilon_0 \exp^{i\omega t}$. Keeping in mind equation (2.19), in the limit (2.20) the maximum energy per unit volume stored in the oscillation is:

$$\mathcal{E}_{MAX} = \frac{1}{2} \Re[\sigma] \Re[\epsilon]_{MAX} \simeq \frac{1}{2} Y_r(\omega) \epsilon_0^2 \quad (2.22)$$

while the mean energy dissipated in a cycle, per unit volume is:

$$\mathcal{E}_{DISS} = \int_{cycle} \Re[\sigma] \Re[\dot{\epsilon}] dt \simeq \pi Y_i(\omega) \epsilon_0^2 \quad (2.23)$$

Taking the ratio between equations (2.23) and (2.22) one obtains:

$$\frac{\mathcal{E}_{DISS}}{\mathcal{E}_{MAX}} \simeq 2\pi \frac{Y_i}{Y_r} \approx 2\pi\phi(\omega) \quad (2.24)$$

Even if the strain pattern within the body is supposed to assume a very general form, the result (2.24) maintains its validity, provided that the material under consideration is homogeneous. Since energy losses add linearly, the superposition of loss sources with different angles ϕ_i is correctly described by an effective loss angle $\phi = \sum_i \phi_i$.

In the presence of a conservative force, like for instance the gravity, the loss angle is somehow diluted [42]. Writing again the equation (2.24) in terms of the total energy dissipated E_{DISS} and the mean elastic potential energy V_e , then adding a generic potential V , one has:

$$\frac{\mathcal{E}_{DISS}}{\mathcal{E}_{MAX}} = \frac{E_{DISS}}{2(V_e + V)} = \frac{E_{DISS}}{2(V_e)} \frac{V_e}{V_e + V} = 2\pi\phi D \quad (2.25)$$

so that the resulting loss angle is lower than ϕ by a factor $D = V_e/(V_e+V)$, which is called *dilution factor*.

2.3 Harmonic oscillator with losses

The first step of the harmonic decomposition approach consists in studying the behaviour of a simple, one-dimensional harmonic oscillator under the action of a dissipative force. As shown in the previous section, the corresponding Hooke law includes a complex Young's modulus with a small imaginary part (equation (2.21)), leading to a complex elastic constant k :

$$k \longrightarrow k(1 + i\phi(\omega)) \quad (2.26)$$

The equation:

$$m\ddot{x} = -k(1 + i\phi(\omega))x + F_{ext} \quad (2.27)$$

describes then the motion of the oscillator with mass m driven by an external force F_{ext} .

It is worthwhile comparing (2.27) with the equation of an oscillator with viscous damping [43]:

$$m\ddot{x} = -kx - b\dot{x} + F_{ext} \quad (2.28)$$

where b is the viscous drag coefficient. Substituting a harmonic solution $x = x_0 \exp^{i\omega t}$ in both expressions, one finds by comparison that the loss angle in the viscous case is proportional to the frequency:

$$\phi(\omega)_{VISCOUS} = \frac{b \omega}{k} \quad (2.29)$$

Traditionally, oscillators performances are characterized by using the quality factor Q , which corresponds to the ratio between the energy stored in the natural frequency of a viscous oscillator $\omega_0 \simeq \sqrt{k/m}$, and that which is lost in a cycle. Applying the definition of Q , it is easy to show that:

$$Q = \frac{k}{b \omega_0} \quad (2.30)$$

The quality factor and the loss angle for the viscous resonator are thus related in the following way:

$$\phi(\omega)_{VISCOUS} = \frac{\omega}{Q\omega_0} \quad (2.31)$$

The latter result is relevant for the technique which is usually employed in measuring the loss angle, as described in chapter (4).

Equation (2.27) allows the mechanical impedance of the oscillator to be computed, obtaining:

$$\mathcal{Z}(\omega) = \frac{\tilde{F}_{ext}}{\dot{x}} = \frac{m}{\omega} (\phi(\omega)\omega_0^2 + i(\omega^2 - \omega_0^2)) \quad (2.32)$$

The lossy resonator is clearly a linear and dissipative system, so that the fluctuation-dissipation theorem can be applied. The resulting displacement thermal fluctuation has the spectrum:

$$\langle S_x^2 \rangle = \frac{4k_B T}{m\omega} \frac{\phi(\omega)\omega_0^2}{(\omega^2 - \omega_0^2)^2 + \phi(\omega)^2\omega_0^4} \quad (2.33)$$

Far beyond the resonance, equation (2.33) becomes:

$$\langle S_x^2 \rangle = 4k_B T \frac{\phi(\omega)\omega_0^2}{m\omega^5}, \quad \omega \gg \omega_0 \quad (2.34)$$

Now that the thermally induced vibrations spectrum is written for the simple one-dimensional lossy oscillator, the full noise spectrum for a complex mechanical system will be obtained by summing the contributions from each normal mode, thought as a single resonator with its equivalent mass. Practically, the sum over the modes has some convergence range, after which it can be truncated.

The former thermal noise analysis has been performed without specifying the physical content of $\phi(\omega)$; its form and frequency dependence were thought to be known, for instance as the result of a suitable measurement. In the following, the loss angle will be related to models of dissipative mechanisms.

2.4 The standard anelastic solid and Debye peak

Deviation of solid bodies from the ideal elasticity is generally referred to as *anelasticity*. The anelastic behaviour will result in some dissipation described by a proper loss angle. For example, the proportionality of ϕ to the frequency in the viscous case has been already highlighted (equation (2.29)).

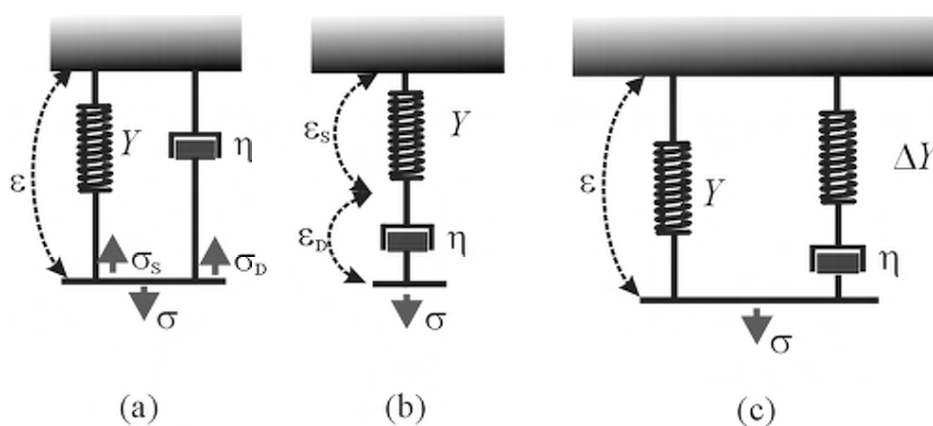


Figure 2.1: Schemes of the solid models discussed in the text. (a) Kelvin-Voigt solid, (b) Maxwell unit, (c) standard anelastic solid.

The viscous dissipation within a body can be described using a mechanical model, called the Kelvin-Voigt solid (see figure (2.1)), which, in place of a simple lossless spring, consists in a spring and a dashpot in parallel. Suppose a strain ϵ is set; while the spring provides a Hook-like stress $\sigma_S = Y\epsilon$, for the dashpot $\sigma_D \propto \dot{\epsilon}$. The whole stress is simply the sum of both the contributions. Therefore, the constitutive equation for such material is usually written as:

$$\sigma = Y\epsilon + \tau_r Y \dot{\epsilon} \quad (2.35)$$

The meaning of the proportionality factor τ_r can be explained as follows. If a sudden constant stress σ_0 is applied to the KV solid, the strain exhibits an exponential approach to the Hooke law value $\epsilon_0 = \sigma_0/Y$, with a decay time τ_r . As discussed in section (2.2), this relaxation is indicative of the onset of dissipation. The dashpot is represented by a viscous constant defined as:

$$\eta = \tau_r Y \quad (2.36)$$

Conversely, one can think about a material in which the relaxation appears in the stress, provided a constant strain is switched on. The mechanical equivalent model (the so called Maxwell solid or Maxwell unit, figure (2.1)) is built again with a dashpot and a lossless spring, but now arranged in series. Here, suppose a stress σ is applied to the body. Since it has been found that for the dashpot $\sigma = \tau_r Y \dot{\epsilon}_D$, it is convenient to compute $\dot{\epsilon}$, so that for the spring $\dot{\epsilon}_S = \dot{\sigma}/Y$. In this configuration, the contributions $\dot{\epsilon}_S$ and $\dot{\epsilon}_D$ add together. The resulting equation is:

$$\dot{\epsilon} = Y^{-1} \dot{\sigma} + (\tau_r Y)^{-1} \sigma \quad (2.37)$$

The relaxing stress shows a time constant $\tau_r = \eta/Y$. The associated loss angle can be worked out with a harmonic analysis, by introducing the complex Young's modulus $\mathbf{Y} = \sigma(\omega)/\epsilon(\omega)$:

$$\mathbf{Y}(\omega) = \frac{i\omega\eta Y}{Y + i\omega\eta} \quad (2.38)$$

Following the given definition:

$$\phi(\omega) = \frac{\Im[\mathbf{Y}]}{\Re[\mathbf{Y}]} = \frac{Y}{\eta\omega} \quad (2.39)$$

However, a large number of materials show both a relaxation time τ_σ for stress *and* a relaxation time τ_ϵ for strain. Such condition would be

expressed by a constitutive law containing the time derivative of the stress and of the strain. The corresponding mechanical scheme is a lossless spring with Young's modulus Y , in parallel with a Maxwell unit ΔY , η (refer again to figure (2.1)). It can be shown with a bit more complex algebra that the respective constitutive law is:

$$\sigma + \tau_\sigma \dot{\sigma} = Y(\epsilon + \tau_\epsilon \dot{\epsilon}) \quad (2.40)$$

where the decay times are:

$$\tau_\sigma = \frac{\eta}{\Delta Y} \quad (2.41)$$

$$\tau_\epsilon = \frac{Y + \Delta Y}{Y \Delta Y} \eta \quad (2.42)$$

Computing the loss angle as in equation (2.39):

$$\mathbf{Y}(\omega) = Y \frac{1 + i\omega\tau_\epsilon}{1 + i\omega\tau_\sigma} \quad (2.43)$$

$$\phi(\omega) = \Delta(\omega\bar{\tau})/[1 + (\omega\bar{\tau})^2] \quad (2.44)$$

where:

$$\bar{\tau} = \sqrt{\tau_\sigma \tau_\epsilon} \quad (2.45)$$

$$\Delta = \frac{\tau_\epsilon - \tau_\sigma}{\sqrt{\tau_\sigma \tau_\epsilon}} \quad (2.46)$$

The body described by equation (2.40) is usually called *standard anelastic solid* (SAS), while the frequency dependence of $\phi(\omega)$ in (2.44) leads to a bell-shaped plot (a *Debye peak*), reaching its maximum value $\Delta/2$ at $\omega = \bar{\tau}^{-1}$.

When the dissipation is small, that is when $Y \gg \Delta Y$, the relaxation time is the same for stress and strain $\bar{\tau} \simeq \tau_\epsilon \simeq \tau_\sigma = \eta/\Delta Y$, and $\Delta \simeq \Delta Y/Y$. In this approximation, the equivalent spring constant⁴ for the SAS can be obtained from (2.43):

$$k_{SAS} = k(1 + \omega\bar{\tau}\phi(\omega) + i\phi(\omega)) \quad (2.47)$$

where k is the equivalent constant for an ideal elastic body with Young's modulus Y . For very low frequencies, $k_{SAS} \simeq k$, so that Y is referred to as the SAS *relaxed* modulus.

⁴Note that in the written expression of the SAS spring constant, the real part is frequency dependent. It must be kept in mind that equation (2.21) is an approximation, as explained in the footnote (3).

The SAS model fits with those dissipative processes which are suitably characterized by means of two parameters, for instance, the two time delay constants previously defined. It gives an adequate description for most of the practical cases⁵, so that it is a standard choice in treating them.

In next paragraphs a brief review of the main dissipative processes in solids is presented. Anelasticity affecting internal variables will be accounted for using the SAS model. Of course, there are also external sources of energy loss, such coupling with mechanical supports, or leaking out by sound waves in air.

2.4.1 The thermoelastic effect

In searching for internal dissipative mechanisms, one has to look at those processes which are excited by means of vibrations, and take a finite time to reach an equilibrium condition⁶. Since the free energy in elastic bodies depends on the deformation, it is expected that the coupling between strain and temperature gives rise to an irreversible heat flux and thus to dissipation.

In a periodic motion, a thermal diffusion process is established between neighbouring regions of contraction, where the temperature raises up, and expansion, where it falls down. The temperature T can be thus taken as the internal relaxing variable; this process is called *thermoelastic effect* [44], [45], [46]. It must be explicitly noted that this effect is limited to frequencies which are low compared with phonons relaxation rates, so that a local temperature is well defined.

The main feature of the thermoelastic dissipation is represented by the characteristic time τ_{th} of heat migration. If the vibration frequency is small with respect to τ_{th}^{-1} , the thermalization between compressed and expanded regions occurs almost instantaneously (isothermal limit); conversely, at high frequencies the temperature has not enough time to set up a heat flux, therefore the vibration is practically adiabatic.

The typical relaxation time for the thermal gradient can be obtained

⁵Actually, the SAS cannot get through all the anelastic processes in metals and different materials; models involving three or more parameters can be developed as well, but for the purposes of this chapter only the SAS will be considered in detail.

⁶As explained above, energy loss occur if the system reacts to a sudden change in deformation with a finite relaxation time.

by solving the heat diffusion equation:

$$\frac{\partial T}{\partial t} = \frac{\kappa}{c_V} \nabla^2 T - \frac{Y \alpha T_0}{c_V (1 - 2\sigma)} \frac{\partial(\nabla \cdot \mathbf{u})}{\partial t} \quad (2.48)$$

where κ is the thermal conductivity, c_V is the specific heat per unit volume, α is the thermal expansion coefficient, σ is the Poisson's ratio and \mathbf{u} is the elastic deformation vector. The solution of equation (2.48) depends clearly on the geometry of the considered body. If d is the distance between expansion and contraction regions⁷, it results that:

$$\tau_{th} = C d^2 \frac{c_V}{\kappa} \quad (2.49)$$

being C an adimensional form factor which takes into account the particular geometry and the shape of the considered vibration mode⁸. The thermoelastic contribution to loss angle, related to a macroscopic relaxation τ_{th} , can be modeled with a SAS configuration, obtaining a Debye peak:

$$\phi_{th}(\omega) = \phi_0 \frac{\omega \omega_{th}}{\omega^2 + \omega_{th}^2} \quad (2.50)$$

where the maximum dissipation happens when $\omega = \omega_{th} = 2\pi/\tau_{th}$. The dissipation strength ϕ_0 in the SAS model results:

$$\phi_0 = T Y \frac{\alpha^2}{c_V} \quad (2.51)$$

Objects which have at least one dimension much larger than the others show a prominent thermoelastic peak in the frequency band of the first resonant modes. On the contrary, this effect is usually negligible for bulky objects with ω_{th} small with respect to the modal frequencies.

The former discussion, valid for homogeneous bodies, must be modified for anisotropic materials, like crystals, whose thermal expansion, conduction and elastic moduli depend on the orientation. Nevertheless, the main features are the same; a rough estimation of the thermoelastic dissipation can be obtained in such case by averaging α , κ , Y and σ over the solid angle and using (2.50).

⁷The geometrical parameter d does not coincide in general with the wavelength of the vibration. Consider a thin, long cylinder; in this case, the largest thermal gradient occurs normally to the length, where the separation is set by the cross sectional size, so that d can be equated to the cylinder diameter.

⁸If d is small with respect to the mode wavelength, C is almost independent of the mode shape. For instance, for a thin, long cylinder $C \simeq 1/2.16$ for the low frequency flexural modes.

If the material under study is polycrystalline, there is an additional thermoelastic dissipation source which must be considered [47]. The presence of crystal grains with average dimension d_G defines a new typical heat diffusion time $\tau_{th,G}$. In the regime $\omega\tau_{th,G} \ll 1$ the vibrations are nearly isothermal for neighbouring grains and the resulting loss angle is viscous-like, proportional to ω . If conversely $\omega\tau_{th,G} \gg 1$, within each grain the deformation is adiabatic. In the latter case, the heat conduction is confined to a grain shell with characteristic thickness $\delta = (D_{th}/\omega)^{1/2}$, being D_{th} the thermal diffusivity. It results that:

$$\phi(\omega) \propto (\omega\tau_{th,G})^{-1/2} \quad (2.52)$$

The contribution of such intercrystalline heat diffusion to the dissipation in polycrystalline objects is in general not negligible.

A nonlinear thermoelastic loss mechanism due to the temperature dependence of the material elastic moduli can be of remarkable importance in GW detectors suspension fibres; it has been described in [48].

2.4.2 Structural losses

Dissipation mechanisms which are related to microscopical variables within the solid, such as orientation or displacement of atoms and molecules and the presence of defects, are classified under the generic name of *structural losses*. They are described by a set of typical relaxation times.

All these structural processes can be thought as being excited once an activation energy U is reached. The population of particles which possesses the needed energy U is set by the Boltzmann's distribution, so that the rate of events follows an Arrhenius' exponential law:

$$\bar{\tau}^{-1} = \nu_0 \exp^{-\frac{U}{k_B T}} \quad (2.53)$$

where $\bar{\tau}$ is the relevant relaxation time to be included in the SAS model. Therefore one obtains:

$$\phi(\omega) = \Delta \frac{\omega\bar{\tau}}{1 + \omega\bar{\tau}^{-1}} = \frac{\Delta}{2} \left[\sinh \left(\ln(\omega\bar{\tau}) + \frac{U}{k_B T} \right) \right]^{-1} \quad (2.54)$$

Plotting equation (2.54) versus $1/T$ produces a peak similar to a Debye peak, centered in $k_B T = -U/\ln(\omega\bar{\tau})$. Individual relaxation processes giving rise to such peaks have been experimentally observed and interpreted in many materials.

By contrast, there is experimental evidence of a structural contribution to loss angle which is almost constant in frequency [49], [50], [51]. The phenomenon is usually modeled by considering a superposition of similar Debye peaks with continuously distributed activation energies. The energy distribution is taken constant within a large interval:

$$f(U)dU = \frac{dU}{U_2 - U_1} \quad (2.55)$$

Computing the sum of single Debye terms:

$$\begin{aligned} \phi_{TOT}(\omega) &= \Delta \int_{U_1}^{U_2} \frac{\omega \bar{\tau}}{1 + (\omega \bar{\tau})^2} \frac{dU}{U_2 - U_1} = \\ &= \frac{\Delta}{U_2 - U_1} k_B T (\arctan(\omega \bar{\tau}_1) - \arctan(\omega \bar{\tau}_2)) \end{aligned} \quad (2.56)$$

where:

$$\bar{\tau}_{1,2} = \nu_0^{-1} \exp \frac{U_{1,2}}{k_B T} \quad (2.57)$$

The density defined in (2.55) can be put in the form of a function of the relaxation time, by means of the equation (2.53), obtaining:

$$f(\tau) = \frac{k_B T}{U_2 - U_1} \frac{1}{\tau} \quad (2.58)$$

The latter relation points out the fact that the discussed constant loss model is equivalent to the request that the structural dissipation behaves like $1/f$ noise [52].

There are many studied internal dissipation processes. In amorphous objects, specific mechanisms described by the thermal activation (equation (2.54)) are well known [47]. In crystals and metals, they can be divided in two groups: those which act even in a perfect crystal, and those due to the presence of defects in the body microscopical structure. Both are summarized in the rest of this paragraph.

Phonons and electrons relaxation

It is well known that the phonon-phonon interaction arising from perfect crystal anharmonicity provides a mechanism for sonic and ultrasonic attenuation [53]. If the elastic wave frequency is low enough for the phonon mean lifetime τ_{ph} to be much lower than the wave period, i.e., if $\omega \tau_{ph} \ll 1$, then relaxation formalism of SAS can be applied [47]. In fact, within this limit the phonon distribution rearranges itself almost instantaneously

during the vibration; the relaxation happens locally, and locality is requested for (2.19) to be valid. However, such low frequency limit is well satisfied for the materials and conditions which are considered here.

As a result of the crystal anharmonicity, the phonon frequencies are modulated by the acoustic strain. The three-dimensional anisotropic nature of the lattice structure and the dispersive phonon propagation make the frequency shift depend on the strain via the so called *Grüneisen parameters* $\gamma_{k\alpha}$:

$$\frac{\Delta\Omega_{k\alpha}}{\Omega_{k\alpha}} = \gamma_{k\alpha}\epsilon \quad (2.59)$$

where the wavevector k and the polarization α specify the branch of phonon spectrum.

The tensor nature of the strain is not specified in equation (2.59). Usually, the Grüneisen parameters are defined for a pure dilation ϵ_{jj} [54], while a general treatment for arbitrary strain needs a Grüneisen tensor $\gamma_{k\alpha}^{ij}$ to be defined [55], [56], [57]. Nevertheless, the overall contribution to the acoustic damping will be of the order of the pure dilation relaxation, which can be roughly estimated as:

$$\phi_{ph}(\omega) = \left(\frac{K\alpha_g^2 T}{c_g} \right) \omega\tau_{ph} \quad (2.60)$$

In the case of metals, an anelastic relaxation mechanism analogous to the phonons relaxation just discussed is due to conduction electrons [47].

Point defects and dislocations

The presence in a real crystal of point defects such as interstitial or substitutional impurities in the lattice will in general give rise to relaxation phenomena. If, for instance, impurity atoms can be arranged in crystallographically equivalent interstitial sites, the distribution of such defects is modulated by an applied stress. Therefore, energy dissipation arises. Beside the described behaviour, called *Snoek effect* [58], [59], many other point defect processes are known, such as stress-induced pairs reordering, quantum tunneling and so on. A typical value of the activation energy for these mechanisms is 1 eV; they give rise to Debye peaks which usually show a maximum at audiofrequency well above room temperature [47]. Hydrogen impurities can instead provide relaxation channels at lower temperatures, due to their smaller volume and activation energy [58].

Dislocations appear within a real crystal basically in two ways [39]. An *edge* dislocation occurs when a crystalline plane is inserted within

two other close packed planes. *Screw* dislocations can be visualized imagining each plane being cut along an half infinite segment, then each cut edge being glued to the opposite edge of the adjacent plane. It results in an helicoidal surface around a defect line orthogonal to the crystal planes.

As well as for point defects, dislocations can be strongly coupled with external mechanical solicitations [60], [61], [62]. The internal friction processes caused by the dislocation motion under an applied stress are divided in two categories [39].

In the case the dislocation orientation differs from the crystallographic directions, its motion can be described in terms of continuum mechanics, since discrete features disappear by averaging over the dislocation length. It has been shown [63], [64], [39] that under these assumptions the dislocation can be regarded as a vibrating string, with a resonant peak at ultrasonic frequencies. In the low frequency band, the contribution to dissipation is:

$$\phi_d(\omega) \propto \Lambda l^4 \omega \quad (2.61)$$

where Λ is the dislocation density and l is a typical dislocation length.

If otherwise the dislocation lies close to a crystallographic direction, there exists a potential barrier to its movement due to the periodic variation of the dislocation energy along its length (Peierls potential [65]). This relaxation mechanism is thermally activated, thus leading to a Debye peak whose parameters depend on l .

Both mechanisms give rise to a loss angle which increases with increasing l , so that their effects should be still present even in annealed samples, where great values of l can counteract the decreasing of Λ .

Finally, interactions between dislocations and point defects must also be considered [66]. The pinning of dislocation lines by the impurities, resulting in a shortening of l , is an example of such mixing processes. Theoretical work on this topic, and in general on defect losses, is still in progress, due both to the difficulty of measuring parameters such as the defect density, and to the variety of possible specific mechanisms.

2.4.3 Surface effects

In the previous section, structural defects in a real crystal have been treated supposing that their distribution within the body was homogeneous. In fact, this is the case for homogeneous materials, as long as

the volume contribution to loss angle is considered. The dissipation is proportional to the defect density.

Still, the surface of a body is exposed to chemical and mechanical damage; it is likely that here the amount of defects is much greater than in the volume. Indeed, in homogeneous bodies the overall dissipation increases for higher surface to volume ratios, due to surface effects.

Surface contribution can be included in the total loss angle by the following definition:

$$2\pi\phi_{TOT} = \frac{\Delta\mathcal{E}_{BULK} + \Delta\mathcal{E}_{SURF}}{\mathcal{E}_{TOT}} \quad (2.62)$$

where \mathcal{E}_{TOT} is the energy stored in the oscillation, $\Delta\mathcal{E}_{BULK}$ and $\Delta\mathcal{E}_{SURF}$ are the amounts of energy dissipated in the volume and near the surface, respectively. One assumes that $\Delta\mathcal{E}_{BULK}$ is proportional to the volume V of the body, and $\Delta\mathcal{E}_{SURF}$ to the surface S :

$$\frac{\Delta\mathcal{E}_{SURF}}{\Delta\mathcal{E}_{BULK}} = D \frac{S}{V} \quad (2.63)$$

The proportionality factor D has the dimension of a length; it carries the information about the oscillation mode shape and the geometry of the body. Moreover, it depends on the entity of surface dissipation. It is convenient therefore [67] to put it in the form $D = \mu d_s$, in such a way that μ takes into account geometry and dynamics and d_s , called *dissipation depth*, models the presence of a dissipative layer at the surface. One thus obtains from (2.62) and (2.63), being $\mathcal{E}_{TOT} \simeq \mathcal{E}_{BULK}$:

$$\phi_{TOT} = \phi_{bulk} \left(1 + \mu d_s \frac{S}{V} \right) \quad (2.64)$$

since the bulk loss angle is defined as:

$$\phi_{bulk} = \Delta\mathcal{E}_{BULK}/\mathcal{E}_{BULK} \simeq \Delta\mathcal{E}_{BULK}/\mathcal{E}_{TOT}. \quad (2.65)$$

The dissipation depth is related to the thickness h of the superficial dissipative shell. Let $\phi(n)$ be the local value of the loss angle in a small volume at depth n ; then it results:

$$d_s = \int_0^h \phi(n) dn \quad (2.66)$$

Supposing $\phi(n) = \phi_{surf}$ constant within the shell:

$$\phi_{surf} = \phi_{bulk} \frac{d_s}{h} \quad (2.67)$$

According to equation (2.64), surface effects are negligible if $d_s \ll V/(S\mu)$. The coefficient μ is of the order of unity; for instance, a cylindrical thin fibre oscillating transversally has $\mu = 2$.

2.5 Other sources of loss

While the dissipation processes examined hereto are intrinsic to the anelastic solid, a body can lose its mechanical energy outward, due to interactions with the environment. Usually these external loss sources are not interesting in determining the anelastic behaviour of a body, in fact, if they overcome the intrinsic loss level, care must be taken in reducing them as much as possible.

2.5.1 Recoil losses

The energy of a vibrating body clamped in a frame is partly transmitted to the support, where it is dissipated. This coupling would be null only if the supporting structure were infinitely massive and rigid; in general, though, this external source of loss is not negligible [68].

Consider the case of a pendulum of mass m hung to a mass M by a massless wire of length l . An effective spring constant for small oscillations $k_g = m g/l$ is used for modelling the restoring force due to gravity, being g the modulus of the gravitational acceleration. In order to introduce a coupling with the support, the mass M is supposed to be horizontally connected with an infinitely massive wall by an ideal spring of constant K . The dissipation within this spring is described by its internal loss angle ϕ_K . Therefore, ϕ_K measures the energy loss due to the induced vibration in the supporting frame. The equations of motion of m and M along the horizontal x axis are:

$$M\ddot{x}_M = -Kx_M - iK\phi_K x_M + k_g x_m \quad (2.68)$$

$$m\ddot{x}_m = -k_e x_m \quad (2.69)$$

Substituting in the former expressions $x_m = x_{m0} \exp^{i\omega_0 t}$, where $\omega_0 = \sqrt{g/l}$ is the pendulum angular frequency, and neglecting the small dissipation term, one finds the amplitude x_{M0} of the support motion as:

$$\frac{x_{M0}}{x_{m0}} = \frac{k_g}{(K - \omega_0^2 M)} \quad (2.70)$$

Therefore, in the limit $\omega_M^2 = K/M \gg \omega_0^2$:

$$\frac{x_{M0}}{x_{m0}} = \frac{k_g}{K} = \frac{m\omega_0^2}{K} \quad (2.71)$$

According to equation (2.24), the recoil loss is represented by an effective loss angle ϕ_e such that, if E is the total vibration energy, $2\pi\phi_e E$ is the

amount of dissipated energy. Therefore, reminding $\omega_M \gg \omega_0$:

$$\phi_e = \phi_K \frac{K x_{M0}^2}{E} \simeq \phi_K \frac{K x_{M0}^2}{k_g x_{m0}^2} \quad (2.72)$$

so that, using (2.71):

$$\phi_e \simeq \phi_K \frac{m \omega_0^2}{K} \quad (2.73)$$

The expression of ϕ_e without approximations, for a supported mechanical oscillator with natural frequency ω_0 , is found [68] to be:

$$\phi_e = \phi_K \frac{m}{M} \frac{\omega_0^2 \omega_M^2}{(\omega_M^2 - \omega_0^2)^2} \quad (2.74)$$

The leak of energy toward the support, given by equation (2.74), can be reduced by choosing a massive, rigid support with a small intrinsic dissipation. Nevertheless, if $\omega_M \sim \omega_0$, even with the proper material choice the recoil loss becomes relevant.

2.5.2 Air losses

If the vibrating body is immersed in a fluid, the viscous drag of the fluid results in a damping of the vibration. The corresponding loss angle will be of the same form of equation (2.29), i.e., proportional to the frequency:

$$\phi_{gas}(\omega) = \frac{b}{m \omega_0^2} \omega \quad (2.75)$$

where b is the viscosity coefficient of the fluid.

While in dense fluids the friction includes the effect of shear forces, in a rarefied gas the drag is mainly due to pure momentum transfer between the body and the gas molecules which are given a thermal velocity whose mean value is $\bar{v} = \sqrt{k_B T / m}$. In this case the viscosity coefficient can be written [8] as:

$$b = \frac{1}{4} \rho_{gas} A \bar{v} \quad (2.76)$$

The gas density ρ_{gas} depends on the pressure and the temperature via the usual thermodynamical equation of state for ideal fluids. The parameter A represents the total cross sectional area of the body for collisions with gas molecules during the oscillation. One thus obtains:

$$\phi_{gas}(\omega) = \frac{\rho_{gas} A \bar{v}}{4 m \omega_0^2} \omega \quad (2.77)$$

As an example, for a vibrating cylinder of diameter d and density ρ [67]:

$$\phi_{gas}(\omega) = \frac{\rho_{gas}\bar{v}}{2\rho d\omega_0^2}\omega \quad (2.78)$$

Thus the quality factor of this cylindrical resonator in a diluted gas is (see equation (2.31)):

$$Q_{gas} = \frac{2d\rho\omega_0}{\bar{v}\rho_{gas}} = \frac{2d\rho\omega_0}{n\sqrt{\mu k_B T}} \quad (2.79)$$

being n and μ the numerical density and the mass of the gas molecules. As one would expect, the limiting quality factor (2.79) becomes very high when n is small; that is, the air damping can be easily reduced by placing the resonator under vacuum.

2.6 Thermal noise in a gravitational waves interferometric detector

2.6.1 Thermal noise due to the suspension wires

The test masses of an Earth-based interferometric detector of gravitational waves are suspended in a pendulum configuration which acts as a mechanical filter for the attenuation of seismic noise. In this configuration, the thermally induced vibrations of the suspending wires result in a fluctuation of the masses position along the laser beam [69] and produce a spurious signal in the power output which limits the detector sensitivity. In the case of Virgo, whose mirrors are suspended from a chain of pendula, only the last stage is considered for the sake of evaluating the thermal noise. According to the normal-mode decomposition, the suspension wires thermal noise spectrum can be computed separately for the pendulum mode [70], [71], [72] and for the violin harmonic series [71], [73].

Pendulum mode

A point-like mass M hung by an ideal, massless wire of length L swings with an angular frequency $\omega_P = \sqrt{g/L}$. As long as the internal structure of the wire is neglected, there are no friction losses⁹ associated to the swinging and actually all the energy is stored in the lossless gravity field.

⁹It is supposed here that all the external sources of loss, such as air damping and recoil, are made negligible by a proper choice of materials and conditions.

The wire bends exactly at the upper end and, once the oscillation is stopped, no thermal noise is present.

When instead a real wire is considered, the pendulum mode shape is determined by the tension \mathcal{T} applied by the suspended mass and by the elastic characteristics of the wire material. The bending occurs at a finite distance from the top, called *bending length* λ , which for a rod of constant cross section Σ has the expression [42]:

$$\lambda = \sqrt{\frac{YI}{\mathcal{T}}} \quad (2.80)$$

where Y is the Young's modulus and I is the geometrical moment of inertia of Σ :

$$I = \int_{\Sigma} r^2 dx dy \quad (2.81)$$

being r the distance from an axis passing through the center of the section.

An extended mass M hung by a single wire will exhibit both pendulum and *rocking* swing. A rocking mode is indeed present for which the bending is located mainly near the mass, again at distance λ ¹⁰. In an interferometric detector, the test masses are suspended by several wires. It is assumed here that each cylindrical mirror is suspended by four wires fixed sideward; the wires are pinned in four points forming an horizontal rectangle whose center lies near the center of mass of the mirror. The real configuration is obtained with a cradle suspension [74] (see figure (2.2)). In this arrangement, the rocking mode is essentially suppressed, while during the pendulum swing each wire bends both at the top and at the bottom. Therefore, a certain amount of energy is contained in the elastic strain, so that dissipation occurs.

Recall equation (2.25). Calling $\phi_w(\omega)$ the intrinsic loss angle of the wires, the overall loss angle to be considered here is diluted by the presence of the gravity field [68], [75], [76]:

$$\phi_P(\omega) = D_P \phi_w(\omega) \quad (2.82)$$

where:

$$D_P = \frac{V_e}{V_G + V_e} \simeq \frac{V_e}{V_G} \quad (2.83)$$

¹⁰If the cross section depends on the position along the wire, there will be in general two different bending lengths at the top and at the bottom, but the main features of the discussion do not change.

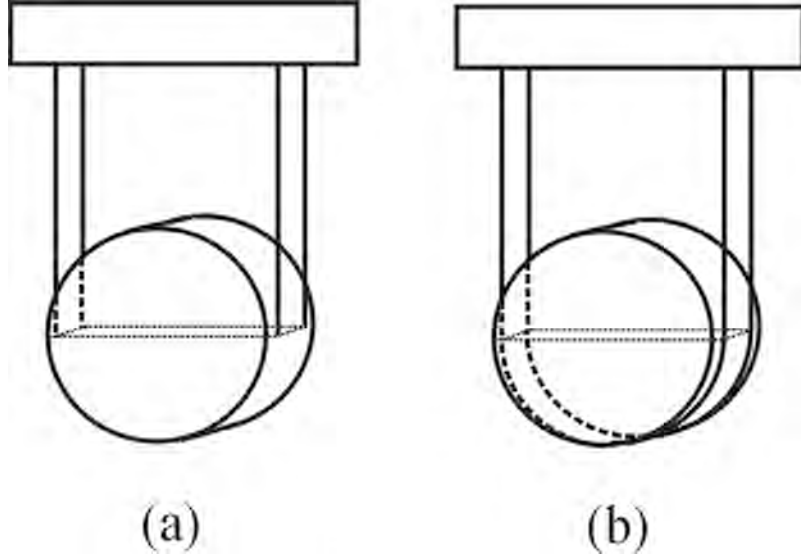


Figure 2.2: Scheme of the mirror suspension configuration described in the text. (a) Pinned fibres (b) Cradle suspension.

is the relevant dilution factor, V_e , V_G are the elastic and gravitational mean potential energies and small oscillations are assumed. By solving the elasticity equations for the four wires one finds that¹¹:

$$D_P = \frac{1}{L} \sqrt{\frac{YI}{\mathcal{T}}} \quad (2.84)$$

Here $\mathcal{T} = Mg/4$ is the tension applied to each wire. Now, the pendulum mode corresponds to an oscillator with mass M and elastic constant $k_g = Mg/L$, so that, making use of (2.33):

$$\langle S_{x,P}^2 \rangle = \frac{4k_B T}{M\omega} \frac{\phi_P(\omega)\omega_P^2}{(\omega^2 - \omega_P^2)^2 + \phi_P^2(\omega)\omega_P^4} \quad (2.85)$$

is the thermal noise spectrum for the displacement x along the laser beam, due to the pendulum resonance.

Violin and bouncing modes

Besides the pendulum mode, which is due to the presence of gravity, a real wire possesses a set of vibration proper modes due to the elastic inner

¹¹This expression is doubled with respect to that valid for a pendulum with point-like mass [71], since the bending here happens both at the upper and at the lower end.

forces. The shape and frequency of such modes is clearly depending on the tension \mathcal{T} , therefore, even though they are due to elasticity, they are influenced by gravity.

The spring-like vibration of a wire suspending a mass M is called *bouncing mode*; the equivalent spring constant is $k_B = Y\Sigma/L$, thus the angular frequency:

$$\omega_B = \sqrt{\frac{Y\Sigma}{ML}} \quad (2.86)$$

Neglecting the coupling between vertical and horizontal displacement, the bouncing mode would not affect the position of the mirror along the laser beam. However, such coupling exists in a gravitational waves interferometer, due to the Earth curvature and imperfections in the mechanics of the suspensions: the vertical directions for two mirrors placed apart at a distance D are not parallel, they form an angle $\psi = D/R_\oplus$, calling R_\oplus the Earth radius. Therefore, the vertical bouncing mode gives rise to a thermal noise spectrum modulated by ψ :

$$\langle S_{x,B}^2 \rangle = \psi \frac{4k_B T}{M\omega} \frac{\phi_w(\omega)\omega_{B,N}^2}{(\omega^2 - \omega_{B,N}^2)^2 + \phi_w^2(\omega)\omega_{B,N}^4} \quad (2.87)$$

where $\omega_{B,N} = \sqrt{N}\omega_B$ if N is the number of suspension wires.

Instead, the violin transverse modes of the wires contribute directly to the suspension thermal noise. The set of violin harmonics is given by the formula:

$$\omega_n = \frac{n\pi}{L} \sqrt{\frac{\mathcal{T}}{\Sigma\rho}} \left[1 + \frac{2\lambda_v}{L} + \frac{1}{2} \left(\frac{n\pi\lambda_v}{L} \right)^2 \right] \quad n = 1, 2, \dots \quad (2.88)$$

where ρ is the mass density. The shape of the violin modes is such that most of the wire bending occurs again at its top and bottom, over a typical distance $\lambda_v \simeq \lambda$. Since for the suspension wires $\lambda \ll L$, the first several modes are almost equal to the vibrations of an ideal string:

$$\omega_n \simeq \frac{n\pi}{L} \sqrt{\frac{\mathcal{T}}{\Sigma\rho}} \quad (2.89)$$

Taking into account only the bending near the top and the bottom and computing the elastic and gravitational energies, one finds the dilution factor in the four wires arrangement:

$$D_V \simeq 2 D_P \quad (2.90)$$

The latter is valid as far as the bending energy along the wire is small with respect to that at the top and bottom, that which ceases to be true for the higher order modes.

The effective mass of the violin n th mode is [71]:

$$\mu_n \simeq \frac{\pi^2 M^2}{2\Sigma\rho L} n^2 \quad (2.91)$$

It is noticeable the fact that μ_n is proportional to M^2 ; this high mass value is the effect of the tiny mass displacement during a violin vibration.

The contribution of violin modes to the thermal noise spectrum is therefore:

$$\langle S_{x,V}^2 \rangle = \frac{4k_B T}{\omega} \sum_{n=1}^{\infty} \frac{\mu_n^{-1} \phi_n(\omega) \omega_n^2}{(\omega^2 - \omega_n^2)^2 + \phi_n^2(\omega) \omega_n^4} \quad (2.92)$$

2.6.2 Test masses thermal noise

The test mass itself contributes to the thermal noise level by means of several different mechanisms [71], [77]. The mass is constituted by a bulky cylindrical substrate with a coated flat face, so in fact, the origin of these mechanisms can be individuated either in the dissipation within the bulk or in the losses associated with the coating.

The thermal noise sources in the substrate are divided in three main branches, Brownian noise, thermoelastic noise and thermal lensing. The Brownian noise comes from the displacement fluctuation of the mirror related to its internal friction, according to the usual formulation of the fluctuation-dissipation theorem. In finding the expression of the bulk Brownian noise spectrum, one has to solve the mirror acoustic wave equation and use the described direct approach (see section (2.1.1)), obtaining [78]:

$$\mathcal{S}_{x,B}^2 = \frac{8k_B T}{\omega} \phi_B \mathcal{F} \quad (2.93)$$

where ϕ_B is the bulk loss angle¹², and \mathcal{F} is a series of Bessel functions with coefficients depending on the material and the mirror and beam spot size geometry.

A mirror bulk thermoelastic noise is also present, due to a coupling between the temperature fluctuations and the mirror elastic strain, thanks

¹²For the structural damping here considered the loss angle has been found experimentally to be approximatively constant in frequency (see section (2.4.2)). A frequency dependent model for the structural losses based on a review of many experimental data has been recently published [79].

to a non-null expansion coefficient α . The fluctuations of the temperature are originated either by laser photon absorption or they are the thermodynamical counterpart of the statement of the fluctuation-dissipation theorem, that at the equilibrium each internal variable undergoes a spontaneous fluctuation. The resulting strain causes heat conduction to dissipate energy in the substrate. Furthermore, in those mirrors which work in transmission, the fluctuation of temperature results in a variation of the refraction index n determining a laser phase noise, which is referred to as *thermal lensing*.

The thermal noise due to the coating layer [80], [81], [82] is similarly divided in Brownian, thermoelastic and thermorefractive contributions. The Brownian noise has in this case the special feature that the coating loss angle ϕ_C is different from that of the bulk, therefore an inhomogeneity is present. Moreover, ϕ_C is assumed to be non isotropic and is written as:

$$\phi_C = \left(\frac{\delta U_{\parallel} d}{U} \phi_{\parallel} + \frac{\delta U_{\perp} d}{U} \phi_{\perp} \right) \quad (2.94)$$

where δU_{\parallel} and δU_{\perp} are surface integrals of the coating energy density components along the parallel and perpendicular direction with respect to the surface, ϕ_{\parallel} and ϕ_{\perp} are the associated loss angles, U is the total stored bulk energy and d is the coating thickness. The values of ϕ_{\parallel} and ϕ_{\perp} are not well known experimentally, so it is customary to rely on the simplifying assumption that $\phi_{\parallel} \approx \phi_{\perp}$. A rough, approximated expression¹³ of the coating Brownian thermal noise is therefore obtained by means of the Levin calculation approach:

$$\mathcal{S}_{x,C}^2 = \frac{2k_B T}{\omega} \frac{d}{\pi Y_B r_0^2} \left(\frac{Y_C}{Y_B} + \frac{Y_B}{Y_C} \right) \phi_{\parallel} \quad (2.95)$$

being Y_B , Y_C the bulk and coating Young's moduli and r_0 is the beam radius. The matching of the Young's moduli $Y_C \simeq Y_B$ corresponds to the lower value of (2.95).

Temperature fluctuations generated thermodynamically or due to laser photon absorption give rise to a thermoelastic coating noise. These fluctuations couple with the laser phase thanks to a non null dn/dT , leading to the thermorefractive component of the coating thermal noise.

A complete and detailed review of all these noise contribution is offered in [78].

¹³It is assumed also, for the sake of simplicity, that the bulk and coating Poisson's ratios σ are negligible with respect to the unity; nevertheless, since usually $\sigma \simeq 0.2$, the latter condition is rather crude.

2.6.3 Thermal noise budget in Virgo

The total thermoelastic noise spectrum is the sum of the suspensions and test masses components formerly reviewed. The thermal noise contribution to the noise budget in Virgo and in the foreseen second-generation detector Advanced Virgo are compared in figures (1.5) and (2.3) with the main non-thermal noise sources.

Virgo employs steel wires ($\phi_S \simeq 10^{-4}$) for suspending the mirrors. The Virgo present status curve in figure (1.5) is dominated by the pendulum noise in a wide frequency band from few Hz up to 50 Hz, where it becomes comparable with the mirror bulk noise which is dominant around 100 Hz. The coating noise is negligible.

In the Advanced Virgo design, the suspensions will be made of fused silica (see chapter (3)), resulting in an improvement of the low frequency sensitivity. Similarly, low-loss substrates will allow a reduction of the mirror bulk noise to negligible levels. On the contrary, the coating thermal noise will become the new dominating noise around 50 Hz: coating Brownian, as well as thermoelastic and thermorefractive components are foreseen to overcome the substrate effects. The sensitivity curve shown in figure (2.3) is a conservative estimation of the noise contributions to Advanced Virgo, based on a monolithic design with cylindrical fused silica fibres. Choosing different geometries, like ribbons or dumbbell fibres, would reduce the pendulum noise level; with heavier mirrors, also the radiation pressure noise would get lower.

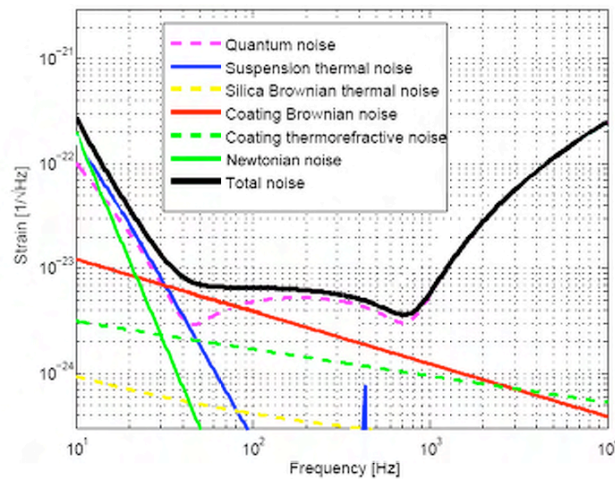


Figure 2.3: Advanced Virgo nominal sensitivity curve, from [28].

Chapter 3

Fused silica fibres for Virgo+ and Advanced Virgo

Future generations of GW interferometric detectors will improve the detection performance in the whole sensitivity frequency band. A specific effort will be made for finding solutions to reduce the thermal noise coming from the test masses and the last stage suspensions [83], [84]. In this chapter, the attention is focused on a material which is particularly interesting for the second generation GW interferometers monolithic suspensions, that is, fused silica [72], [85].

The production of fused silica fibres for realizing monolithic fused silica suspensions for Virgo+ is described [86]. A tool for characterizing the fibres mechanical behaviour, in particular the position of the bending point, is presented, together with a first set of measurements.

3.1 Monolithic fused silica suspensions for the second generation

In the design of advanced GW interferometric detectors, thermal noise represents the most serious sensitivity limitation in the frequency range from a few Hz up to a few kHz. Thermal noise in the suspensions dominates the sensitivity curve up to about 100 Hz.

In the frequency range comprised among the pendulum resonance and the first violin mode of a suspension fibre the power spectral density of the thermal noise displacement of a suspended mirror is computed by means of equations (2.84) and (2.85), and is well approximated by the

following expression:

$$\langle S_{x,P}^2 \rangle = \frac{4k_B T}{\omega^5} \frac{g}{L^2} \sqrt{\frac{Yg}{4\pi n M C_S T_B}} \phi(\omega) \quad (3.1)$$

where L is the suspension fibres length, Y is the Young's modulus of the fibres material, n is the number of suspension fibres for each mirror of mass M , and C_S is the percentile of breaking stress T_B at which the fibre is loaded. The loss angle $\phi(\omega)$ represents the sum of all the dissipative processes which occur in the material (structural and thermoelastic, as described in chapter (2)), plus an effective loss angle taking into account the losses associated with the connecting elements such as clamps or chemical bonded pieces (see section (5.4)).

The suspensions system of the main optics in the current GW interferometric detectors is based on a single or double metal wire loop. A scheme of a cradle-like suspension with two wires is drawn in figure (3.1); note the presence of triangular spacers between the mirror and the wires, assuring a precise knowledge of the wires break-off points position. The presence of spacers is an additional source of losses. In Virgo, C85 steel wires are presently used, with an intrinsic loss $\phi_w \sim 2 \times 10^{-4}$ at 100 Hz and a tensile breaking strength of about 2.9 GPa [87].

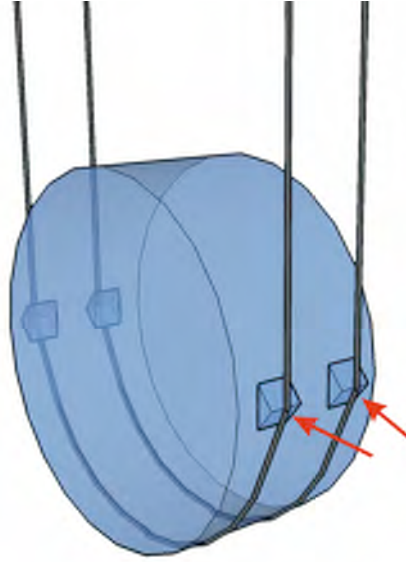


Figure 3.1: Scheme of a double steel wire cradle suspension. The position of the spacers is indicated by red arrows.

Only the GEO600 detector uses a different suspension system, based

on a monolithic fused silica design, while an analogous solution is currently being developed for Virgo. A monolithic suspensions arrangement prevents the friction among wires and mirrors in the cradle-like steel suspension scheme. Furthermore, fused silica is a good material for low thermal noise suspensions [87], [88] because of its low intrinsic loss angle (at room temperature) [89], [90], [91], [92], [93] and its low thermoelastic effect (see section (2.4.1)). The thermoelastic dissipation (equation (2.50)) in fused silica fibres is suppressed by a low thermal expansion coefficient $\alpha \simeq 0.5 \times 10^{-6} \text{ K}^{-1}$ [94], while the high value of the tensile strength $T \simeq 4 \text{ GPa}$ makes large the gravitational dilution (equation (2.84)) [87]. It seems possible that the monolithic arrangement will reduce the suspension thermal noise in the interesting frequency range of about one order of magnitude.

In spite of these positive characteristics, fused silica present some drawbacks, since the tensile strength is dominated by cracks and defects present in the fibre surface and there is evidence of a sort of ageing due to ambient moisture [87].

Monolithic suspensions using fused silica fibres involve the silicate bonding technique described later on, in section (5.4) [85]. Silicate bonding will be employed for chemically glue silica ears to the substrates, allowing the fused silica fibres to be welded on them. A scheme of a possible monolithic assembly to be realized for the future upgrades of Virgo (first of all Virgo+, see section (1.4.2)) is given in figure (3.2). Difficulty arose in testing such kind of arrangement, due to the thermal stress induced in the bonded ears during the fibres welding. Therefore, alternative assembly schemes are now under consideration.

The production and characterization of fused silica fibres is a fundamental issue in the path toward monolithic fused silica suspensions.

3.1.1 Production of fused silica fibres

Silica (SiO_2) is retrievable in nature in two different aggregation states, both transparent, the one with an high grade of internal order, the other showing a disordered clustering of molecular aggregates. The former state is represented by the crystalline quartz, while the latter has a vitreous structure and is properly called *fused silica*. Within the silica molecule, each silicon atom is bonded to four oxygen atoms by covalent bonds. Vitrification temperature of fused silica depends on specific material history and vitrification velocity; it usually lies near 2000 K. Fused silica

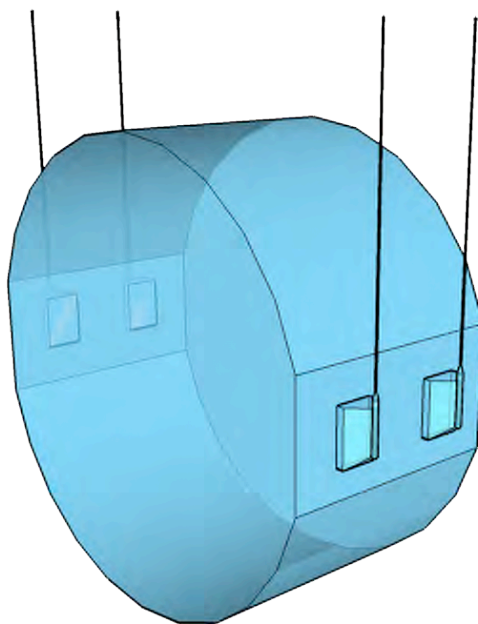


Figure 3.2: Scheme of a possible monolithic fused silica suspension assembly to be realized for Virgo+. Silica ears are attached to the mirror by silicate bonding on flattened sides; then the fibres are welded to the ears.

breaking strength and intrinsic losses have been already reviewed in the previous section; here in table (3.1) other thermomechanical parameters are sketched.

C [J/(kg K)]	κ [W/(m K)]	α [K ⁻¹]
670	1.4	5.5×10^{-7}

Table 3.1: Values of the specific heat C per unit mass, thermal conductivity κ and linear thermal expansion coefficient α in fused silica (from [95],[96]).

Fused silica are currently employed in the realization of optical fibres for telecommunications; nevertheless, since these applications have specifications completely different from the ones here described, the fused silica fibres to be used for monolithic suspensions have to be produced purposely.

The fibres are produced starting from high purity fused silica cylindrical bars commercially available (suitable materials are HERASIL[®] or SUPRASIL[®]), with length ~ 10 cm and 1.5 mm thick. Once melted, fused silica material becomes highly viscous and it can be plastically deformed.

Fibres are thus obtained by melting the central region of the bar and subsequently pulling the two ends apart. This method can be implemented in several ways. Care must be taken in the process for avoiding contaminants to enter the melted material; impurities diffused in it will indeed spoil the tensile strength performances. Moreover, a method capable of producing fibres with reproducible characteristics would be preferable.

Initially and up to now, hydrogen/oxygen flames have been used for melting the bars. Nevertheless, at the moment we are using a different method. A machine for pulling fused silica fibres using a CO₂ laser has been developed at the University of Glasgow [97]. A duplicate of this machine has been assembled in a dedicated laser room at the site of the Virgo experiment. A schematic view of the functional parts of the machine is given in figure (3.3).

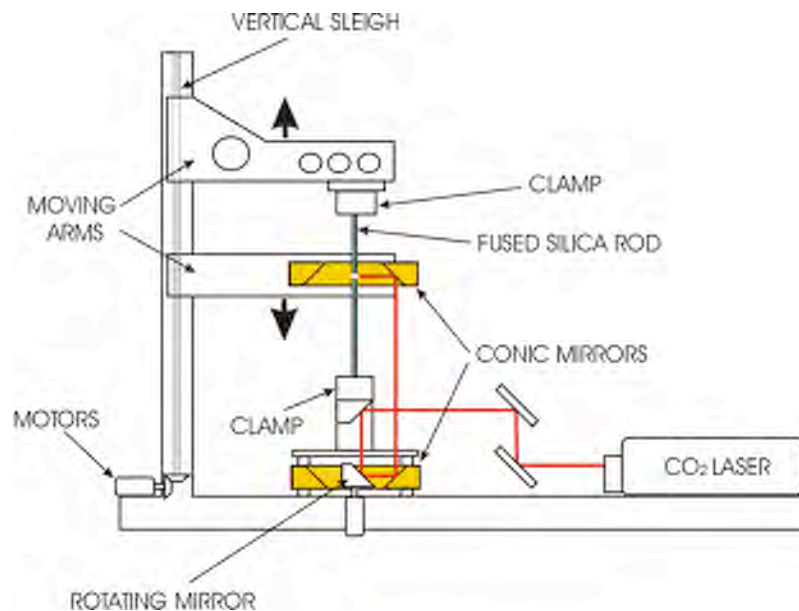


Figure 3.3: Schematic drawing of the CO₂ laser pulling machine described in the text.

The fused silica rod is first cleaned with isopropylic alcohol; then it is clamped at its lower end to a fixed clamp, while it is blocked at the top to a clamping tool rigidly connected to a moving arm. The vertical displacement of this arm is acted by precision motors which are controlled through a computer board, by a suitable software application.

A 100 Watts CO₂ commercial laser with 10.6 μm wavelength furnishes the needed power for melting the rod. The laser beam is delivered onto the fused silica rod by a series of gold coated mirrors. A rotating

45° mirror placed underneath the fixed clamp delivers the beam on a conic mirror, where the beam is reflected toward a second conic mirror which finally directs it to the rod. Thanks to the rotating and conic mirrors, the beam hit the rod continuously all around its axis, assuring an homogeneous local heating.

Once the rod is melt by the laser, the upper arm pulls it upward following a given velocity profile and a thin fibre is produced. The geometry of the pulled fibre depends critically on the chosen velocity profile.

Since the melting involves a small volume of the rod from which the material is driven away during the pulling, new material must be melt in order to feed the fibre. Therefore, the melting point must be shifted downward during the operation. This is the reason why the second conic mirror is fixed to a moving arm analogous to the one hosting the upper clamp; the velocity profile to be passed to the motor is obtained applying the conservation of rod mass through the continuity equation.

When the rods are shipped, though being pure, defects and small cracks are present at the surface and in their volume. Indeed, when a rod is placed in the machine and the beam melts it, usually internal reflections show a diffuse luminosity within the rod and small spots almost everywhere. Such kind of structural defects compromise severely the breaking strength of the obtained fibres. Therefore, an annealing is performed on the fibre before the pulling; the beam is moved up and down along the fibre by moving the lower arm, so that the melted region goes through all the fibre length. This process is repeated until no more diffuse light or spots are present inside the fibre, which therefore appears perfectly transparent.

The clamped rod ends are not melted during the process, so the fibre maintains thick heads. Two small bobs within the heads can be produced before the pulling, melting the rod near the clamps and then shrinking it. These bobs are necessary for allowing a good clamping in all the subsequent operations described in section (3.1.2).

With this method, thin fibres about 1 m long can be produced. The laser pulling allows a very good reproducibility of the fibre shape, as shown in figure (3.4) where the profiles of two fused silica fibres produced subsequently are compared. The profiles are measured using a profiling tool such as the one described in section (4.3.1). For the sake of realizing monolithic suspensions, fibres with a diameter of about 280 μm are pulled, capable of supporting loads as high as 10 kg or more.

There are several advantages in using the laser pulling machine. Though

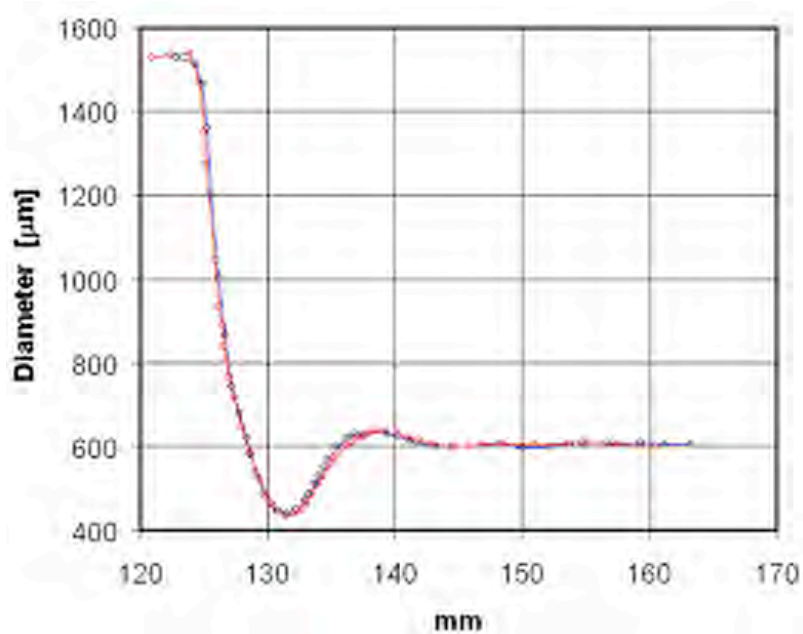


Figure 3.4: Comparison among the measured profiles of two fused silica fibres pulled 45' the one after the other with the CO₂ laser pulling machine. The profile reproducibility is very good. These fibres were not regular, showing a thinner neck. Nevertheless, this problem has been fixed and the fibres presently pulled show a monotonically decreasing diameter near the heads, after which the section is pretty regular.

the laser is at the moment not stabilized, a short term improvement of the system will include a laser power control loop, so that very fine control of quantity and localization of heating will be possible. With respect to the flame method, the contamination of the fibre material is almost completely avoided since no gas is involved in the process. Finally, the laser itself can be used to perform precise welding of the fibres.

3.1.2 Characterization of fused silica fibres

The fused silica fibres produced with the CO₂ laser machine must have the mechanical characteristics requested for realizing a monolithic suspension stage. In particular, they have to support a load of about 5 kg each one, since the mirror mass is 20 kg and 4 fibres are employed in suspending it.

Therefore, a stress test has to be performed once the fibre has been pulled. The test consists in gently hanging to the fibre a 10 kg load and letting the fibre support it for few seconds. The load is progressively released by using a labjack. If the test is passed, the fibre is validated and will be used in the monolithic suspensions arrangement tests.

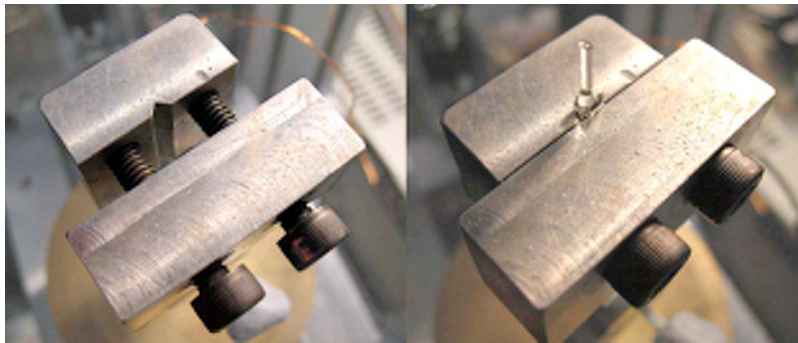


Figure 3.5: Picture of the clamping system used for blocking the fused silica fibres during the load test and the λ measurements. The clamp parts are shown on the left, while a fibre clamped is on the right. Note the small bob in the fibre thick head and the rubber pipe envelope.

The hanging operation requires the fibre to be clamped both at the top to a rigid support and at the bottom to the loaded mass. Therefore, an efficient and strong clamping has to be realized avoiding the ends of the fibre to slide out from the clamp due to the high load. This has been obtained using two aluminum thick slabs pressed together by screws; a triangular groove has been machined onto one of the two slabs, as shown

in figure (3.5). The fibre head is firstly inserted in a fitting rubber pipe, then placed along the groove in the clamp, making attention that the bob has been left out of the clamp, at the opposite with respect to the straining direction. The bob cannot pass through the clamp, so that the fibre slipping is avoided; moreover, the rubber pipe prevents the fibre to break inside the clamp.

With this system, a produced fibre strength is validated; now, a characterization of its mechanics is needed, allowing a full knowledge of the dynamic behaviour of the future monolithic assembly.

A three segments model of the fibres

In order to design and successfully realize a monolithic fused silica suspension assembly, a very precise knowledge of its dynamical parameters is needed, so that the structural mechanical resonances can be optimized for the best active control performance of the whole mass suspension system.

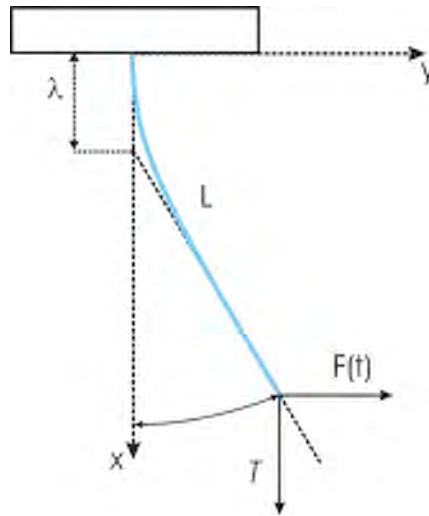


Figure 3.6: Scheme of the deformation of a fibre once it is pulled apart by a force $F(t)$. The pendulum mass is supposed pointlike. The pendulum swings with an effective length smaller than the real length L by the amount λ .

A fundamental dynamical parameter of a cylindrical suspending fibre is its bending length λ (equation (2.80)):

$$\lambda = \sqrt{\frac{YI}{T}} \quad (3.2)$$

Following the definition, λ represents the distance of the fibre bending point from the clamped end, when the fibre pendulum mode is on¹. Consider a force $F(t)$ applied horizontally to the lower end of the fibre supporting the load \mathcal{T} (figure (3.6)). The horizontal displacement $y(x, t)$ along the fibre obeys the equation [42], [98]:

$$YIy'''' - \mathcal{T}y'' = \rho \frac{\partial^2 y}{\partial t^2} \quad (3.3)$$

where ρ is the mass density, Y the Young's modulus, I the cross sectional moment of inertia and each apostrophe stands for a derivative with respect to the position x along the fibre. In the case of harmonic excitation $F(t) = F_0 \exp^{i\omega t}$ and sufficiently small ω for the right hand side of equation (3.3) to be neglected, one finds:

$$y(x) = \frac{F_0 \lambda}{\mathcal{T}} \left[\exp^{-x/\lambda} + \frac{x}{\lambda} - 1 \right] \quad (3.4)$$

The resulting fibre shape exponentially approaches two lines at the fibre ends; the crossing point of the two lines identifies the bending point. If the suspended mass is not point-like, a similar bending happens also at the fibre bottom.

The given expressions for $y(x)$ and λ hold for a regular fibre with constant cross sectional moment I . Nevertheless, the fibres pulled by the CO₂ laser machine are not regular, since they present a tapered profile near the heads (the so called *neck* region) which is different among the two heads due to the pulling procedure. Different values are thus expected for the bending length at the top and at the bottom of the fibre; the mechanical behaviour of the fibre is obtained by applying the beam equation (3.3) with a varying $I(x)$. Nevertheless, this is a very complicate approach, especially when the dynamics of the whole suspensions system are concerned.

By knowing the bending length at both the ends, a simple model of the fused silica fibre can be built, using just three rigid, massless sections of length λ_t , L and λ_b , respectively the top bending length, the distance among the bending points and the bottom bending length (see figure (3.7)). This model is able to give the correct values of force and torque on the suspended mass. A computation of the proper angular frequencies gives:

¹The bending length is relevant not only for the pendulum motion, but also for the violin modes, as discussed in section (2.6.1).

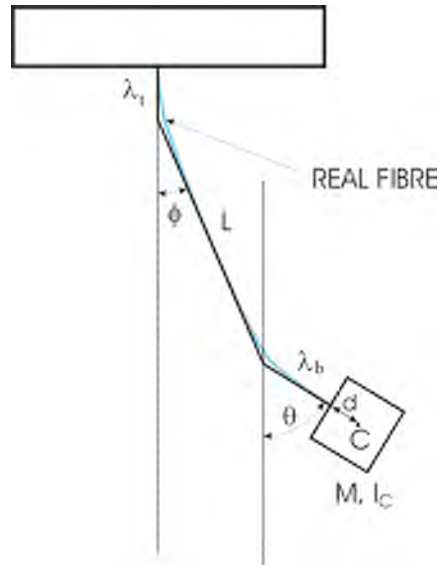


Figure 3.7: Scheme of a simple model of a fused silica fibre, based on a three segments pendulum.

$$\omega_{\pm}^2 = \frac{g}{2LI_C} \left(l^2M + I_C + lLM \pm \sqrt{(l^2M + I_C + lLM)^2 - lLMI_C} \right) \quad (3.5)$$

where I_C is the moment of inertia of the suspended mass with respect to the center of mass C , $l = \lambda_b + d$ where d is the distance between C and the fibre connection point, M is the mirror mass and g is the gravity acceleration. Note that, letting $l \rightarrow 0$, one has:

$$\omega_+ = \sqrt{\frac{g}{L}}, \quad \omega_- = 0 \quad (3.6)$$

so that as expected only the pendulum mode survives. Clearly, ω_- corresponds to the rocking mode.

This model provides a simple constitutive relation for the suspensions fibres, to be used in the detailed calculations of suspension system dynamics and proper frequencies. Therefore, the bending points enter the expression of the suspension mechanical transfer function, which is used for projecting the suspensions active controls.

The knowledge of λ is strictly needed for a successful control design. As an example [99], in the monolithic suspensions realized for GEO600,

the estimated bending point position was wrong by about 1 cm. The designed feedback models for the suspensions resulted not to be sufficiently accurate and the locking of the interferometer was rare and depended strongly on the environmental conditions, so that a new seismic isolation system had to be installed. The alignment problems were traced back to a pitch coupling among the longitudinal motion of the suspension point and the tilt of mirrors. The latter can be prevented by placing the bending point as close as possible to the horizontal plane passing through the mirror center of mass. The GEO600 experience taught a severe lesson on the importance of the knowledge of the fibres parameters, especially the bending length.

Bending point measurement

Since in general $\lambda \neq \lambda_t, \lambda_b$, the position of both the bending points of the produced fibres must be evaluated experimentally. In principle, the measurement of the bending point is quite simple. Consider a fibre blocked at its top to a rotary stage, supporting a load² \mathcal{T} . If the bending point is placed exactly on the rotation axis of the stage, when the top head of the fibre is rotated, the bottom part of it actually does not move (see figure (3.8)). If instead the bending point does not correspond to the rotation center, the fibre body moves in different directions depending on whether the bending point is above or below the center.

A specific apparatus has been realized to perform the measurement of λ , which is shown in figure (3.9). A rotary stage, mounted at the top of a rigid structure, is driven by a controllable motor; on the stage, a second motor acts on a micrometric sleigh moving along a diameter of the rotary stage. This motor can be controlled by means of a joystick. On the sleigh, a clamp is placed for blocking one head of a fused silica fibre. The exact position of the center of rotation is found by inserting in the hollow shaft of the rotary stage a steel bar on which a cut is machined indicating precisely the rotation axis.

At the bottom of the fibre, a load is clamped and released gently by means of a labjack. Once suspended, the loaded mass starts to swing at the pendulum frequency. The pendulum motion is damped with a PVC bar fixed to the load mass and inserted in a rubber pipe (see figure (3.10)); the pipe is in frictional contact with the floor, even when the mass is lifted

²Since the position of λ depends on the tension, \mathcal{T} has to be chosen as close as possible to the foreseen working load. In this case, a load of 5.1 kg is employed.

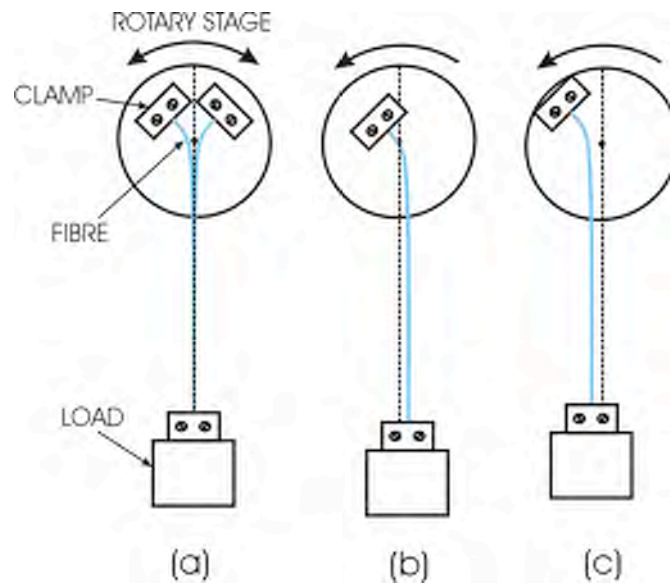


Figure 3.8: Description of the experimental setup for measuring the position of the bending length. (a) The bending point is exactly on the rotation axis: the lower part of the fibre does not move away from the vertical line. (b) and (c) The bending point is not centered on the axis: the lower part of the fibre moves horizontally during the rotation.

or released.

The movements of the fibre are detected following the displacement of the fibre shadow, projected by a LED diode on a double photodiode. The photodiode is split in two elements by a thin insensitive gap and the fibre is placed in face of the gap. The signals coming from the two photodiodes are subtracted and amplified; the output becomes negative or positive if the fibre moves, following its oscillation. The advantage of tilting the photodiodes of about 45° with respect to the vertical axis is explained in figure (3.11). The displacement signal is then displayed on a screen.

Once the load is suspended, the rotary stage motor is started and driven with a square-wave signal, so that a small oscillation of the fibre head occurs. If the acquired signal from the shadow sensor indicates that the fibre bottom is moving, a small displacement of the fibre head along the micrometric sleigh is produced acting with the joystick, trying to reduce the fibre movements. When these movements get their minimum amplitude³, then we know that the bending point is on the rotation axis.

³Though actually the movements when the bending point is on the axis should

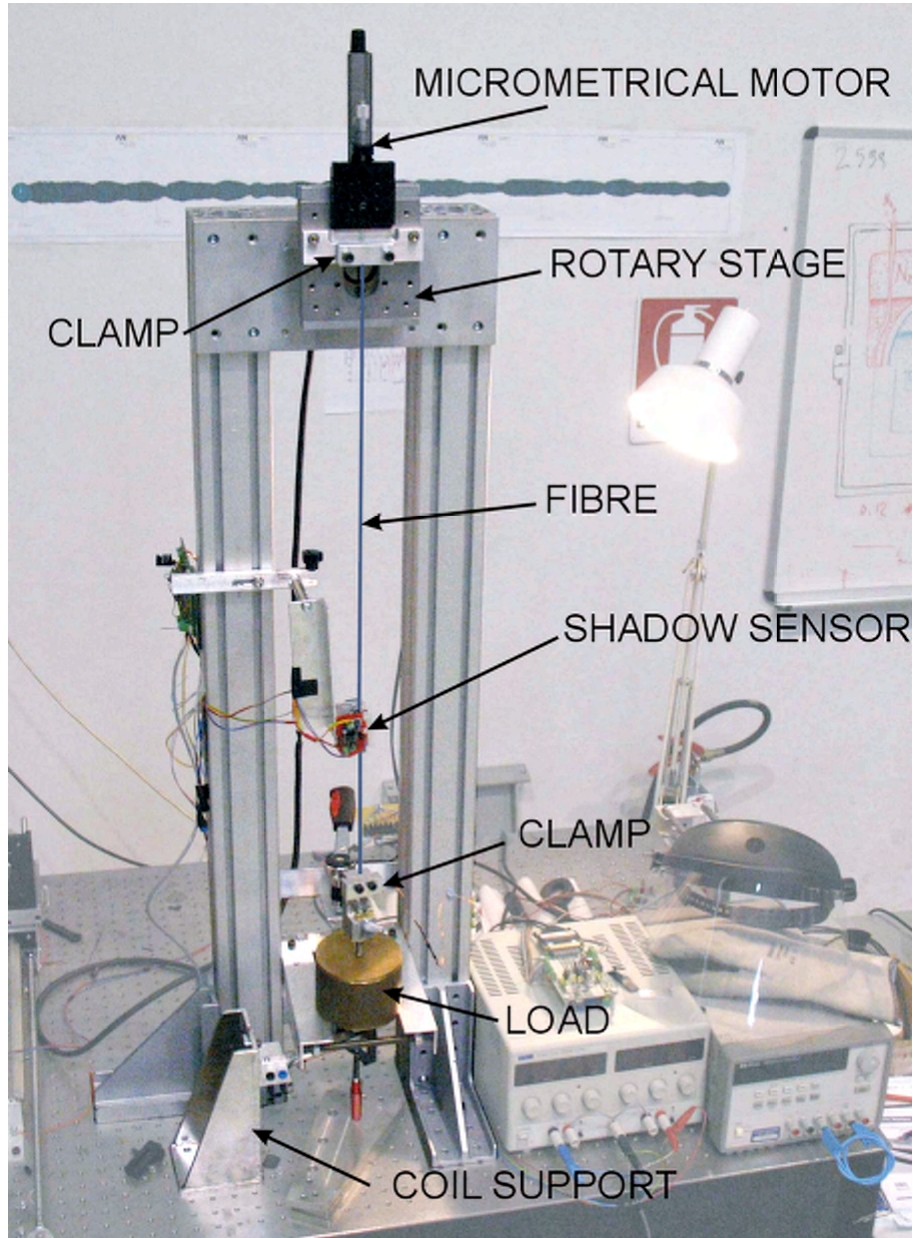


Figure 3.9: Picture of the bending point measurement apparatus.

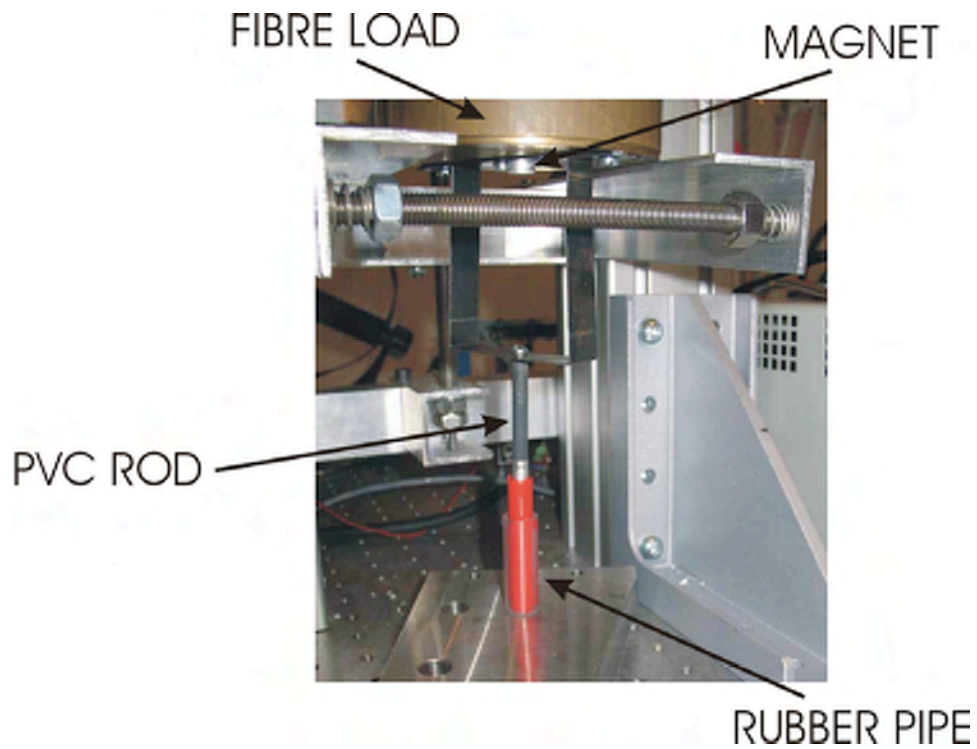


Figure 3.10: Picture of the rubber tool used to damp the pendulum swing of the suspended mass.

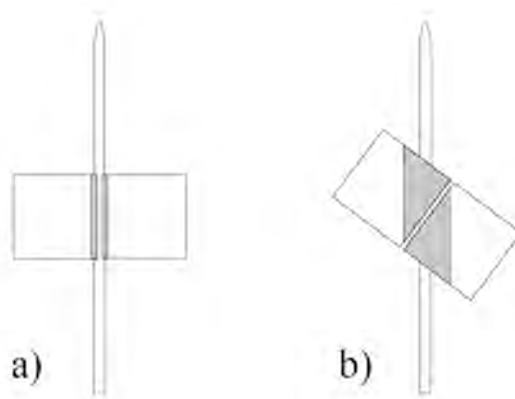


Figure 3.11: Possible configurations for the read-out system, with the photodiode gap (a) parallel and (b) tilted with respect to the fibre axis. The gray areas represent the sensitive regions for a good detection.

Thus, the rotary stage is blocked and the distance among the rotation center signalled by the steel bar and the upper end of the fibre is measured using a caliper. In this way, the bending point position is evaluated with respect to the fibre tip.

During all the measurement procedure, great care must be taken in avoiding to touch the fibre. In fact, even a very soft touch would cause cracks or defects to be produced on the surface, spoiling the tensile strength so that the fibre would break when suspended.

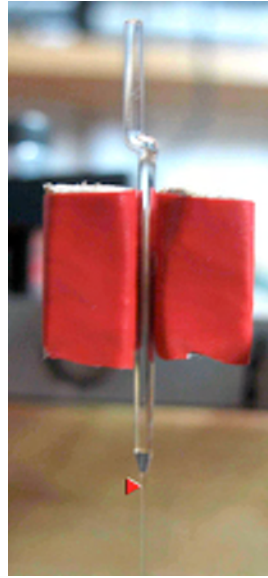


Figure 3.12: Pictorial display of the measured position of the bending point, indicated by a red arrow.

A test measurement has been performed on a 74 cm long fibre pulled by the CO₂ laser at the Virgo site. The obtained position of the bending point is shown pictorially in figure (3.12). It has been possible to calibrate the shadow sensor signal by moving the micrometric stage during the oscillations by a known amount, and observing the acquired signal amplitude. The measurement uncertainty has been thus estimated evaluating the residual minimum oscillation when the bending point is found, then converting it in length. It has been found eventually, for the fibre considered above, that $\lambda_t = 36.64 \pm 0.04$ mm measured with respect to the tip.

vanish, the accuracy of the micrometric sleigh movements is not enough for reaching a perfect centering.

Other mechanical parameters

Due to the fact that the fibre section is not constant, other mechanical parameters must be measured directly since their analytic expression would be too complicate to find.

The machine which has been built for measuring λ can be advantageously employed for obtaining an evaluation of the fibre violin first mode f_v (equation (2.89)) and of the bouncing mode frequency f_b (equation (2.86)).

The violin mode can be measured just gently hitting the clamp support with an hammer and observing the FFT of the shadow sensor signal. A peak is observed in the frequency spectrum, and performing a long lasting acquisition a precise measurement of the frequency position of the peak is obtained. For the measured fibre, $f_v = 444 \pm 1$ Hz, assuming as uncertainty the width of the recorded peak.

To measure the bouncing mode, a specific setup has been realized. A magnet is rigidly fixed underneath the suspended mass (see figure (3.10)), while a coil is mounted on a support and placed close to the magnet. The coil-magnet force driven by a sinusoidal current is used for exciting the bouncing oscillation. The coil is feeded with a swept sine current with frequency ranging from few Hz up to 10 Hz, since the bouncing mode is expected to be around 6 Hz. In this way, the bouncing mode is excited. The read-out of the mass oscillation is obtained by means of a 1 cm piezoelectric rod, having one end clamped to the suspended load and the other fixed to a small mass. The voltage coming from the piezoelectric sensor is amplified and acquired by a computer board. When the excitation force is removed, a long lasting acquisition of the read-out signal is used to perform a FFT allowing the evaluation of the bouncing peak position. For the considered fibre, we found $f_b = 6.1 \pm 0.1$ Hz.

3.2 Conclusions

Monolithic fused silica suspensions will be realized probably in time for being used in Virgo+, and they will be part of Advanced Virgo.

The CO₂ machine is able to pull fused silica fibres with a good control on the diameter value and regularity; the pulled fibres show a remarkable diameter reproducibility. The necessity of measuring all the relevant mechanical parameters of the fibres has been stressed, particu-

larly in relation with the experience of GEO600. The presented tool for measuring the bending point is now ready to perform a full characterization of the pulled fibres, before they are welded to the ears attached to the test masses. The welding procedure depends on the design of the monolithic assembly, which is currently under study (as discussed at the beginning of this chapter); the fundamental request is that the bending point must be placed in correspondence with the mirror center of mass. At the present status, a problem could be represented by the fact that the bending point position is known with respect to the fibre tip; when the welding is performed, the fibre head is deformed⁴ and the bending point is no longer referable to the tip. Several solutions depending on the welding procedure are under consideration.

As next step, fibres produced with the CO₂ laser machine will be employed in realizing monolithic suspensions tests. Using the λ -machine, a complete dynamical characterization will be carried over a statistically significative set of fibres to be used in monolithic assemblies.

⁴Depending on the welding procedure, the fibre head can be intentionally broken for fitting with the ears geometry.

Chapter 4

Silicon suspensions for third generation detectors

The suspensions of cryogenic interferometers will be probably made of silicon [100], [101], [84]. In this chapter, a method of production of silicon crystalline fibres is presented. The grown silicon fibres are then measured in order to study their internal dissipation. The dissipation indeed enters the expression of the thermal noise spectrum as seen in chapter (2). Therefore, an experimental setup for measuring the fibres loss angle within the frequency band concerned in the GW detectors is described and the obtained room temperature measurement results are discussed.

The produced fibres show a not perfectly regular geometry. Therefore, a facility for realizing a 3D model of the fibre is also presented. The 3D model has been used for a dynamical finite element analysis allowing a comparison between the experimental results and the model outcomes. In this way some physical parameters of the fibres have been extracted.

Finally, the problem of the fibre clamping is addressed, proposing solutions for the foreseen cryogenic measurements on the fibres.

4.1 Silicon as a promising material for the third generation

Long baseline GW interferometric detectors of the second generation will optimize the level of thermal noise at room temperature, by a suitable choice of low loss materials and a monolithic mounting solution [102], [103].

According to the fluctuation-dissipation theorem (2.1), the overall

thermal noise power spectrum depends directly upon the temperature. Thus in view of the realization of a third generation of GW interferometric detectors a cryogenic approach is currently under study.

As for the second generation, a gain in sensitivity against photoelectron shot noise will be obtained by increasing the circulating power. In the cryogenic perspective, this would request the suspensions to have a high thermal conductivity in order to allow the heat deposited in the mirrors to be extracted efficiently. Moreover, the heat absorption by the mirror would cause a deformation with extent proportional [104] to α/κ and, consequently, a lensing effect (thermal lensing, see section (2.6.2)). This effect could be source of optical mismatch and even cause instabilities of the interferometer. Thus, the thermal conductivity of the substrate is also requested to be high.

Fused silica fibres are not suitable for cryogenic suspensions due to a peak in the dissipation at around 40 K [84], and to the low value of the thermal conductivity which reduces the heat extraction capability. The latter argument is also valid for silica substrates.

New materials have to be singled out for matching these requests. Very low levels of internal friction feature in most crystals; these materials have structural loss angle as low as, or even lower than silica (see section (3.1.1)) but, due to their relatively large thermal expansion, the thermoelastic loss dominates by far over the sensitive frequency range. For this reason, crystalline materials have never been considered suitable for the construction of low thermal noise suspensions at room temperature. Despite being crystalline, silicon seems to be promising for realizing cryogenic suspensions and test masses, as detailed below.

4.1.1 Thermomechanical properties of silicon

Silicon thermal and mechanical properties are extremely favorable for realizing low thermal noise suspensions of a cryogenic GW interferometric detector [105], [103].

The high conductivity of silicon is particularly useful for extracting the heat deposited within the mirrors. In an interferometer operating at cryogenic temperatures, with about 1 MWatt of circulating power and mirrors with absorption at the level of few ppm, silicon ribbons with a cross section between 175 mm² and 47 mm² in a monolithic arrangement are suitable for extracting the sufficient amount of heat with just 2 K of temperature difference across 0.7 m of suspension ribbons [102].

Silicon is expected to have large bulk tensile strength (about 7 GPa, dominated by surface effects that can decrease that value down to about 200 MPa [106]) and low intrinsic loss angle ($\phi(300 \text{ K}) \simeq 2.8 \times 10^{-8}$, $\phi(77 \text{ K}) \simeq 5 \times 10^{-9}$ and $\phi(4.2 \text{ K}) \simeq 6 \times 10^{-10}$ [107], [108]). It does not show plastic deformation and it is almost insensitive to fatigue.

Recall the given expression (equation (2.50)) for the thermoelastic contribution to the overall loss angle:

$$\phi_{th}(\omega) = TY \frac{\alpha^2}{c_V} \frac{\omega \omega_{th}}{\omega^2 + \omega_{th}^2} \quad (4.1)$$

where:

$$\omega_{th} \propto \frac{2\pi\kappa}{d^2 c_V} \quad (4.2)$$

and κ is the thermal conductivity, α is the linear thermal expansion coefficient, d is the thickness of the fibre, c_V is the specific heat per unit volume and Y is the Young's modulus.

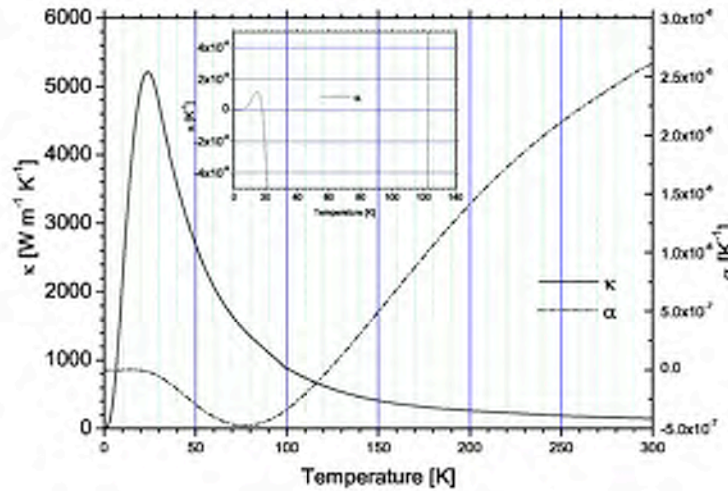


Figure 4.1: Thermal conductivity (continuous line) and linear thermal expansion coefficient (dash-dotted line) of silicon (from [109],[110]), with inset a magnified plot showing where α crosses 0 at about 18 K.

The behaviour of α and κ for silicon is peculiar [111], as displayed in figure (4.1). The thermal expansion coefficient decreases with temperature until it vanishes at about 123 K, is negative in the temperature interval among 18 and 123 K, and almost zero at lower temperatures. This means that the thermoelastic dissipation decreases sharply with the temperature and becomes negligible with respect to the structural

losses in the range $120 \div 130$ K and below 20 K, as shown in figure (4.2).

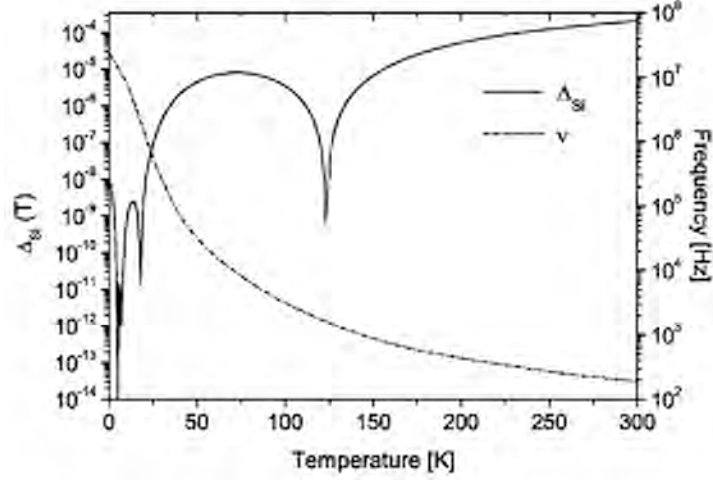


Figure 4.2: Amplitude of the linear thermoelastic loss angle in a silicon fibre plotted versus the temperature. Ideally, at the two temperatures where the thermal expansion coefficient vanishes Δ_{Si} is null. The expected temperature dependence of the thermoelastic peak frequency $\nu = \omega_{th}/2\pi$ in a $560 \mu\text{m}$ diameter silicon fibre is also shown. The frequency increase at low temperature should contribute to reduce the thermoelastic dissipation due to the suspensions.

Peaks in the intrinsic loss angle of silicon have been reported [112] in correspondence with the two temperatures for which α vanishes; it is not known at the moment if these intrinsic loss peaks are related to the zeros in α and further studies are required.

The thermal conductivity κ of silicon increases at low temperature pushing the thermoelastic peak toward higher frequencies, as plotted in figure (4.2). Therefore, the thermoelastic peak would fall out of the sensitivity frequency band of the interferometric detectors. After reaching a maximum, the thermal conductivity drops as explained in section (5.1). The position and height of the maximum of the curve of conductivity, though, depends critically on impurities, dimensions and doping in the region below ~ 100 K. The necessity of measuring the values of κ at low temperatures for the particular silicon specimens considered is discussed in chapter (5). Nevertheless, the latter argument is generally valid since the curve of κ maintains its qualitative trend.

In figure (4.3) the plot of the specific heat per unit mass $C_V = c_V \rho$ of silicon versus the absolute temperature is also shown.

The sources for suspensions thermoelastic noise are mostly in flexural

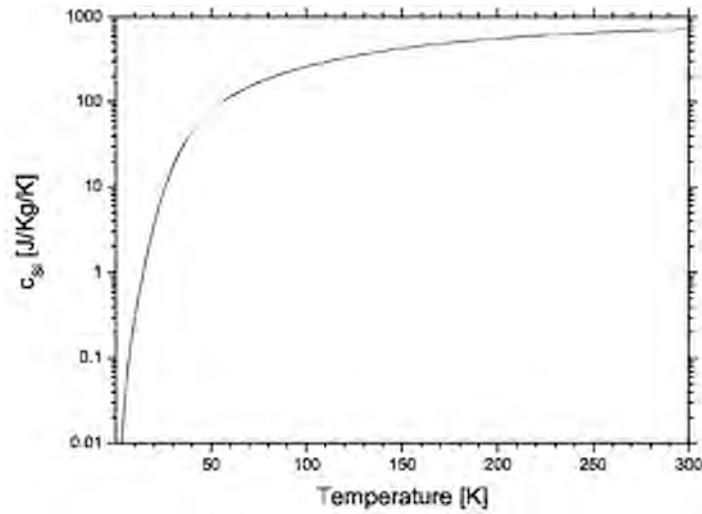


Figure 4.3: Specific heat per unit mass of silicon plotted versus temperature.

points of fibres; a partial thermal noise reduction can be obtained just cooling these points. Beside to classical methodologies, silicon allows to investigate the possibility to cool or control the temperature of a doped silicon fibre using an anti-Stokes fluorescence mechanism [113], [114], [115], [116]. The most interesting dopant is Yb^{3+} , which has been employed for cooling vitreous and crystalline doped matrices, obtaining a maximum temperature reduction of about 65 K with respect to room temperature [117]. Therefore, the study of the effect of dopants on the thermal and mechanical characteristics of silicon and the control and optimization of doping will be of great importance.

For the outlined scheme of third generation GW detectors, the choice of substrate material is limited to silicon [118], [119] and calcium fluoride [102]. Silicate bonding among silicon elements has been proved to be possible (see further, section (5.4)). The pure silicon is transparent in the range $1300 \div 8000$ nm, and presently technical components are available and reliable for realizing transmissive silicon optics at a wavelength of 1500 nm. Also, a wholly reflective optics configuration would be studied in alternative [120].

Crystalline silicon fibres must be realized and characterized in view of their use as mirrors suspensions in a cryogenic, high power interferometer design. It is convenient to produce custom fibres in order to be able to control all the steps of their realization checking the influence of production items, the feasibility of section shaping and the thermo-

mechanical performances. Controlling the production line will allow to vary the type and level of doping, so that an experimental study of the anti-Stokes fluorescence will be possible.

We used a crystal growing Czochralsky [121] furnace for producing silicon crystalline fibres and we measured their loss angle at room temperature [122]. The low temperature loss measurement are foreseen as the next step in this path.

4.1.2 Production of crystalline fibres with micro-pulling down technique

Silicon fibres matching the discussed design can be produced by using known methods of crystal growth. A dedicated research facility has been developed in an INFN Pisa laboratory. The PISA crystal growth furnace uses the so-called micro-pulling down technique (μ -PD) for producing thin (few millimeters), regular crystalline silicon fibres. Basically, the μ -PD method consists in downward pulling of pure material melt in a crucible, through a micro-nozzle placed at the bottom of the crucible (see figure (4.4)). It is an improvement of the classic Czochralski method used currently for growing semiconductor crystals [121]. The facility crucible is made with materials capable of remaining stable at very high temperatures such as the melting point of silicon (about 1700 K at standard pressure [87]). The crystalline material is placed in the crucible and the melting is induced by heating the crucible with a RF generator; then, at the first stage, a silicon seed crystal produced in previous experiments or cut from a bulk crystal is inserted in the crucible orifice. Once a contact is set with the melted material, the seed is pulled downward; the fused material is driven through the nozzle at the bottom of the crucible and cools down forming a new fibre. The method allows to grow crystalline fibres, rod or ribbons with diameters in the range of 0.15-5 mm at variable pulling rates.

The adjustment and tuning of the temperature gradients in the proximity of the nozzle can be done by applying an after-heater under the crucible, allowing thus the regulation of the position of the solid-liquid interface.

The shape and location of the growth interface is one of the most important parameters determining the quality and uniformity of the resulting crystal. A CCD camera is employed for viewing the solid-liquid interface at the meniscus region.

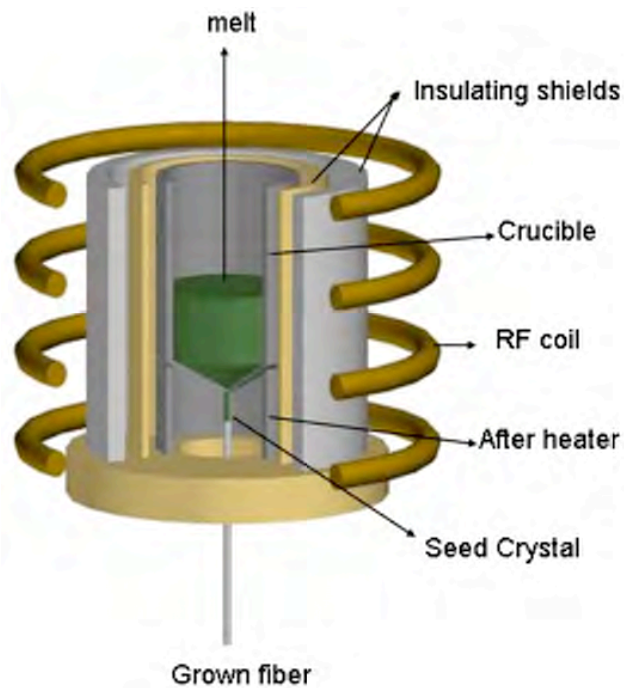


Figure 4.4: Scheme of the apparatus for the μ -pulling down growth of fibres.

The fibres growing facility has been tested with several materials and about 20 silicon crystalline fibres have been already grown, with diameters ranging between 0.4 and 3 mm and maximum length around 310 mm.

Growth process

The starting material was silicon (pure to the level of 10 ppm) in small pieces of typical dimensions of few millimeters. These pieces were inserted in a vitreous carbon crucible held by a zirconate pedestal in a vertical alumina ceramic tube. Cylindrical heat shields made of alumina or zirconate ceramics were placed around the crucible.

The calibrated orifice at the bottom of the crucible was about 0.5 mm in diameter. To avoid the oxidation of the crucible, the crystals were grown in Ar atmosphere of 10 ppm purity.

Seeding and growth procedure

Several Si single crystals with different lengths and diameters were grown. A $\langle 100 \rangle$ oriented thin cut from a Si disk was used as a seed. The crystals

were grown at various pulling rates in the range $0.3 \div 2$ mm/min.

The growth of long crystal fibres is affected by vibrations which become especially intense at longer length. It has been found that the length of crystals oscillations also depends on the fibre diameter [122]. Few abrupt changes in diameter and/or temperature happened, probably due to instabilities of the RF generator and to reactions between silicon and the crucible. Anyway, for most of their length the grown fibres show good quality. A capture of the growth process taken with the CCD camera is shown in figure (4.5).

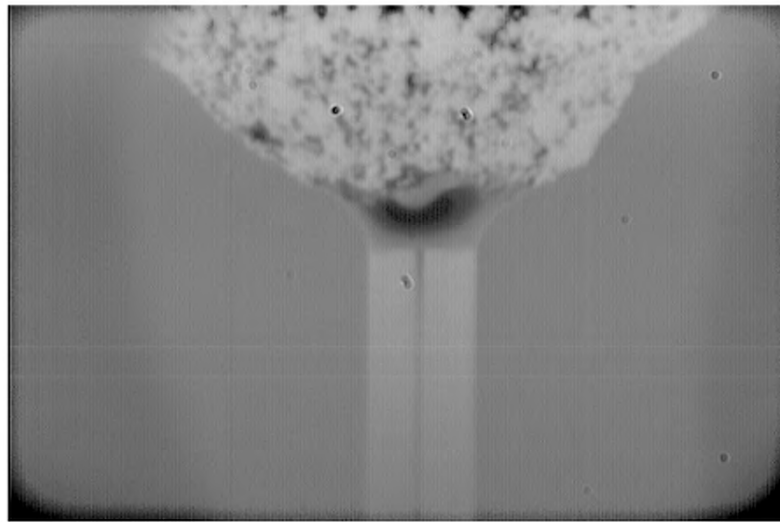


Figure 4.5: Picture of the growing fibre at the crucible orifice, taken with the CCD camera.

Two typical silicon crystal fibres, grown with different diameters and lengths, are shown in figure (4.6). The crystal orientation of the fibres was determined using the X-ray Laue diffraction method. From this measurement it is possible to say that the inspected fibres showed single crystalline character (figure (4.7)), but it was found that the crystal orientation changes along the fibre in every point in which the diameter is not stable. The fibres are thus composed of several monocrystalline segments.

Absorption investigations did not show the presence of any volume contaminants within the sensitivity of the apparatus.

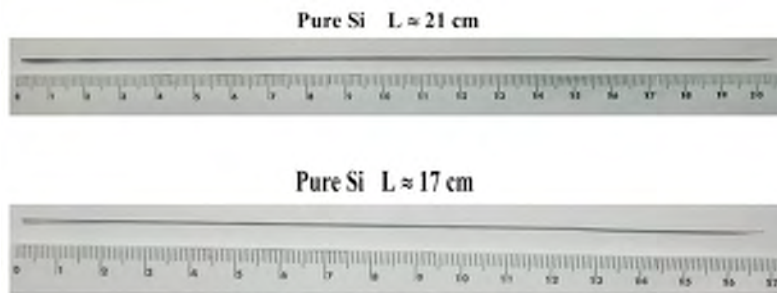


Figure 4.6: Pictures of two crystalline silicon fibres with grown with the μ -pulling down method described in the text. The average diameter of both fibres is ≈ 0.4 mm.

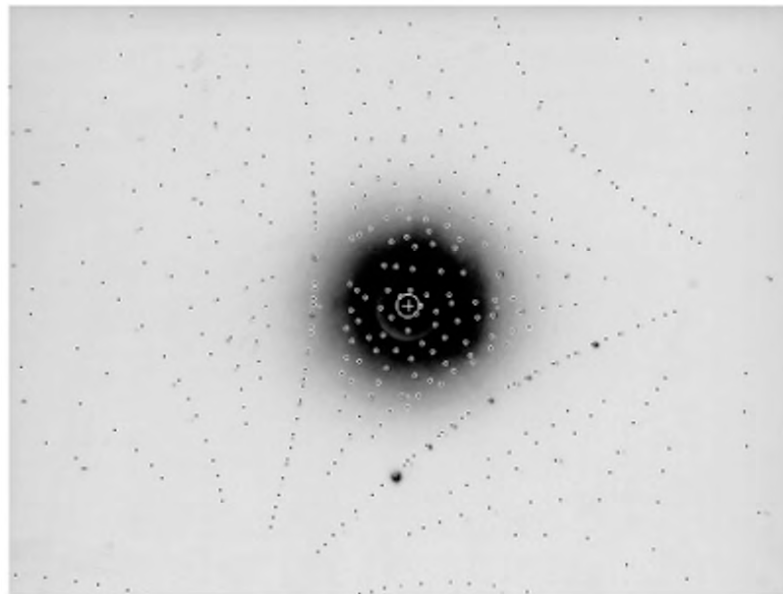


Figure 4.7: Laue X-ray diffraction pattern for the grown silicon fibres. Crystal orientation is determined from the position of the spots. The Laue technique can also be used to assess crystal perfection from the size and shape of the spots.

4.2 Loss angle measurement description

The thermomechanical characterization of the grown fibres requires their loss angle to be measured, stressing the thermoelastic contribution and deducing the bulk dissipation. Also, the determination of physical parameters as Young's modulus, thermal expansion coefficient and thermal conductivity as a by-product of the latter analysis is possible. In this section, the measurement principle and the apparatuses employed in this activity are described.

4.2.1 Measurement principle

The loss angle $\phi(\omega)$ of a body is experimentally deduced by its response to an oscillating solicitation at angular frequency ω . The response can be viewed in terms of Fourier transform, that is, a regime oscillation, or in terms of Laplace transform inspecting the transient, once the solicitation is removed. Consider therefore the first type of analysis: the presence of loss determines a phase lag in the response with respect to the excitation, which is the loss angle itself. Nevertheless, measuring such phase lag is difficult, especially when the loss angle is very tiny as it is the case for the considered materials. The same conclusion would be valid if one would try to measure the resonance width, which is proportional to ϕ .

On the other hand, one can observe the damping of the excited oscillation once the excitation is removed. If the oscillation is driven at a normal mode frequency ω_0 , the damping envelope is an exponential decay whose rate is proportional to the loss angle at that frequency. Indeed, as discussed in section (2.3), if the internal resonance is modeled as a simple harmonic oscillator with losses, one has (equation (2.31)):

$$\phi(\omega) = \frac{\omega}{Q\omega_0} \quad (4.3)$$

so that at the resonance ω_0 a simple relation holds:

$$\phi(\omega_0) = \frac{1}{Q} \quad (4.4)$$

being Q the quality factor of the resonator. The solution of the damped one-dimensional resonator has the form:

$$x(t) = A \exp^{-\frac{t}{\tau}} \sin(\omega_0 t) \quad (4.5)$$

for a given amplitude A . The damping time τ is proportional to the quality factor:

$$\tau = \frac{2Q}{\omega_0} \quad (4.6)$$

Therefore, provided that the oscillation of the body is recorded, the loss angle at each normal mode frequency can be obtained by measuring τ and computing:

$$\phi(\omega_0) = \frac{1}{Q} = \frac{2}{\tau\omega_0} \quad (4.7)$$

Repeating the measurement for n normal modes allows the loss angle to be obtained at the corresponding n frequencies. The frequency dependence of ϕ can be eventually worked out by fitting the measured points with a suitable loss model, e.g. a thermoelastic Debye peak over-imposed to a constant loss level.

4.2.2 Experimental apparatus

The scheme of the apparatus realized for measuring the loss angle of the produced silicon crystalline fibres is shown in figure (4.8). It is made of four parts with specific functions. A vacuum chamber prevents the oscillating fibre from being damped by the air viscosity. A rigid, massive clamp allows the fibre to be blocked at one end, minimizing the recoil energy loss. The measurement is performed using an electrostatic actuator and a shadow position readout system.

Vacuum system

As seen in section (2.5.2), the loss angle measurements can be spoiled by the presence of a gas around the vibrating fibre. The gas viscous drag in this case dissipates most of the mechanical energy. Therefore, the air pressure around the measured fibre must be reduced in such a way that the contribution to the fibre loss angle due to the air damping is negligible.

The stand supporting the fibre clamping system is placed on a bench inside a vacuum chamber (figure (4.9)) equipped with pass-through connectors and optical windows. The pressure inside the chamber is measured with a conduction manometer.

Two pumps arranged in cascade produce the vacuum inside the chamber. A first rotative stage brings the internal pressure down to about $6 \cdot 10^{-2}$ mbar; once this value has been reached, a turbo-molecular pump

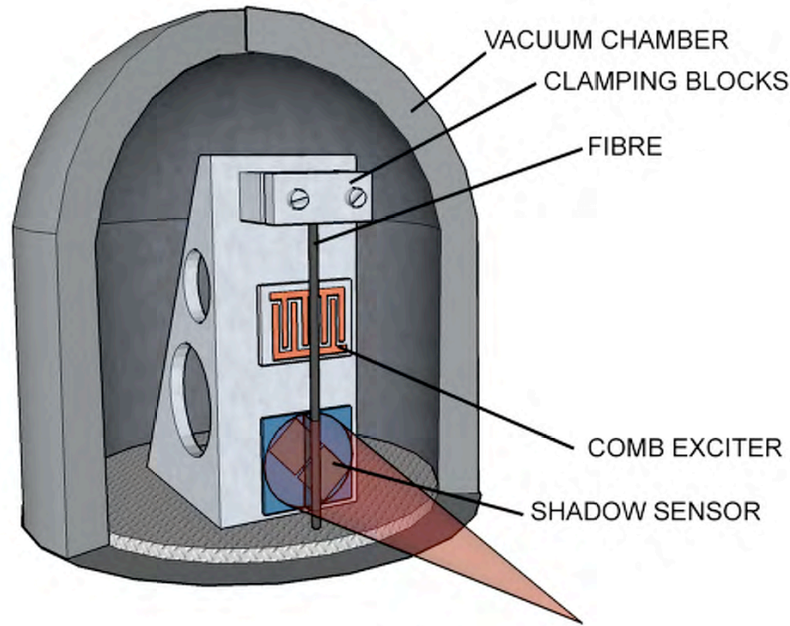


Figure 4.8: Model of the experimental apparatus for loss angle measurements. The dimensions of the parts are not in scale.

stage can be started. The turbo-molecular pump rotor reaches a regime condition with 36000 rpm in about 15 minutes. Thanks to the turbo-molecular stage, the lowest attainable pressure is about 10^{-7} mbar and it is usually reached within two days. Nevertheless, already at $P = 10^{-5}$ the air friction is negligible in the interesting range of frequencies (see figure (4.10)).

The two pumps are connected to the vacuum chamber through semi-rigid tubes, avoiding their vibrations to be directly transmitted to the rigid structure clamping the fibre. Nevertheless, we observe peaks in the vibration spectrum of the fibre, mainly at 50 Hz and 600 Hz which are the rotating frequencies of the pumps.

Clamping stand

A crucial point in loss measurements is generally represented by the clamping system [123], [124], [125]. A limit on the measured loss angle is determined by the energy which is transferred and then dissipated within the clamp, as discussed in section (2.5.1). In addition, stick-slip friction and several other processes can take place in the clamp, which are difficult to evaluate and keep under control. Sliding and stick-slipping of

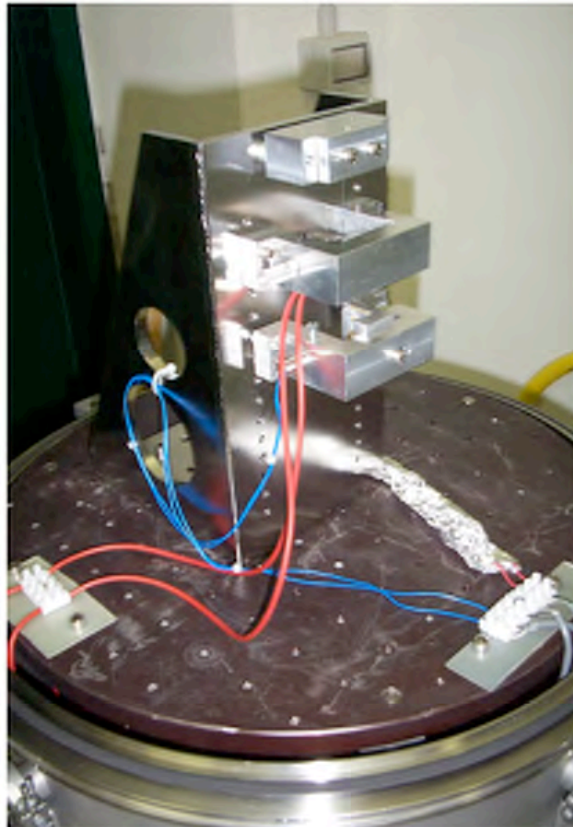


Figure 4.9: Picture of the stand supporting the fibre clamp. The two C-shaped aluminium parts fixed to the stand hold the excitation system and the displacement sensor. The stand is placed on an optical bench hosted in a vacuum chamber.

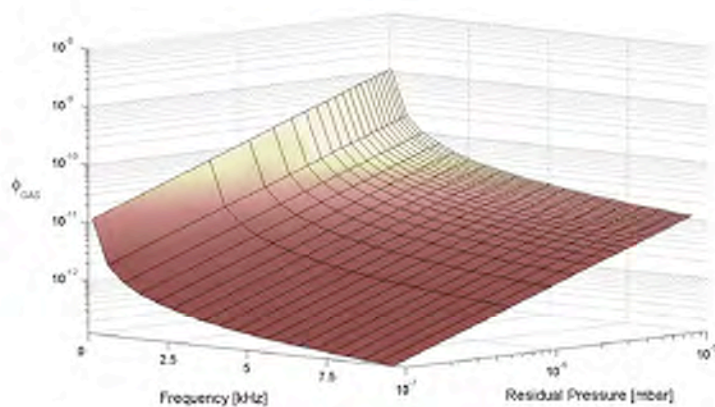


Figure 4.10: Surface plot of the loss angle due to air friction, for a silicon cylindrical resonator with diameter $d = 1$ mm. The computation has been performed using equation 2.79. The loss angle is plotted as a function of the air pressure and of the resonant frequency.

the clamped sample must be avoided as much as possible.

In our set up, the fibre is blocked in vertical position, by clamping its upper end to a rigid, massive steel stand (see figure (4.8)). The fibre head is tightened between two aluminium flat blocks, fixed rigidly to the stand. If the sample is softly tightened, it can move among the blocks giving rise to sliding friction and stick-slipping; if it is tightened too much it can be damaged or broken. A special care must therefore be taken in tightening the clamp, repeating the clamping procedure if the measured losses are dominated by spurious frictions.

Even if the clamp is suitably tightened, mechanical coupling to the support is always present. It is better therefore to avoid measurements near the resonance modes of the stand-clamp structure (of the order of several kHz).

Excitation system

The described measurement method requires the fibre resonant modes to be excited selectively. Neglecting the gravity, the purely elastic modes of an unloaded cylindrical bar clamped at one end have frequencies given by [126]:

$$f_i = \frac{1}{2\pi L^2} \sqrt{\frac{YI}{\rho S}} \alpha_i^2 = \frac{d}{8\pi L^2} \sqrt{\frac{Y}{\rho}} \alpha_i^2 \quad (4.8)$$

where L is the length of the bar, d the diameter, S and I the section and the cross section moment of inertia, Y and ρ are the Young's modulus and the density of the bar material, and α_i are the solutions of:

$$\cos(\alpha) \cosh(\alpha) + 1 = 0 \quad (4.9)$$

A very good approximation for α_i values is [126]:

$$\alpha_i = \begin{cases} 1.8755 & i = 1 \\ (i - \frac{1}{2})\pi & i \geq 2 \end{cases} \quad (4.10)$$

These formulae are useful for guiding the search of resonance frequencies in a real, non perfectly cylindrical fibre. A comparison between the values in equation (4.8) and the measured set of modes provides information about the regularity of a fibre.

The fibre has to be excited at the desired frequency; this is necessary both in a preliminary stage to determine the resonance frequencies and in the measurement stage to excite the known modes.

The employed excitation system makes use of the polarization of the dielectric material the fibre is made of; the fibre is placed into a high gradient electric field $\vec{E}(\vec{x}, t)$ sinusoidally variable with time. The effect of the electric field is to generate a force¹ on the fibre which is proportional to $|\vec{E}|^2$, thus driving an oscillation at an angular frequency which is twice that of the field. For avoiding this discrepancy between the frequency of the exciting field and that of the induced force, one can add a constant field \vec{E}_C to \vec{E} . Otherwise, the angular frequency of the exciting field must be set at half of the desired resonance.

The exciter is composed by two electrodes with opposite polarity in shape of coplanar combs, arranged in such a way that each comb teeth is placed between two teeth of the other comb (refer to figure (4.8)). The fibre is faced near the plane of the exciter, among two neighbouring teeth, where the field gradient is almost maximum and parallel to the comb. In this way the fibre is forced to oscillate perpendicularly to its length.

The voltage signal transmitted to the comb electrodes has a peak-to-peak amplitude of 700 V, to which a continuous voltage of 400 V can be over-imposed.

¹This force is obtained as the field \vec{E} times the induced polarization \vec{P} , which is in its turn proportional to \vec{E} .

Read-out system

The movements of the vibrating fibre are detected with a shadow sensor like the one described in section (3.1.2).

Since the read-out system is able to detect the movements of the fibre at only one point, care must be taken in placing the shadow sensor far from a nodal point where the amplitude of the oscillation for a given mode is null.

The cables with the output voltage from the photodiodes are bound by grounded aluminium foils, shielding them from the electro-magnetic noises induced by the high voltage cables of the excitation system.

In a further improvement, two shadow sensors are placed near the fibre on two orthogonal planes, in order to detect the vibration in two directions x and y normal to the fibre axis. This double device allows the motion on the cross-sectional plane to be reconstructed. That is especially useful for checking the geometry of the measured modes with irregular fibers (see after, section (4.3)).

Measurement procedure

The output of the shadow sensor is referred to the ground of the system and acquired.

First of all, the position of the fibre is measured in DC, in air. The shadow sensor can thus be centered so that a null signal is recorded when no excitation is feeded.

After the centering, a search of the resonance frequencies set is performed with the sample under vacuum. The frequencies can be found looking at the response of the fibre to an excitation sweeping in frequency. The FFT of the signal from the shadow sensor is visualized on a spectrum analyzer, where the resonance peaks are identified thanks to their persistence after the sweeping excitation is passed away. Usually, the resonance modes are measured up to 10 – 15 kHz. At frequencies well beyond that values, the damping time is too short (less than ~ 3 seconds) for detecting a resonance, even with very high Q .

Once the set of resonances ω_i is known, the standard Q measurement is performed for each mode. In order to isolate the single Fourier component of the output corresponding to ω_i , the sampled signal is filtered sharply around the resonance with a digital lock-in filter which provides a further amplification. The lock-in frequency is chosen at about 1 Hz from the resonance, so that the filtered oscillation is shifted at low fre-

quency allowing a low acquisition rate to be employed. A by-product of this technique is that the recorded files are small and handy even for very high values of τ_i . The acquisition of the ring-down of the fibre oscillation is started immediately after the interruption of the excitation. The acquisition extends for a time at least of the order of the characteristic damping time $\tau_i = 2Q/\omega_i$.

The resulting acquired samples vector is shown in a plot and its amplitude shall follow an exponential damping.

To obtain an estimate of the quality factor of the single measurement, a computer program makes a Hilbert transform \hat{x} of the filtered signal $x(t)$:

$$\hat{x}(t) = -\frac{1}{\pi} \int_{-\infty}^{+\infty} \frac{x(s)}{t-s} ds \quad (4.11)$$

The Hilbert transform yields a phase lag of $-\pi/2$ for the positive components of $x(t)$, leaving their amplitude unaltered. Assuming that:

$$x(t) = A \exp^{-\frac{t}{\tau_i}} \sin(\omega_i t) \quad (4.12)$$

the Hilbert transform results:

$$\hat{x}(t) = -A \exp^{-\frac{t}{\tau_i}} \cos(\omega_i t) \quad (4.13)$$

Once $\hat{x}(t)$ has been extracted, the program computes $\mathcal{Z}(t) = x(t) + i\hat{x}(t)$ and gets the envelope of the oscillation calculating the squared modulus:

$$|\mathcal{Z}(t)|^2 = A^2 \exp^{-\frac{2t}{\tau_i}} \quad (4.14)$$

Extracting the logarithm of the envelope one obtains a linear function of t :

$$R(t) = \ln(|\mathcal{Z}(t)|^2) = 2 \ln(A) - 2\frac{t}{\tau} \quad (4.15)$$

The output signal should therefore be a straight line. Performing a linear fit leads to the best value of the slope $\gamma = -2/\tau$. The estimate of Q is then obtained as:

$$Q(\omega_i) = -\frac{\omega_i}{\gamma} \quad (4.16)$$

Several measurements are performed for each resonance frequency and the average value is computed. The error is evaluated as the standard deviation on the measurements set, assuming that no systematics are present. This error usually ranges from 1% to 5%, while the contribution coming from the linear fit is at the level of 1%.

4.3 Fibre modeling

The silicon fibres which have been produced as described in section (4.1.2) do not have a perfectly cylindrical shape. In fact, the diameter changes along the fibre axis z ; furthermore, the cross section is more similar to an ellipse, whose axes are variable in orientation along z .

In order to compare the experimental results with the theoretical predictions of thermoelastic losses, one needs to have a geometrical description of the fibre. The thermoelastic formula (2.49), valid for a vibrating cylindrical fibre, is no longer accurate for the grown fibres. It is necessary therefore to model the fibre; a careful measurement of the profiles along the fibre axis for different angular orientations is needed. Then, once the geometry is known, a finite element analysis can be performed.

4.3.1 Profile measurement apparatus

The fibre to be measured is clamped as it is during the loss measurement and the clamp is blocked on a stand so that the fibre lays horizontally (see figure (4.11)). The stand is free to slide on a rail in the direction of the fibre axis.

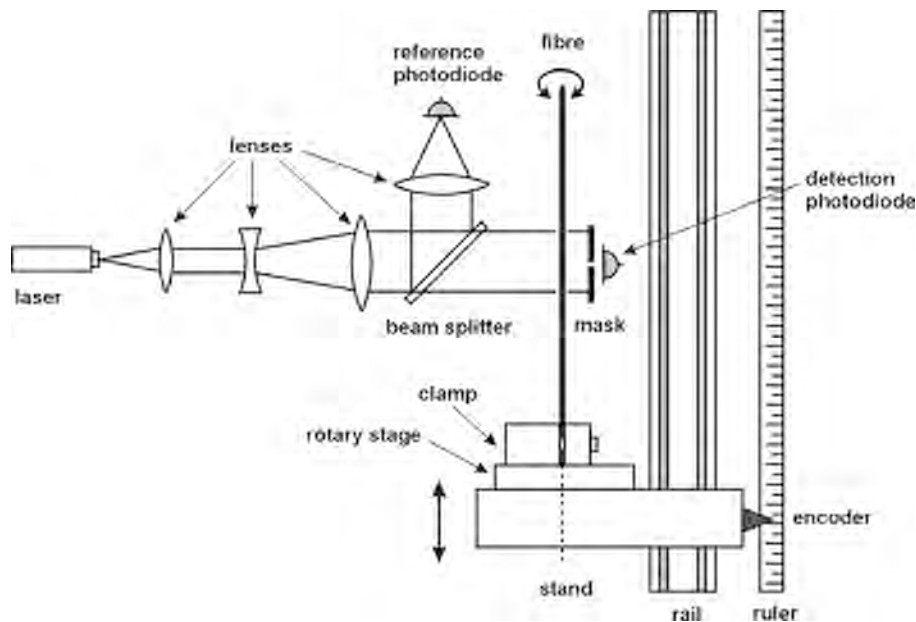


Figure 4.11: Scheme of the apparatus used for obtaining a 3D model of a fibre.

The displacement of the stand along the rail can be recorded by means

of an encoder, reading a rigid metallic ruler parallel to the rail.

A laser LED source, modulated at 1360 Hz, is placed at the focus of a converging lens, so that a parallel beam is obtained. The beam is widened by means of a telescope obtaining a plane wave with a large spot size. The spot is employed for lighting the fibre in a point and projecting its shadow on a photodiode.

The detecting photodiode is partially masked so that the laser detection is allowed only in a narrow strip orthogonal to the fibre shadow. A beam splitter is used for partially reflecting the laser beam before it reaches the fibre, focusing the spot on a third photodiode used as intensity reference.

The signal produced by the masked photodiode is a measurement of the projected diameter of the fibre. If that signal is divided by the output of the reference photodiode, one gets rid of intensity oscillations of the source. The signal acquisition is triggered by the displacement encoder, so that the diameter is recorded at each half millimeter along the fibre. The signals coming from the main and reference photodiodes are filtered around the modulation frequency before being recorded.

The acquired fibre profile is stored in a file. Then, the fibre is rotated around its axis, thanks to a rotary stage on the stand, by a known amount and a new measurement of the profile is performed. Eventually, a 3D model of the fibre has been obtained, with measured diameter values every 0.5 mm along the axis and every 30° around.

The data coming from the profile measurements are pure numbers, taken as ratios between the signal coming from the detection photodiode and the reference one. Therefore, they need a calibration to be converted in diameters.

The calibration is done as follows. A series of wires of known diameters is measured with the profiling apparatus, obtaining a profile like that shown in figure (4.12). If the diameters of the wires are d_i , and the measured ratios R_i are taken to be the averaged values of the oscillations in each step, the calibration gives six couples (d_i, R_i) which can be fitted with a straight line $R(d)$:

$$R(d) = \alpha d + \beta \quad (4.17)$$

so that the calibration parameters $\alpha < 0$ and $\beta > 0$ can be extracted. Therefore, the fibre diameter is obtained as:

$$d = \frac{R - \beta}{\alpha} \quad (4.18)$$

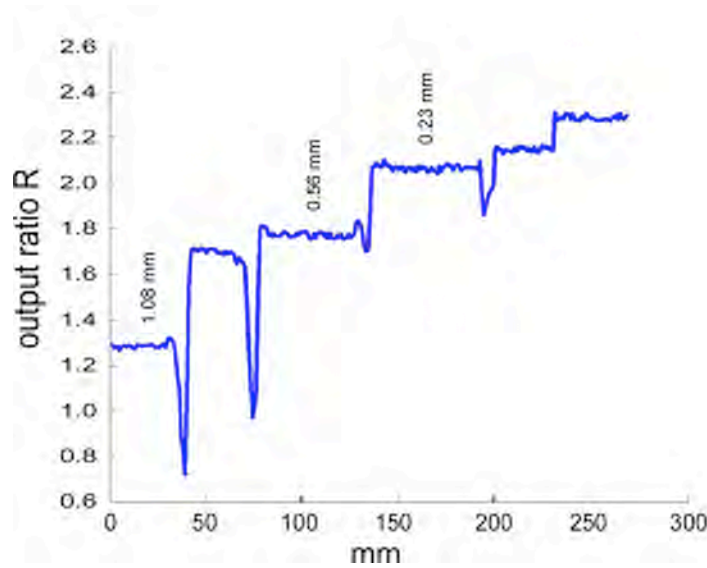


Figure 4.12: Profile of the series of wires used for calibrating the profiling apparatus. Note that the smaller is the diameter, the larger is the output ratio R . The large downward spikes are due to welding bobs at the joining of different wires.

The associated error is:

$$\sigma_d^2 = \frac{1}{\alpha^2} (\sigma_R^2 + d^2 \sigma_\alpha^2 + \sigma_\beta^2) \quad (4.19)$$

An estimation of this error gives $\sigma_d \simeq 100\mu\text{m}$, that is about 10%, dominated by the σ_α^2 term.

Even though the estimated error is quite high, during the profile measurement we had the impression that such error was overestimated, since we found a very good reproducibility (figure (4.13)). Therefore, an independent profile measurement was needed.

An independent method have been used for testing the precision of the profiling apparatus, which is more precise but extremely slow. It resides on the possibility of taking several photos of the fibre profile with a digital camera set on a microscope. The photos are then elaborated digitally obtaining a black and white template of the fibre (figure (4.14)). An image analysis code is used for processing the template in such a way that the profile in pixels is obtained. The error of this method is a composition of the error on the pixel/mm conversion factor and the error on the position of the fibre edge in drawing the template. In figure (4.15), the data obtained with the camera profile and the standard procedure are shown for a part of a silicon fibre. The supposed overestimation of the error in the standard procedure (red bars) is here evident. This is

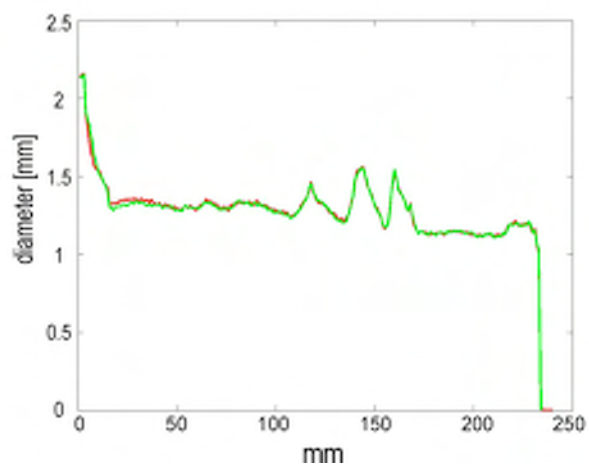


Figure 4.13: Plot of two subsequent profile measurements of the same fibre, at the same angle. The measured diameter shows a very good reproducibility.

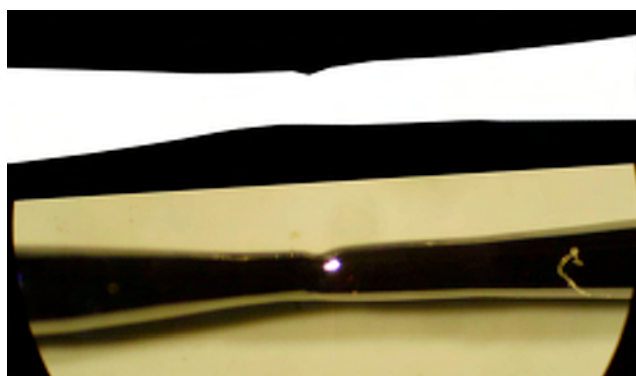


Figure 4.14: Bottom: picture of a small part of a silicon fibre, taken at the microscope. Top: template of the fibre obtained by the picture.

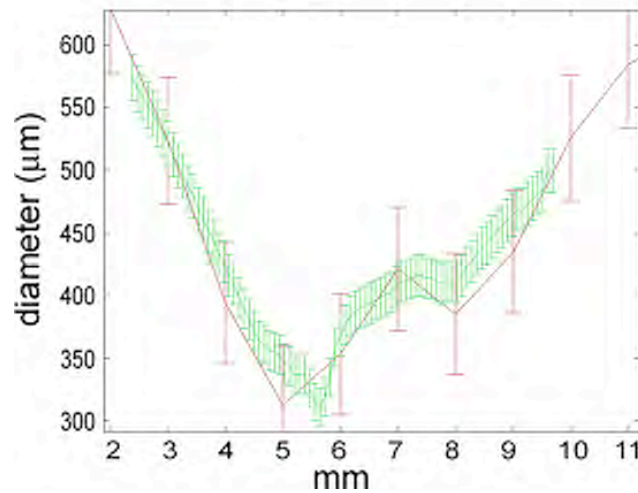


Figure 4.15: Comparison between profile measurements on the fibre segment of figure 4.14, obtained with the digital camera (green line with little bars) and with the standard procedure (red line with big bars).

the case for all the regions inspected along the fibre. Thanks to the agreement found, it seems reasonable to scale the error on the standard profile measurement to the value coming from the camera profiling, i.e. 3.5%.

4.3.2 Modeling the fibre with ANSYS

From the data obtained with the profiling apparatus, it is possible to reproduce a 3D model of the fibre to be used for a finite element analysis (FEA). In the following paragraphs the fibre modeling procedure is briefly reviewed, while a complete description of the simulation steps is given in [78].

Profiles

As formerly explained, the outcome of the profiling measurement is a group of six vectors containing the profiles of the fibre every 30° of rotation around the fibre axis. The displacement encoder is not able to sense the absolute position but just the differential displacement during the stand sliding; therefore, each vector has a starting point which is slightly different in position from the subsequent one. To match the fibre profiles it is necessary to manually align them; the profiles are aligned at the free

end of the fibre. The resulting profiles are shown in figure (4.16) for a 177.5 mm-long fibre. Although it is evident that the fibre is not a perfect cylinder, the various profiles are very similar to one another.

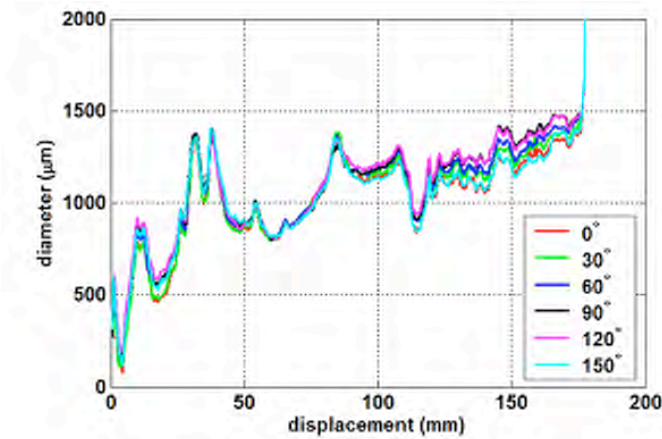


Figure 4.16: Profiles at various section angles are shown for a 177.5 mm-long silicon fibre. The alignment of the different data sets have been performed by manually shifting them to the origin of the plot, where the free end of the fibre is.

Shadow-projection correction

The laser shadow sensing systematically overestimates the diameter at the various angles, since, due to the fact that the fibre is not a perfect cylinder, the shadow produced by the fibre does not correspond to the exact normal section of the fibre at the given angle (this effect is clearly explained by figure (4.17)). As a result, elliptical sections are distorted toward a peanut-shell shape.

A corrective algorithm has been developed to correct the introduced bias. It is based on the idea that the real section of the fibre is contained inside the envelope of all the projection directions of the shadows. The algorithm of projection correction is explained graphically in figure (4.18).

The aligned, corrected profiles are then used for FEA. A 3D model of the fibre is made with a mesh of volume elements, and physical properties such as density and elastic constants are selected. The boundary conditions, that is, free and clamped ends, are also fixed. A part of the resulting fibre model is shown in figure (4.19).

The model is ready to perform a modal analysis on it. In the modal

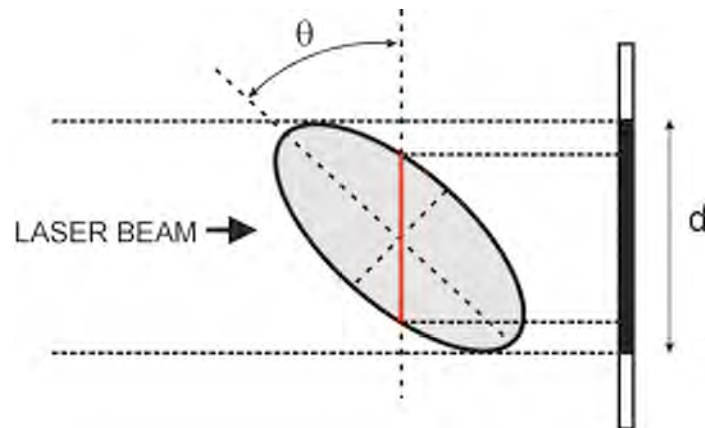


Figure 4.17: Shadow projection of a non cylindrical fibre. It comes clear from the scheme that the profiling system detects at an angle θ a diameter d instead of the normal diameter (red thick line).

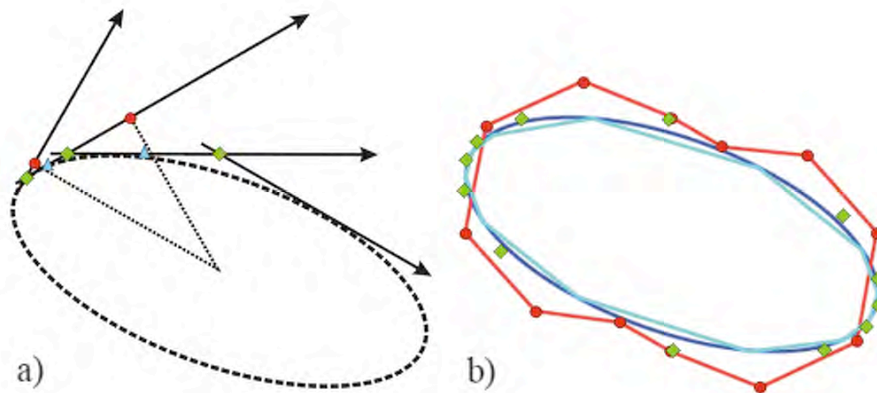


Figure 4.18: (a) Correction of the estimated fibre section from profile measurements. Two consecutive shadow projections identify construction points (the green squares). The new estimated section points (cyan triangles) are chosen to be the midpoints of the segments delimited by the green squares. (b) A comparison among the true section (in blue), the fake estimation (in red) and the corrected one (in cyan) is given. Clearly, the peanut-shell deformation has been corrected.

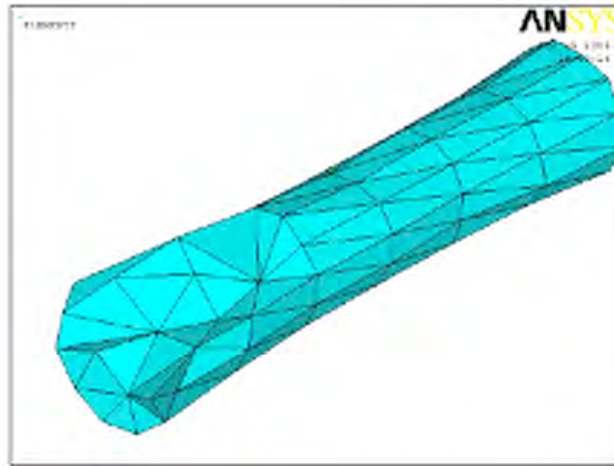


Figure 4.19: View of the elements of a fibre model. Some of them are removed to allow the vision of the underlying elements.

analysis the software extracts the frequencies and the shapes of the resonance modes. It allows also the user to look for stress and strain distribution on the surface or inside the simulated objects.

4.4 HNA etching procedure

In section (2.4.3) the relevance of the loss mechanisms introduced by surface impurities has been highlighted. Such losses are even more important in the case of thin fibres, where the ratio S/V becomes large. Oxides or handling damages are located within a thin layer on the surface of the fibres, contributing to the overall loss angle with a constant term. When a grown silicon fibre is inspected, an opaque gray skin is present on it; it is due to the presence of silicon oxides and silicon carbide, formed in the interaction between the growing fibre and the furnace crucible. Probably, many other impurities and polluting materials are present in the outer layer. If this layer would be removed, one should observe an overall reduction of the dissipation.

Now, it is possible to operate on the grown fibres with a chemical process called etching. It consists essentially of a bath in a chemical solution that acts on the surface of the fibre removing atom layers. It allows the fibre to be polished from surface contaminations.

The etching process modifies also the geometry of the fibre, by reduc-

ing its diameter. The etching can be performed even selectively. It can be realized only on certain parts of the surfaces, shielding the rest with a layer of enamel like nail varnish.

On the one hand, it is convenient to lower the fibre diameter for exploring the parameter space of the thermoelastic effect, whose frequency peak depends on the diameter. In fact, the growth of fibres with diameters below 500 μm is very difficult, due to technical issues in the micro-pulling down process.

On the other hand, the profile can be shaped in order to reduce the clamp losses. Masking with enamel one end of a mm-thick fibre during the etching results in a bigger head which allows a better clamping, shifting the most solicited parts of the fibre to a region which is far from the clamp itself. If the fibre part near the clamp is heavily solicited, indeed, a large amount of mechanical energy is transferred to the support enhancing the spurious losses.

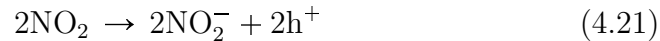
The used chemical solution is called HNA and is obtained by mixing fluoridric acid (HF at a 49% concentration), nitric acid (HNO_3 at a 70% of concentration) and water or acetic alcohol (CH_3COOH). The HNA solution is used for performing an isotropic etching on silicon.

Etching occurs via a redox reaction followed by the dissolution of the oxide by HF that acts as a complexing agent. The reaction is schematized as:

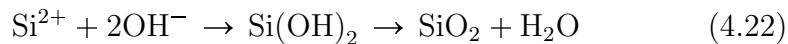


Points on silicon surface randomly become oxidation or reduction sites. These act like localized electrochemical cells, sustaining relatively large currents. It is important to note that for the considered solution each point spends on the average the same amount of time being an anode or a cathode site, leading to an isotropic etching, that is, the corrosion velocity of the material should be the same in all directions.

The nitric acid gives birth to NO_2 , which is reduced at a cathode site producing free holes:



The silicon gains two positive charges at the anodic sites becoming Si^{2+} . The formation of oxide is therefore obtained from the dissociated OH^- :



and the oxide is then dissolved by HF to form a water soluble complex H_2SiF_6 . The nitric acid is therefore fundamental for the reaction to be

allowed; it is produced continuously in an autocatalytic cycle which is boosted by the presence of HNO_3 undissociated. Since the acetic acid is less polar than water, it determines a minor dissociation of HNO_3 , and that is why it is conveniently included in the HNA solution. Furthermore, for the same reason it helps achieving proper wetting of the fibre surface.

The fibre is immersed in horizontal position in a long basin filled with the HNA solution. It has been found that if the fibre is vertically immersed the etching is no longer isotropic. In the latter case, the solution temperature at the top of the fibre rises up; possibly, the reaction at the bottom is slowed by the inert products falling down. Otherwise, it can happen that light products are carried upward modifying the distribution of reactants.

After a first rough etching lasting some minutes, a second immersion is performed for a time which has been calculated to reduce the diameter to a chosen value. Nail varnish can be used at this stage for masking a part of the fibre, for instance the head. After the etching, the varnish is removed by means of acetone. The fibre is finally dipped into a pure HF solution for removing the oxide which may still be present on the surface.

A picture showing the difference between a grown fibre with opaque skin and an etched fibre with a clean blue surface, is presented in figure (4.20).



Figure 4.20: Microscope comparative view of two fragments of silicon fibres, the one still not etched (top), the other after the etching (bottom).

The reaction velocity of HNA etching depends on the concentrations

of the solution components. A diagram of reaction velocities is shown in figure (4.21) as they vary with relative concentrations. The circle marks the actually used solution with 75% HNO_3 , 15% HF and 10% CH_3COOH .

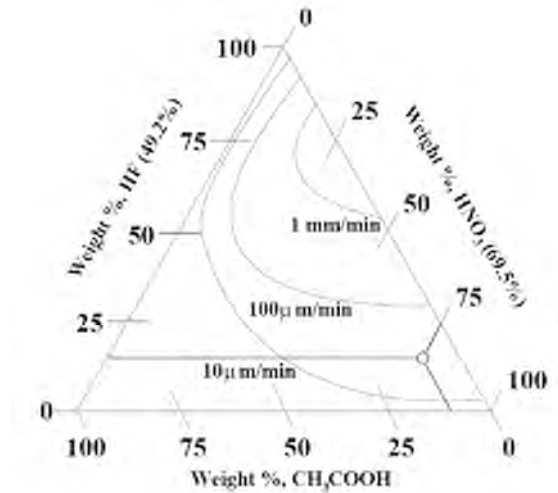


Figure 4.21: Diagram of HNA etching rate (from [127]). The circle corresponds to the concentration of the employed solution.

Using the profiling apparatus described above (section (4.3.1)) the etch velocity can be checked experimentally. It results from a series of measurements performed on a fibre 121 mm long (figure (4.22), where the etching rate is plotted versus the reaction time) that the reaction was slower than the value reported by the diagram in figure (4.21). At the beginning, the etching is quite slow, probably due to the fact that the fibre outer skin, far from being composed by pure Si, contains impurities and oxides. After a fast phase, the etching process again slows down, and this can be caused by depletion of the reactants.

In figure (4.23) the profile of a silicon fibre obtained with the profiling apparatus is shown before and after the etch procedure. It can be noticed clearly that the procedure results in an even diameter reduction all along the fibre.

4.5 Experimental characterization of fibres

A complete room temperature fibre characterization is done as follows. A silicon fibre, grown with the described micro-pulling down method,

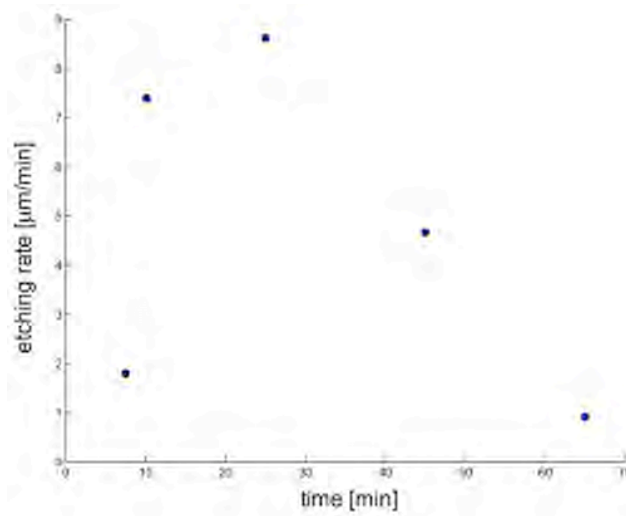


Figure 4.22: Plot of the measured etch rate versus the etching total time, for a 121 mm long, 2 mm thick silicon fibre. The etching solution was 75% HNO_3 , 15% HF and 10% CH_3COOH .

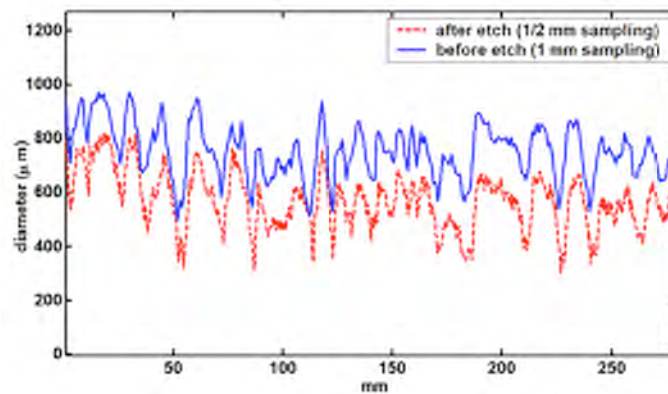


Figure 4.23: Profile of a fibre at a particular angle before (solid blue line) and after (dashed red line) an etching. The diameter has reduced isotropically of about $200 \mu\text{m}$.

is prepared for loss angle measurement. Isopropilic alcohol is employed for cleaning the sample, both for avoiding spurious losses introduced by pollution and for preserving the vacuum from degassing substances.

The fibre head is filed on the side in order to obtain two flat, parallel surfaces. In this way, when the fibre head is clamped, the contact zone is wider allowing a tighter clamping and reducing the risk of breaking it.

In clamping the fibre, the total force acted by the clamp must be kept under the breaking point of the fibre head, which is widely depending on size and imperfections but generally is of the order of 50 kg. This force is exerted on the clamp by a calibrated press, then the clamp is fixed by screws. Often the clamping operation results unsatisfactory, and spurious losses appears. In these cases, the whole measurement procedure must be restarted. The matter is discussed with special attention to the foreseen low temperature measurements in section (4.6).

Once the fibre is clamped, the clamp is settled on the profiling stand and a complete profile is acquired. A 3D model of the fibre is built and a FEA analysis is carried. The analysis provides the set of modal frequencies for the sample, together with the energies and the modes shapes.

Then, the clamp is placed on the measurement stand inside the vacuum chamber. The pumping system is activated and, once a pressure of 10^{-5} mbar is reached, the loss angle measurements can start. The Q of each mode is obtained, then the loss angle $\phi = 1/Q$ is evaluated for each resonance frequency.

After this measurements series, the fibre is removed from the clamp and it is subjected to the etching process, then a new measurements series is carried.

4.5.1 Loss angle measurements

The loss angle has been measured for two fibres with length 308 mm and 111.5 mm.

The measured values for the 308 mm long fibre are shown in figure (4.24). The fibre average diameter was $746 \mu\text{m}$. As it will be explained in section (4.5.2), from the analysis of these data the values of Young's modulus Y , of the thermal expansion coefficient α and of the thermal conductivity κ can be evaluated. Using the measured value of Y , the dispersion relation allows to define an effective diameter for each resonance frequency. Assuming a cylindrical-shaped fibre with this di-

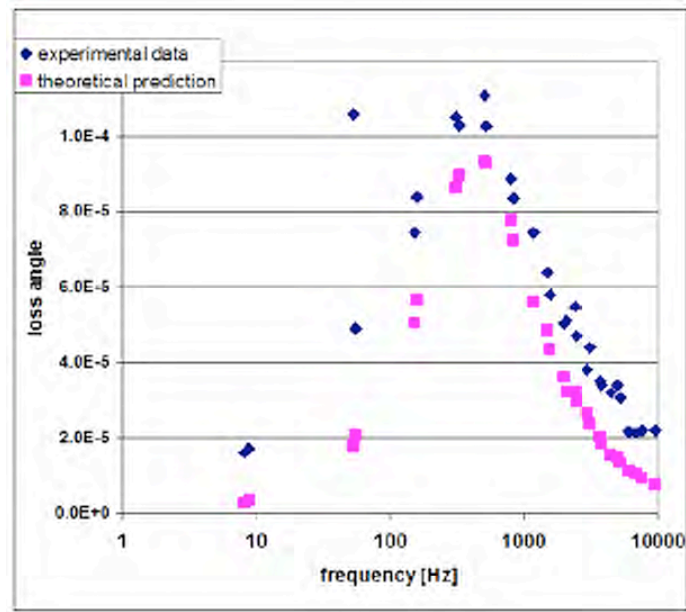


Figure 4.24: Measured loss angle for a 308 mm long fibre, with an average diameter of $746 \mu\text{m}$. The squares represent the thermoelastic contribution as predicted by the finite element analysis model described in the text.

iameter it is possible to predict a value of the thermoelastic loss angle for each resonance, using the formula (2.50). These predictions are also shown on figure (4.24). Their errors come mainly from the uncertainty in the diameter measurement. It is quite evident that some excess loss is present.

In figure (4.25) the measured values of the loss angle for the same fibre after the etching process described in section (4.4) are shown. The average diameter after the etch became $574 \mu\text{m}$; the diameter reduction shifts the position of the thermoelastic peak to higher frequencies. Again, the predictions of thermoelastic losses obtained as explained above are also shown. Clearly, the excess losses play no significant role anymore, thus confirming the idea that surface contaminations were degrading the Q of the sample. Note that a small excess is still present at low frequencies; this is supposed to be due to spurious clamp losses. At low frequency indeed the vibration amplitude is larger, thus all the dissipations induced by the clamp are enhanced.

In figure (4.26) the measured values of ϕ for another fibre 111.5 mm long, treated with chemical etch, are shown. The average diameter of the fibre was $242 \mu\text{m}$. Since this fibre has been found to have a roughly

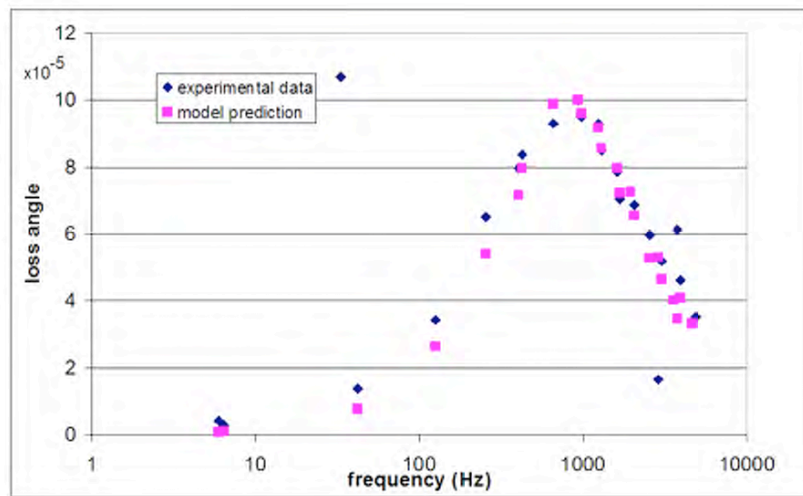


Figure 4.25: Measured loss angle for the same fibre as that shown in figure 4.24 after the etch process; the average diameter is here $574 \mu\text{m}$.

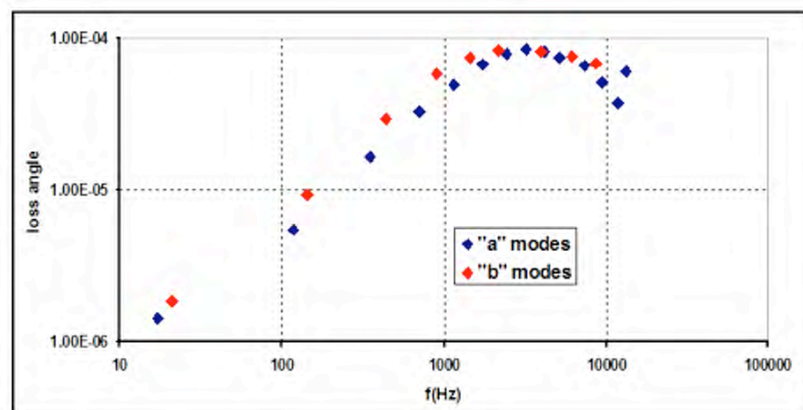


Figure 4.26: Measured loss angle for a 111.5 mm long fibre. The blue and red squares represent the measured loss angle values relative to *a* and *b* modes respectively.

elliptical section, it is evident that the frequencies result to be separated in two sets. Recall indeed the expression (4.8) of the fibre modal frequencies; in case of elliptical section, each mode is split in a doublet, roughly corresponding to the frequencies of two cylindrical fibres with diameters equal to the two main axes of the ellipsis a and b ; that is why in figure (4.26) the two sets are indicated as a -modes and b -modes.

4.5.2 Parameters extraction

The following analysis done for extracting the material thermo-mechanical properties of the silicon fibres resides on FEA carried on the fibres 3D models.

Young's modulus

From equation (4.8), defining $k_i = \alpha_i/L$, it results clearly that, for a cylindrical fibre, f_i/k_i^2 must be constant in frequency. The ratio f_i/k_i^2 experimentally obtained for the 111.5 mm fibre is shown in figure (4.27). The data indicated by blue squares follows two different trends reflecting the ellipticity of the fibre section; moreover, the ratio is not constant due to the irregular geometry of the fibre.

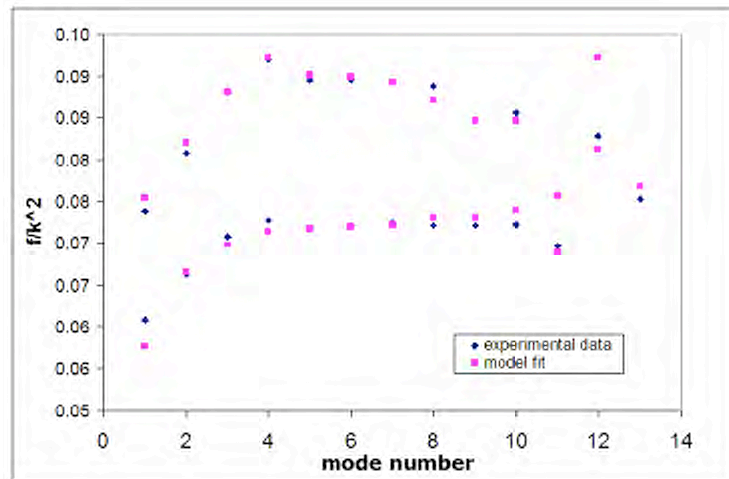


Figure 4.27: Plot of f_i/k_i^2 versus the mode number for the 111.5 mm long fibre.

As seen in section (4.1.2), the silicon fibres have a good crystalline character, but the crystal orientation changes along the fibre axis. Nevertheless, for resonance modes whose wavelength is greater than the typi-

cal monocrystalline scale of the samples (of the order of mm), the elastic deformation sees an effective average Young's modulus Y . Since the FEA model takes into account the geometry of the fibre, it is possible to predict the values of f_i/k_i^2 for a given effective value Y , and therefore the best Young's modulus estimation Y_{best} is obtained by finding a set of frequencies f_i^{model} that minimizes the quantity:

$$\sum_i \left(\frac{f_i^{model} - f_i^{exp}}{k_i^2} \right)^2 \quad (4.23)$$

In figure (4.27) the values predicted by the FEA using for the Young's modulus the obtained value $Y_{best} = (150 \pm 11) \text{ GPa}^2$ are shown with magenta squares. The agreement with the experimental points is very good.

The FEA also allows several modes to be identified, which are not purely transversal, that is, their plane of oscillation depends on the point along the fibre length. These modes have been excluded in the above experimental analysis, since there is not in this case a simple model of the loss angle behaviour.

An analogous estimation gives for the 308 mm long fibre a value of $(174 \pm 12) \text{ GPa}$ for the Young's modulus. Both the Y values are between what is expected for silicon $\langle 100 \rangle$ and $\langle 110 \rangle$ crystallographic directions.

Linear thermal expansion coefficient

The linear thermal expansion coefficient α is completely determined by the thermoelastic peak amplitude ϕ_0 , once the Young's modulus has been evaluated (see equation (2.51)). The specific heat per unit volume is taken as $c_V = C_C \rho$, using the known specific heat $C_C = 707 \text{ J}/(\text{kg K})$ and density $\rho = 2330 \text{ kg}/\text{m}^3$ of silicon.

The ϕ measurements sample the thermoelastic peak at the resonance frequencies only. The amplitude is obtained using the ϕ trend around the peak, finding for the 308 mm fibre $\phi_0 = (10.12 \pm 0.12) \times 10^{-5}$. The error on the amplitude is estimated as the interval between the maximum possible value, taken as the intersection between two lines containing the two couples of experimental points around the peak, and the minimum value which corresponds to the maximum measured ϕ (see

²The error comes mainly from the uncertainty in the diameter measured with the profiling system.

figure (4.28)). Therefore, assuming for T the measured value of 293 K, $\alpha = (2.56 \pm 0.11) \times 10^{-6} \text{ K}^{-1}$.

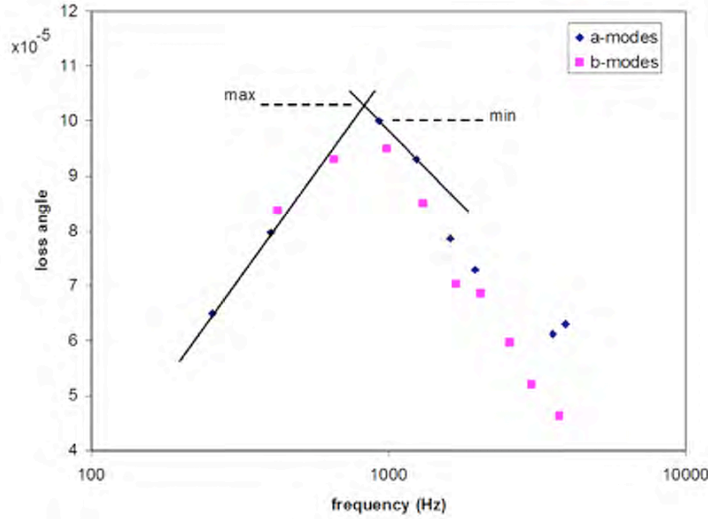


Figure 4.28: Loss angle measurements of the 308 mm fibre around the thermoelastic peak allow the peak amplitude to be estimated and its maximum and minimum values to be determined. The finite element analysis has made possible to recognize also for this fibre *a* and *b* modes, whose splitting is due to the geometrical irregularity of the section.

Analogously, for the 111.5 mm long fibre we found $\phi_0 = (17.26 \pm 0.24) \times 10^{-5}$, and $\alpha = (2.54 \pm 0.13) \times 10^{-6} \text{ K}^{-1}$.

Thermal conduction coefficient

The τ_{th} parameter in the thermoelastic curve allows a determination of the thermal conductivity of the fibre. From equation (2.49), the heat flux characteristic time is:

$$\tau_{th} = C d^2 \frac{c_V}{\kappa} \quad (4.24)$$

Recall that C is a geometrical constant keeping into account the shape of the fiber section. For the 111.5 mm long fibre, whose section is roughly elliptical, an estimate of the distance d can be deduced for each mode assuming a cylindrically shaped fibre oscillating at that frequency. In this way the elliptical section is approximated with two circular sections, one with the larger axis as diameter and the other with the dimensions of the shorter axis, for the two main oscillating direction. Nevertheless, the larger curvature radius assumed for the external circular section leads to

underestimating the heat gradient and, consequently, to overestimating τ_{th} ; the opposite happens assuming the internal circular section. A better first-order estimation can be obtained modifying equation (4.24) with the introduction of a parameter c correcting the form factor C known for a cylindrical geometry:

$$\tau_{th} = \frac{1}{2.16} (1 \pm c) d^2 \frac{c_V}{\kappa} \quad (4.25)$$

The sign $+$ (or $-$) in front of c is referred to the inscribed (respectively, circumscribed) circular section. Fitting τ_{th} for the 111.5 mm long fibre leads to the estimation of the parameters $\kappa = (146 \pm 13)$ W/(mK) and $c = (0.018 \pm 0.002)$, while for the 308 mm fibre $\kappa = (138 \pm 11)$ W/(mK) and $c = (0.001 \pm 0.001)$. The errors are computed varying Y and α within their errors. Table (4.1) summarizes the physical parameters obtained for the two fibres. The thermal conductivity κ is in both cases compatible with the tabulated room temperature value for the silicon. Moreover, the value of c for the 308 mm fibre is compatible with zero, reflecting the fact that this fibre has an almost circular cross section.

$L[\text{mm}]$	$Y[\text{GPa}]$	$\alpha[\text{K}^{-1}]10^{-6}$	$\kappa[\text{W}/(\text{mK})]$	c
111.5 ± 0.5	150 ± 11	2.54 ± 0.13	146 ± 13	0.018 ± 0.002
308.0 ± 0.5	174 ± 12	2.56 ± 0.11	138 ± 11	0.001 ± 0.001

Table 4.1: Summary of the measured physical parameters for the two silicon fibres.

4.6 Investigation on clamps performances

The experience gained in fibres ϕ measurements at room temperature clearly showed the prominent role played by the clamp system in determining the reproducibility and quality of measurements. Regarding the influence of the clamp procedure on the experimental activity on fibres, several point can be highlighted.

Clamping by hand-tightened screws is difficult; very small movements of the screw-driver can suddenly damage or break the fibre, even when the fibre head has been filed. On the other hand, a too soft tightening can not always prevent the appearance of excess losses due to friction or similar phenomena.

Moreover, the clamp material influence on the performances has not been understood, remaining at the level of conjectures. While a soft

material like aluminium should be able to encompass the fibre head, preventing its movements inside the clamp and therefore its friction losses, an aluminium clamp would give rise to plasticity losses in those regions where the pressure is high. The matter is further complicated by the fact that thin fibres can locally penetrate deeper in the clamp than the thick ones.

The clamping procedure can be made more independent from force uncertainty using a specifically designed tool. In figure (4.29) a clamp design is presented, which would allow the squeezing force to be finely tuned. In this design, screws are replaced by rigid shafts worked in a single block with the clamp basis. The slab is equipped with two thin rings embossed inside the shaft holes, whose inner radius match the radius of the shaft. Two screws allow these rings to be tightened around the support shafts, acting as jaws. The squeezing pressure on the slab is exerted by means of pipes pressed against these rings (as shown by arrows in figure (4.29)). The clamping force can be adjusted to a chosen value, then the jaws are tightened and the force actuator removed. In the following we will always refer to this generic clamp design.

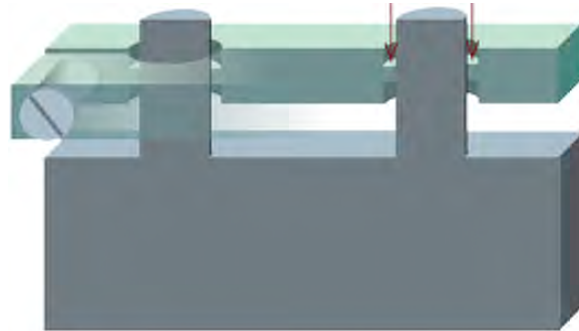


Figure 4.29: Cross sectional view of the clamp designed for optimizing the fibre clamping procedure.

A clamp like the one in figure (4.29) represents a good improvement at room temperature, but it is still unsatisfactory in the case of cryogenic measurements like those we are interested in for next future developments. With the cooling process indeed the whole clamp undergoes thermal contraction, but since the fibre has a thermal expansion coefficient smaller than that of the clamp ($\alpha_{Si} = 2.6 \times 10^{-6} K^{-1}$, $\alpha_{Al} = 2.3 \times 10^{-5} K^{-1}$ at room temperature), going down in temperature results in a squeezing of the fibre head, leading eventually to its breaking.

Basically two clamp designs have been conceived for allowing cryogenic measurements.

Using materials with different thermal expansion coefficients, it is possible to compensate for the thermal expansion of the clamp. The distance between the inner clamp faces must follow the fibre thickness variations with temperature. This idea is explained in paragraph (4.6.2).

Alternatively, the problem could be overcome by using a thin clamp slab. When the cooling shrinks the clamp, the shafts drag the slab against the fibre; hence the slab slightly bends. If the elastic response due to bending is soft (that is the case for a thin plate), it can prevent the fibre from breaking.

4.6.1 Dimensioning the bending clamp

Let us suppose that, while the fibre is vibrating, the fibre head is in frictionless contact with the flat inner sides. Since the fibre outside the clamp is completely free to move (once the gravity is neglected), the vibration modes are those of a rod fixed at one end. Let us call z the coordinate along the fibre and put $z = 0$ at the fixed tip. In order to keep the constrain, a certain force and momentum should be applied from the clamp at $z = 0$. These force and momentum for a cylindrical fibre with length L_f and diameter d_f are [128]:

$$F \propto \sqrt{\frac{KL_f^3}{Ed^4\alpha_i^4}} H(\alpha_i) Ed_f^4 \frac{\alpha_i^3}{L_f^3} \quad (4.26)$$

$$M_x \propto \sqrt{\frac{KL_f^3}{Ed^4\alpha_i^4}} Ed_f^4 \frac{\alpha_i^2}{L_f^2} \quad (4.27)$$

where E is the Young's modulus inside the fibre, K is the energy stored in the oscillation, $H(\alpha)$ is an adimensional function³ and α_i is found to be for the i -th mode ($i > 2$):

$$\alpha_i = \frac{\pi}{2} + (i - 1)\pi \quad (i > 2)$$

³The function $H(\alpha)$ comes from the solution of the force and momentum equations under suitable constraints for the clamped end. It results:

$$H(\alpha) = \frac{\sin(\alpha) - \sinh(\alpha)}{\cos(\alpha) + \cosh(\alpha)}, \quad \alpha = kL$$

where k is the wave number and L is the free length of the fibre.

Since, from the third mode on, $H(\alpha_i) \simeq -1$, taking as reference the value of α_i for $i=4$ and including all numerical constants disregarded in (4.26), (4.27) yields:

$$F = 3.2 \times 10^{-3} \left(\frac{d_f}{1 \text{ mm}} \right)^2 \left(\frac{L_f}{20 \text{ cm}} \right)^{-3/2} \times \\ \times \sqrt{\frac{E}{1.7 \times 10^{11} \text{ Pa}}} \sqrt{\frac{K}{10^{-6} \text{ J}}} \left(\frac{\alpha_i}{11} \right) \quad \text{N} \quad (4.28)$$

This value for the force acting against the clamp increases for increasing mode number i .

Consider now the behavior of the clamp upper slab, tightened with the two shaft-pressing jaws as described in paragraph (4.6) and pushed by the fibre head with a pulsating force of amplitude F . Let assume this force to be applied uniformly along the medium line of the slab (that is a rough approximation, the force being applied by the fibre mainly at the clamp brim). If the fibre is assumed to be placed midway between the shafts⁴, the amplitude of the bending ζ of the slab pushed by the fibre turns to be (see [128]):

$$\zeta \left(\frac{l}{2} \right) = \frac{Fl^3}{192 Y I}$$

Y being the Young's modulus of the clamp, l the distance between the shafts and I the cross sectional moment of inertia, which for a rectangular section of width L and thickness d is:

$$I = \frac{L d^3}{12}$$

Thus ζ and F obey to an usual elastic equation $F = k \zeta$, once it has been defined an effective elastic constant k as:

$$k = 16 Y L \frac{d^3}{l^3} \quad (4.29)$$

Because of this shaking, part of the elastic vibration energy is stored in the oscillation of the slab. It is possible, using the written relations, to evaluate how much energy is transferred to the clamp, allowing an

⁴The reported expression is valid for a slab with both ends clamped, as it is the case for the rigidly fixed clamp plate. If the slab is instead supported, the right side of the equation should be multiplied by 4.

estimation of the dissipation inside it. At that point the loss angle associated with such dissipation will be requested to be less than a chosen value (in the present case 10^{-8}), so that it will be negligible compared with the loss angle of the fibre: this request will result in an evaluation of a minimal value for the thickness d . It should be noted that the described analysis is quasi-static, taking into account only the amplitude of the force exerted, and is useful for the sake of the slab dimensioning; a dynamical calculation should pass through the transfer function of the whole system. A quasi-static analysis would be strictly valid only well below the first resonance of the slab (about several kHz).

The first step is to write down the energy of the oscillating slab as:

$$\epsilon_s = \frac{k\zeta^2}{2} = \frac{F^2}{2k} \quad (4.30)$$

Here F contains a dependence on the energy K , while the thickness d is "hidden" in k .

The amount of dissipated energy in the clamp is easily obtained when the loss angle ϕ_s of the material the slab is made of is known:

$$\epsilon_{diss} = 2\pi\phi_s\epsilon_s$$

From the point of view of the whole energy K , there will exist an effective value ϕ_c such that:

$$\epsilon_{diss} = 2\pi\phi_c K$$

Therefore the loss angle associated with the slab motion is:

$$\phi_c = \phi_s \frac{\epsilon_s}{K}$$

Substituting now the expression (4.30) yields:

$$\phi_c = \phi_s \frac{F^2}{2kK}$$

In the latter equation k can be written explicitly in terms of d ; the force F can also be put in the form (4.28), so that forcing $\phi_c \leq 10^{-8}$ leads to a condition on d for the i -th mode:

$$d_i \geq \sqrt[3]{\frac{\phi_s}{2K10^{-8}} \frac{F^2(\alpha_i)l^3}{16YL}} \quad (4.31)$$

Assuming a conservative estimation for the clamp material losses ($\phi_s = 10^{-2}$), and requiring this condition to be valid up to the 10^{th} mode, we have finally $d_{min} \simeq 2$ mm (stainless steel clamp). Numerical values of

geometrical and elastic parameters used in this computation are reported in table (4.2). It is worth noting that F is proportional to \sqrt{K} , so that in (4.31) the result does not depend on K .

Y	L	l	E	L_f	d_f
210 GPa	2 cm	1.6 cm	170 GPa	18 cm	2400 μm

Table 4.2: Numerical values used for the computation of the minimal clamp plate thickness.

So far, it has been explored the lower limit for d , keeping the other clamp dimensions fixed. It could seem now that a clamp with $d \gtrsim d_{min}$ would be a suitable solution, but since things go better when d increases, why not choosing d as large as possible?

With a large d , problems arise when Q measurement are performed at low temperatures. Thermal expansion is indeed very different in silicon fibres and in the clamp material (see paragraph (4.6)), smaller for the former than for the latter. Thus going down in temperature results in an additional squeezing force exerted by the clamp on the fibre. If d is "large" (in a sense that will be shortly made more quantitative) this additional squeezing would be strong enough to break the fibre.

Therefore the question becomes: how large can be d in order to prevent a breaking inside the clamp? It depends obviously on the force F_0 applied by the clamp before the cooling. Suppose C to be the breaking value of the force for a clamped fibre; it is clear that having $F_0 \ll C$ will let d to be very high, but in that case the friction losses inside such a weak clamp would be severe. This is the reason why the clamp is tightened with F_0 a considerable fraction of C . The experience suggests that, for silicon fibres with diameter $d_f \sim 1$ mm, the breaking force is $C \gtrsim 500$ N.

With $F_0 \sim C$ it is clear that the cool-induced breaking becomes very likely; so the clamp should be as soft as possible ($d \sim d_{min}$). In the following, the presented approach for the calculation of d_{min} is pursued in a slightly different perspective for showing clearly the effect of the cooling.

Let the force F_0 to be about 500 N, and suppose the room temperature bending of the clamp slab is $\zeta \sim 1$ μm . Since the fibre is very close to the breaking, it is necessary to take care about the cool-induced bending. If the temperature T goes from 300 K to 100 K, for a diameter $d_f = 1$ mm

the bending increases by about $3.5 \mu\text{m}$, so willing to keep the additional squeezing force due to the cooling at a level of, for instance, 35% of F_0 (a conservative value), it should be $\zeta = 10 \mu\text{m}$. It is straightforward to obtain the elastic constant for the room temperature bending:

$$k = \frac{F_0}{\zeta} = 5 \cdot 10^7 \frac{N}{m}$$

thus, remembering the equation (4.29), the thickness d can be worked out as:

$$d = l \sqrt[3]{\frac{k}{16 Y L}}$$

that is, for values in table (4.2):

$$d \simeq 3.6 \text{ mm}$$

Therefore choosing a value for the bending, suitable for preventing the breaking, the thickness comes out of the same order of magnitude than in the evaluation obtained formerly in this section.

Does this value verify the constraint put on the loss angle ϕ_c ? The energy stored in the clamp for the 4th mode of the fibre is:

$$E_c = \frac{F^2}{2k} = 2 \cdot 10^{-13} \text{ J}$$

where F is the oscillating force of equation (4.28) for $K = 1 \mu\text{J}$. For the loss angle it leads to:

$$\phi_c = \phi_s \frac{E_c}{K} = 10^{-9}$$

and the request is fulfilled.

The chosen values for the geometrical dimensions of the realized clamp are reported in table (4.3). A scheme of this clamp is shown in figure (4.30).

L	l	d
2 cm	1.6 cm	2.4 mm

Table 4.3: Geometrical dimensions of the stainless steel clamp sized using the computation described in the text.

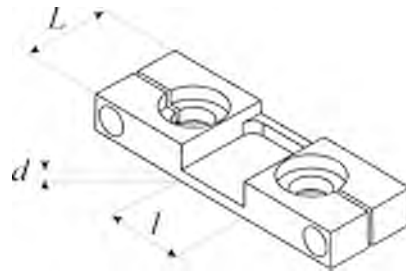


Figure 4.30: Design of the bending clamp slab to be mounted on the shaft-pressing jaws described in paragraph 4.6. Dimensions are those reported in table 4.3.

4.6.2 A clamp based on thermal compensation

Thermal expansion of different materials can be advantageously used for the sake of counteracting the fibre squeezing induced by cooling. This idea relies on the fact that, once a squeezing force is chosen, its effect can be thought as a shortening of the distance between the two clamping surfaces, and, due to the low value of thermal expansion in silicon, maintaining the squeezing force constant is (almost) the same as maintaining constant such distance. It can be done by realizing the slab of the clamp with a material having a suitable expansion coefficient and shaping it in a proper way.

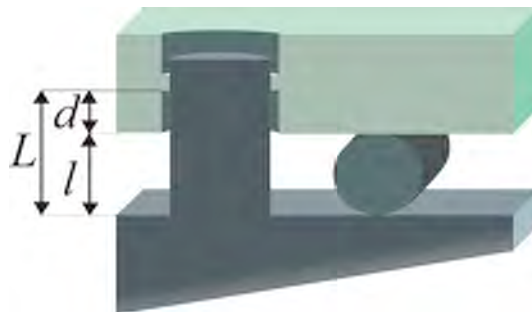


Figure 4.31: Clamp scheme for thermal compensation of cooling-induced squeezing. Note the protruding lower part of the slab, which drops down for a length d from the narrow ring jaw around the clamp shaft.

Refer to figure (4.32). It should be noted the protruding lobe of the clamp slab, whose depth is d . The slab and the support are made with two different materials. Once the fibre has been tightened, before the cooling, we have:

$$L_0 = d_0 + l_0 \quad (4.32)$$

where the subscript 0 denotes quantities taken at room temperature T_0 .

During the cooling inside the cryostat, all these lengths vary according to the thermal expansion law:

$$\frac{\Delta\mathcal{L}(T, \Delta T)}{\mathcal{L}(T)} = \alpha(T)\Delta T \quad (4.33)$$

Since α depends on the temperature, for large ΔT the length variation is the sum of small variations like the ones described by (4.33). This variation is tabulated [129] as a function of the temperature for the various materials, assigning the values of polynomial coefficients. So for instance the thickness of the silicon fibre can be written as:

$$l(T) = l_0 \left(1 + \left[\frac{\Delta\mathcal{L}}{\mathcal{L}} \right]_{Si} (T) \right) \quad (4.34)$$

The expression:

$$\Delta l(T) = l(T) - l_0 = l_0 \left[\frac{\Delta\mathcal{L}}{\mathcal{L}} \right]_{Si} (T) \quad (4.35)$$

represents the thickness variation of the fibre at temperature T .

Now, since we need to keep constant the force against the fibre, and this force is obviously related to the distance between the clamp inner faces, the condition:

$$L(T) - d(T) \sim l(T) \quad (4.36)$$

must be valid at each temperature. Thus we need to compare (4.35) with:

$$(L - d)(T) = L_0 \left(1 + \left[\frac{\Delta\mathcal{L}}{\mathcal{L}} \right]_{SS} (T) \right) - d_0 \left(1 + \left[\frac{\Delta\mathcal{L}}{\mathcal{L}} \right]_X (T) \right) \quad (4.37)$$

where subscripts SS (stainless steel) and X indicate the material which the clamp support and slab are made with. Taking L_0 as parameter, and remembering (4.32), equation (4.37) leads to:

$$\begin{aligned} (L - d)(T) &= L_0 \left(1 + \left[\frac{\Delta\mathcal{L}}{\mathcal{L}} \right]_{SS} (T) \right) - (L_0 - l_0) \left(1 + \left[\frac{\Delta\mathcal{L}}{\mathcal{L}} \right]_X (T) \right) \\ \Delta(L - d) &= L - d - (L_0 - d_0) \\ &= L_0 \left[\left[\frac{\Delta\mathcal{L}}{\mathcal{L}} \right]_{SS} (T) - \left[\frac{\Delta\mathcal{L}}{\mathcal{L}} \right]_X (T) \right] + l_0 \left[\frac{\Delta\mathcal{L}}{\mathcal{L}} \right]_X (T) \end{aligned} \quad (4.38)$$

For a fibre with given diameter l_0 , appropriately choosing both L_0 and the material X , the condition (4.36) can be satisfied with good approximation. The values $\Delta(L - d)(T)$ for aluminium (triangles) and brass (diamonds) are compared with $\Delta l(T)$ in figure (4.32), where $l_0 = 2.2$ mm and $L_0 = 1.2$ cm.

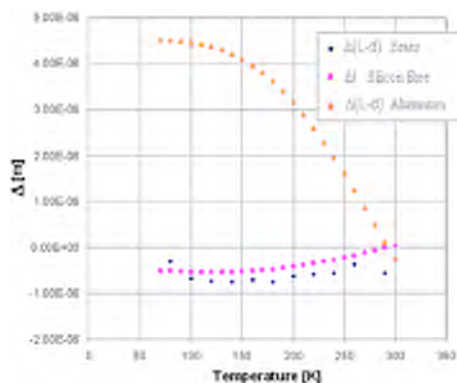


Figure 4.32: Comparison between thermal compensation obtained with brass and with aluminium. The fibre diameter is $l_0 = 2.2$ mm and the shaft length $L_0 = 1.2$ cm.

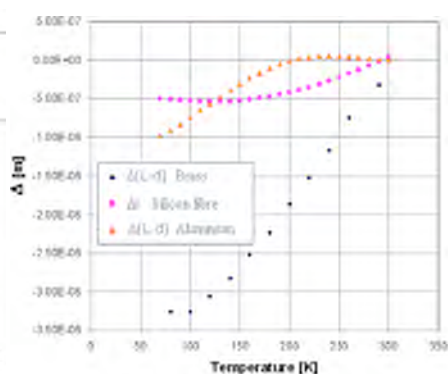


Figure 4.33: Comparison between thermal compensation obtained with brass and with aluminium. The fibre diameter is $l_0 = 2.2$ mm and the shaft length $L_0 = 0.7$ cm.

Obviously, each deviation $\delta(T) = \Delta l(T) - [\Delta(L - d)(T)]$ from the perfect thermal compensation would result in a static force $\Delta F_{th}(T) = k_{slab}\delta(T)$ against the fibre. From the figure it is clear that a suitably shaped brass slab could follow the silicon contraction trend, with a maximum deviation $\delta \simeq .5 \mu\text{m}$. Also, an aluminium slab can be realized, provided that in this case the shaft free length is $L_0 = 7$ mm; the maximum deviation does not exceed $\delta \simeq .5 \mu\text{m}$, but the concavity is not well fitting (see figure (4.33)). Table (4.4) resumes the shaping parameters obtained for aluminium and brass.

material	L_0 (mm)	d_0 (mm)	δ_{MAX} (μm)	$\langle \delta \rangle$ (μm)
BRASS	12	9.8	0.5	0.21
ALUMINIUM	7	4.8	0.5	0.25

Table 4.4: Shaping parameters for thermal compensating clamps, with a fibre diameter $l_0 = 2.2$.

4.7 Conclusions

We used crystalline silicon fibres produced with the micro-pulling down technique for testing experimentally several items. First of all, a custom production of fibres with optimal crystalline characteristics, with the possibility of shaping and doping, is possible thanks to a dedicated facility.

This will be fundamental when a full analysis of the doping influence (as an example, on the anti-Stokes cooling) will be carried out. Moreover, measurements of the loss angle indicated clearly that the influence of surface defects produced as a by-product of the pulling technique can be eliminated using an isotropic etching. The etching is also useful for a re-shaping of the silicon fibres, since it can be precisely controlled. It is remarkable the fact that, to our experience, the excess surface loss is still not present in the etched fibres, even after several weeks. Handling and exposition to air did not spoil the fibres high Q values. Our work on the experimental results shows that a finite element analysis can be very helpful in extracting the fibres thermomechanical parameters only by knowing the thermoelastic loss.

The activity on this topic is just at the beginning. Monolithic suspensions using silicon fibres have never been realized; the suspensions design is still under consideration. A main problem evidenced during our measurements is that the welding of silicon fibres on silicon ears cannot be performed with the method used for silica: the high conductivity of silicon prevents the heat from melting the material in a localized volume.

In this preliminary phase, the natural continuation of our work is a cryogenic measurement of the fibres dissipation; part of this activity has been pursued at the INFN laboratories in Perugia [122], while we foresee to test our ideas on fibre clamping at cryogenic temperatures.

Chapter 5

Thermal conductivity measurements

As discussed in chapter (4), silicon monolithic suspensions are thought to be very advantageous in the perspective of cryogenic third generation ground-based GW detectors. A thermomechanical characterization of silicon specimens is therefore necessary. In this chapter a facility for measuring the thermal conductivity of various materials samples is presented. The facility is now working and it is disposable for the European GW community involved in the design study of a third generation interferometer.

In the first section, the question why it is convenient to measure directly the thermal conductivity of specimens, instead of taking literature data, is addressed. A description of the main features of heat conduction in semiconductors like silicon is shortly given.

Then, the realization of the apparatus for thermal conductivity measurements down to cryogenic temperatures is discussed, and a test measurement made on a high purity silicon reed is presented.

Once the system has been tested, it has been employed for studying the thermal conduction across silicate bonded silicon disks. Silicate bonding, a technique developed for chemically gluing silica substrates, is briefly reviewed; this technique will be employed for assembling monolithic silicon suspensions. The modifications of the apparatus made for measuring the bonded disks conductivity are commented, and measurement results are shown. Remarks on next work to be done within the item of silicon silicate bonding conductivity are given.

Finally, the design of a facility to be used for measuring the thermal expansion coefficient and small displacements in general is presented.

Small displacements include a series of phenomena, like creep and thermal expansion, which are of high interest in the field of suspensions noise issues. Part of the facility has been also realized, as it is described in the last section.

5.1 Thermal conductivity of silicon

The design of the suspensions for the third generation of GW interferometers must take into account the problem of heat extraction, as discussed in section (4.1). Obviously, in this respect, the main issue is represented by the thermal conductivity of the suspensions. The heat extraction capability depends upon the thermal conductance $K(T)$ of the suspension fibres¹:

$$K(T) = \kappa(T) \frac{n\Sigma}{L} \quad (5.1)$$

where Σ is the cross section of the fibres, L is their length, n is the number of fibres, $\kappa(T)$ is the thermal conductivity coefficient and the Σ , L temperature dependence has been neglected. The heat flux equation:

$$C\dot{\theta}_R(t) + k\theta_R(t) = P(t) \quad (5.2)$$

where θ_R is the temperature difference among the fibre ends due to the flux P and C is the heat capacity, can be written in the regime condition when $P(t) = P_0$ as:

$$\theta_R = \frac{P_0}{K} \quad (5.3)$$

In section (4.1) the advantages of choosing silicon suspensions have been explained; the expected behaviour of the silicon thermal conductivity was also described. Suitable silicon monolithic suspensions should have $\Sigma \sim 100 \text{ mm}^2$ and $\theta_R \sim 2 \text{ K}$ [102].

As it is well known, at low temperatures (below 100 K) the thermal conductivity can vary largely, even for materials specimens of the same shape and conditions, depending on samples history and purity [130]. This is especially true for silicon [131], [132], [133], [134], [135], [136]. As for other semiconductors, the heat conduction in silicon is mainly due to phonons currents. Considering thus a phonons gas carrying the heat along the thermal gradient, the conductivity results:

$$\kappa = \frac{1}{3} C v \lambda_p \quad (5.4)$$

¹The following equation is valid for homogeneous bodies with constant cross section.

where C is the specific heat capacity, v is a mean velocity of the phononic flux and λ_p is the phonons mean free path.

In figure (5.1) a typical $\kappa(T)$ curve for crystalline silicon is presented, showing a broad peak well below room temperature. Indeed, when temperature starts to go down phonon *Umklapp* scattering depending on silicon Debye temperature becomes less frequent, so that λ_p grows causing κ to increase. This trend is counteracted when defects or impurities in the crystal become "visible" for phonons, so that diffusion happens. Thus, a maximum value is reached; pushing T further down, the phonon mean free path gets larger until it becomes comparable with the sample dimensions D . From this point down, one has to put $\lambda_p = D$ in equation (5.4), obtaining, since v is almost independent of T , that $\kappa(T \rightarrow 0 \text{ K}) \propto C \propto T^3$. Therefore, κ starts to decrease rapidly toward zero.

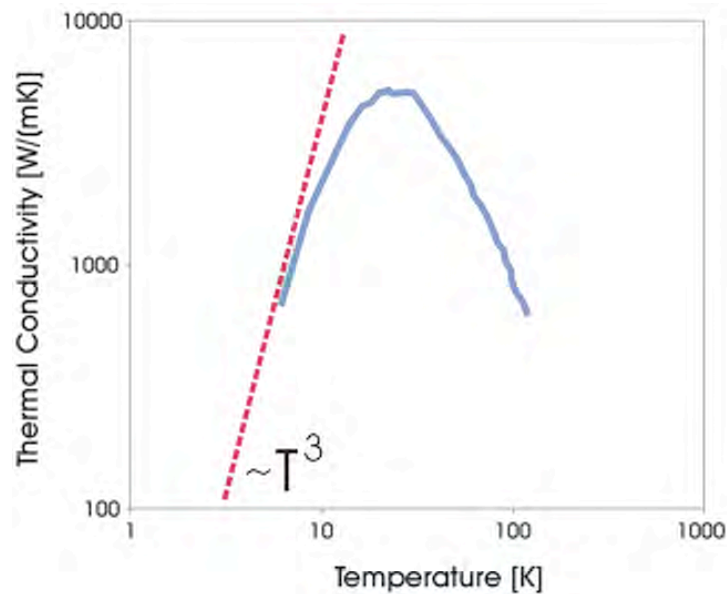


Figure 5.1: A typical curve for silicon thermal conductivity (from [137]). The proportionality to T^3 at low temperatures is fitted by the red dotted line.

Diffusion by defects due to both handling and impurities (even if at a very low level) determines the κ peak region, while specimen dimensions set the region where the $\kappa \propto T^3$ regime is valid. For temperatures $T \gtrsim 100 \text{ K}$ or $T \rightarrow 0 \text{ K}$, almost all crystalline silicon samples with similar dimensions behave in the same way².

²This is not the case for isotopically pure silicon, which shows an higher conductivity with respect to the natural one, even at room temperature [133].

The behaviour of $\kappa(T)$ thus carries information about the physical status of phonons in the crystal. As discussed in section (2.4.2), attenuation of sonic and ultrasonic waves in a perfect semiconducting crystal is mainly due to phonon-phonon interactions. Moreover, in the peak region of $\kappa(T)$ the role of defects and impurities is fundamental, and it can be correlated to the energy dissipation which, in a real crystal, arise from processes involving indeed impurities and crystallographic defects (see section (2.4.2)).

The thermomechanical characterization of silicon suspensions and the study of thermal issues in related techniques requires therefore the thermal conductivity to be measured for the materials and the components the suspensions will be made of.

5.2 A thermal conductivity measurement facility

A facility has been realized for measuring the thermal conductivity coefficient in interesting specimens, at temperatures ranging from room value down to cryogenic values. The facility is conceived for steady state measurements of the thermal gradient set across a constant cross section sample by a given constant heat flux. Once the temperature gradient is measured along the flux, knowing just the power flowing through the sample and the geometric parameters Σ and L , the thermal conductivity κ is obtained by means of equations (5.1) and (5.3).

In practice, an homogeneous heat flux P_0 from an heater flows in the sample. The sample, whose cross section is Σ , is connected with a massive heat sink, so that a steady flux is reached after few minutes. Along the flux direction, in two points at a distance L from one another, two temperature sensors are placed in contact with the specimen. The temperature difference among the points $\Delta T = T_1 - T_2$ is measured, then the conductivity is estimated as:

$$\kappa(T) = \frac{L}{\Sigma} \frac{P_0}{\Delta T} \quad (5.5)$$

Spurious contribution to the heat transfer are due to conduction through air and radiation toward the environment. If the specimen is placed in vacuum, the conduction by air can be kept at a negligible level. The radiation is reduced by keeping the temperature of the surroundings as close as possible to that of the sample.

5.2.1 Experimental apparatus

The facility is divided in two main parts. A cryostat is used for cooling the sample down to cryogenic temperatures; inside the cryostat a pumping stage provides the vacuum level needed for preventing the heat conduction in air. Enclosed in the cryostat, a measurement stage contains the sample holder, the heater and the temperature sensors. These parts are described in detail in the following paragraphs.

Cryostat and vacuum system

In order to measure the curve $\kappa(T)$ down to low temperatures, the sample is hosted in a LN-LHe cryostat which is supported by a rigid structure which is shown in picture (5.2). The cryostat is made with a steel cylinder split in two parts by a copper massive plate (refer to the scheme in figure (5.3)).



Figure 5.2: Picture of the LN-LHe cryostat used for the thermal conductivity measurements.

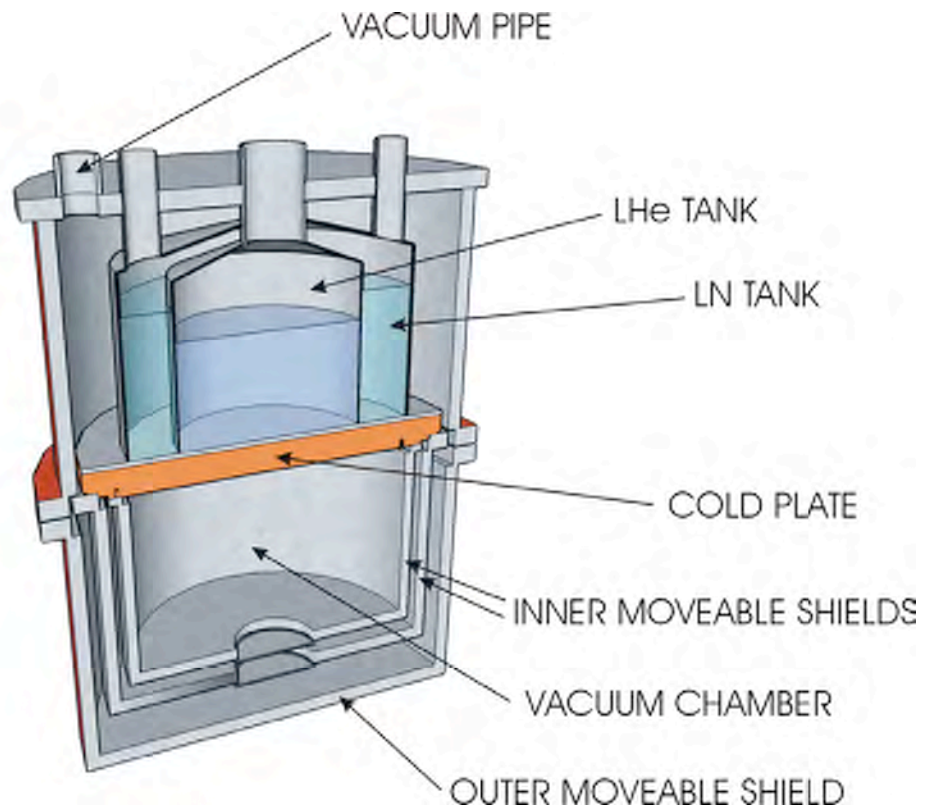


Figure 5.3: Cross sectional view of the LHe-LN cryostat used for measuring the thermal conductivity down to about 4 K. The diameter of the copper cold plate is about 30 cm. The vacuum chamber hosting the experimental equipment is accessible by removing the shields.

In the upper part, two tanks, the one into the other, are placed in contact with the cold copper plate. Refilling holes are opened in the upper steel plate for accessing the tanks. Both tanks can be filled with liquid nitrogen in order to reach 77 K; if then liquid helium is poured in the inner tank in place of nitrogen, 4 K can be attained. The nitrogen can be removed from the inner tank by inserting nitrogen gas in the tank with a two ways pipe as in figure (5.4); then, with a transfer line, the liquid helium is poured from the dewar to the cryostat. This operation must be carried when all the nitrogen from the inner tank has been removed; if a mixing between He and N happens, temperatures as low as 4 K are not attainable.

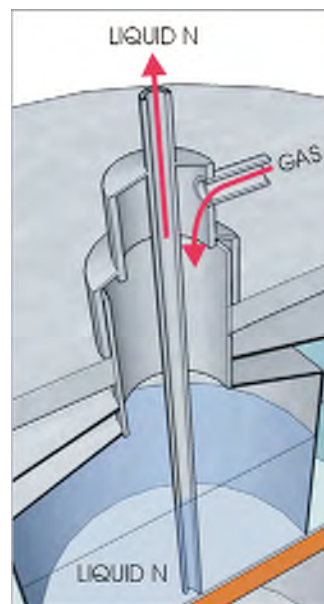


Figure 5.4: Cross sectional view of the cryostat settled with the two way pipe used for depleting the liquid nitrogen from the inner tank.

The cryostat vacuum chamber, which is connected with the pumping stage by a vacuum pipe in the top steel plate, is under the cold plate. The cold plate is accessible by removing three steel shields. The two internal shields are put in direct thermal contact with the plate, preventing excessive radiative heat dispersion from the plate itself to the environment. The shields have optical windows. The cold plate is machined with a pattern of screw holes; it has a diameter of about 30 cm, which represents the available space for hosting experimental equipments. The cryostat is equipped also with a pass-through for electrical connections,

which is not reported in figure.

The pumping stage is realized with two pumps arranged in cascade. A first rotative stage brings the internal pressure down to about $6 \cdot 10^{-2}$ mbar; when this value is reached, a turbo-molecular pump is started, which is directly connected to the cryostat with a wide straight tube. The turbo-molecular pump is able to reach 72000 rpm usually in few minutes, after which the residual pressure is at the level of 10^{-4} mbar. Such pressure is low enough for neglecting air conduction. With this system, the lowest attainable pressure is about 10^{-7} mbar and it is reached within two days. The pressure attains values around 2×10^{-8} mbar when the cryostat is cooled down to 77 K.

Measurement stage

The measurement apparatus is placed underneath the cold plate of the cryostat. The apparatus is composed by three functional parts. A conductive massive clamping system is used for holding the sample, providing at the same time the sinking of the heat flow. The sample is heated by a coil heater placed at the opposite end of the specimen with respect to the sink. Two temperature sensors placed at a precise distance L as large as possible along the flux represent the temperature sensing system. Specifically, the design of each one of these parts depends upon the shape and dimension of the considered sample. To test the apparatus we measured in the chamber a silicon high purity (pure at the level of 1 ppm) cylindrical rod 10 cm long, with a diameter $d = 5$ mm. The setup realized for this specimen is schematically drawn in figure (5.5). It is described here in detail, while the needed modifications for different specimens are discussed later on.

The apparatus is enclosed inside a copper box, which provides an additional thermostatic shielding; its purpose is to get a uniform temperature around the sample in order to reduce at minimum the radiative losses. An aluminium clamp shaped for granting a large contact surface as shown in figure (5.6) is fixed in thermal contact with the copper box. The clamp is big enough for behaving as a thermostat for the power flow needed for the measurement (much less than 1 W); i.e., it operates as heat sink. A PVC layer is interposed between the copper box and the cold plate. That is useful for slowing the cooling of the sample, so that conductivity measurements can be performed at almost every temperature in the range $4 \div 300$ K. In this way, since a single measurement lasts no longer than 15-20 minutes and during that time the temperature of

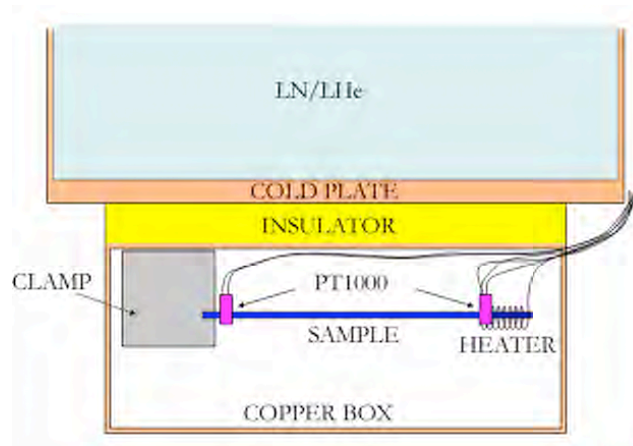


Figure 5.5: Scheme of the apparatus employed for measuring the thermal conductivity of a high purity silicon reed.

the box can be regarded as constant, it is possible to obtain $\kappa(T)$ for each given T .

The sample heater has been realized by means of a constantan wire coiled around the sample end, opposite with respect to the clamp. The wire is connected with the exterior by means of thin cryogenic wires soldered to the cryostat pass-through connectors. The coil provides the heat flux by Joule effect. A dedicated circuitry measures the voltage and the current through the coil allowing the power supplied to the sample to be known.

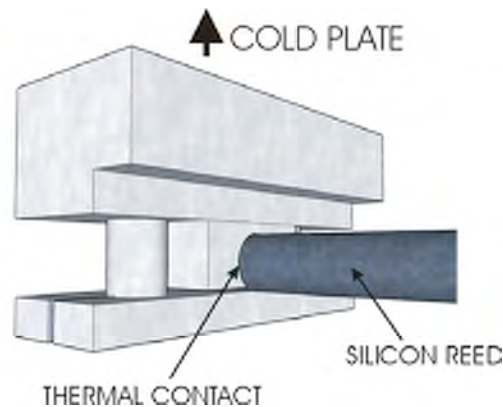


Figure 5.6: Schematic view of the clamping system of the silicon reed, designed for assuring a good thermal contact between the reed and the clamp.

In two distant points along the specimen, PT1000 temperature sen-

sors are put in contact with the silicon rod using two small aluminium clamps. For temperatures below 20 K, Cernox[®] sensors must be employed in place of PT1000. Both sensors are connected to the pass-trough connectors by cryogenic wires. Note that, since the transverse dimension of PT1000 strips is about 2 mm, while the distance among the two sensors is 8 cm, the contact region between the sample and one of the sensors can be regarded as point-like.

Other PT1000 strips are put in the vacuum chamber, in contact with the cold plate and with the aluminium clamp, and out of the cryostat in air. All the connections inside the cryostat are made with cryogenic wires. These sensors register the temperature of the plate T_P , that of the sample T and that of the environment T_E during the measurements.

Circuitry and acquisition line

PT1000 sensors are resistors with a resistance value $R(T)$ sensible to temperature changes (at 300 K, $R=1100\text{ k}\Omega$ and $dR/dT \simeq 4\text{ }\Omega/\text{K}$). A measurement of their resistance is used for measuring T .

For sensors placed on the plate, on the clamp and in air, a precision of the order of a tenth of K is needed. The sensors are mounted in series to a waveform generator providing a sinusoidal signal with $f = 40\text{ Hz}$ and amplitude $V_{RMS} = 1\text{ V}$. The voltage differences V_i at the ends of sensors are acquired by a computer board and sharply filtered around f ; the voltage on a calibrated $1\text{ k}\Omega$ resistance in series to the sensors is also acquired for evaluating the current I . The i -th PT1000 resistance is thus computed as $R_i = V_i/I$. Hence, the values of T_P , T_E and T are obtained by inverting the known relation $R(T)$.

The temperature difference along the sample must instead be measured as precisely as possible. For this reason, the two PT1000 placed on the specimen have been connected in a bridge configuration (refer to figure (5.7)). It results:

$$\Delta V = V \left(\frac{R_1}{R_1 + 50\text{k}\Omega} - \frac{R_2}{R_2 + 50\text{k}\Omega} \right) \quad (5.6)$$

but since $R_i \ll 50\text{k}\Omega$:

$$\Delta V \simeq \frac{V}{50\text{k}\Omega} (R_1 - R_2) = \frac{V}{50\text{k}\Omega} \Delta R \quad (5.7)$$

The bridge is supplied with an AC signal at 60 Hz with RMS amplitude 5 V. The output ΔV is amplified, then a lock-in filter is used for enhancing and demodulating it. The amplification introduces a multiplicative

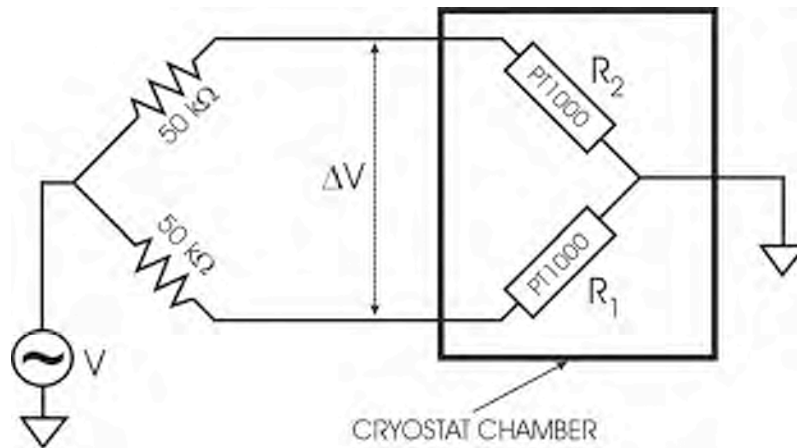


Figure 5.7: Schematic of the circuitry used for measuring the temperature on the sample. The two PT1000 resistors are placed inside the cryostat, in contact with the specimen.

coefficient in equation (5.7), thus the overall factor $c = \Delta R / \Delta V$ must be evaluated. A calibration of the bridge, therefore, is obtained placing a $100 \text{ k}\Omega$ in parallel to a PT1000 and measuring the corresponding output variation. That allows c to be measured at the working point.

Potentiometers (not shown in figure) are placed in both the branches of the bridge, for correcting the unbalancing offset and setting it to zero. This is particularly useful when the sample is cooled, since the offset level varies with the absolute temperature.

Then the calibrated output of the lock-in is acquired and converted in temperature by means of the known relation $R(T)$. The temperature difference ΔT is thus obtained.

5.3 Facility test measurements

Figure (5.8) shows the apparatus fixed beneath the cold plate, and the silicon reed placed in the aluminium clamp.

During the measurement, the heat flux in air is completely negligible due to the low value of the residual pressure. Nevertheless, the power radiated at regime by the sample must be subtracted from the amount of power supplied to the sample; that is, the whole conductivity which is measured contains a spurious contribution due to radiation toward the copper box. This contribution depends on the temperature difference between the silicon reed and the box. Clearly, the effect of radiative

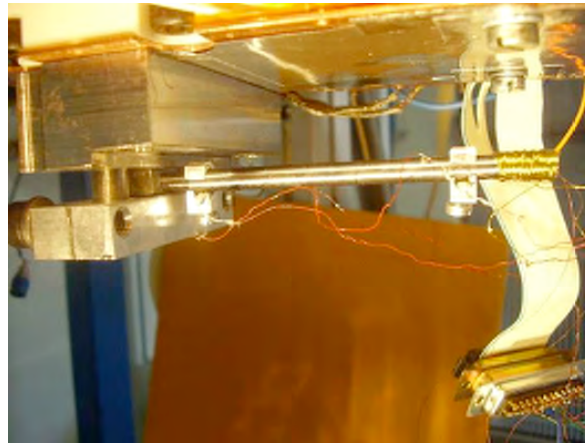


Figure 5.8: Picture of the apparatus used for measuring the thermal conductivity of a silicon reed 10 cm long, 5 mm thick.

conductance must be evaluated.

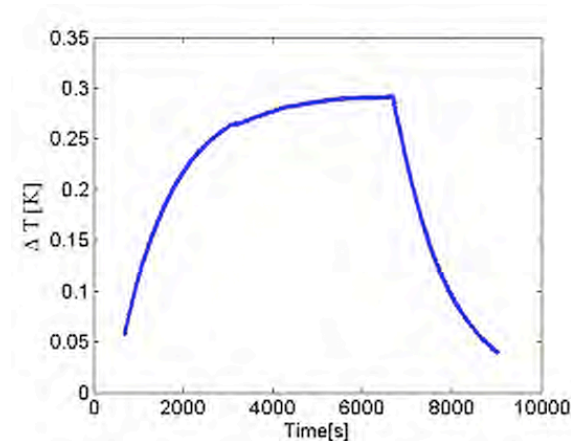


Figure 5.9: Heating curve of the silicon reed suspended with two plastic wires, recorded for evaluating radiation loss.

At room temperature, the silicon sample has been disconnected from the clamp and suspended in vacuum to two thin plastic wires. One of the two bridge PT1000 has been moved to the box surface, and the sample has been heated. By measuring ΔT in this configuration, it has been possible to evaluate the radiating conductance, which has been proved to be negligible³. By fitting the obtained heating curve in figure (5.9), the heat capacity has been also measured (see table (5.1)).

³The radiative loss of heat obviously becomes even lower at low temperatures.

C [J/K]	K [mW/K]
4.2 ± 0.1	3.7 ± 0.1

Table 5.1: Heat capacity and radiating conductance measured for the high purity silicon reed.

A set of measurements of $\kappa(T)$ of the silicon reed has been performed in the way described in the previous section. Since the offset signal of the bridge follows the absolute temperature, each heating curve is superimposed to a slowly varying offset. However, this problem can be easily overcome, by linearly fitting the offset variation and subtracting it by the acquired curve. From the residual heating curve, the temperature difference at regime is evaluated.

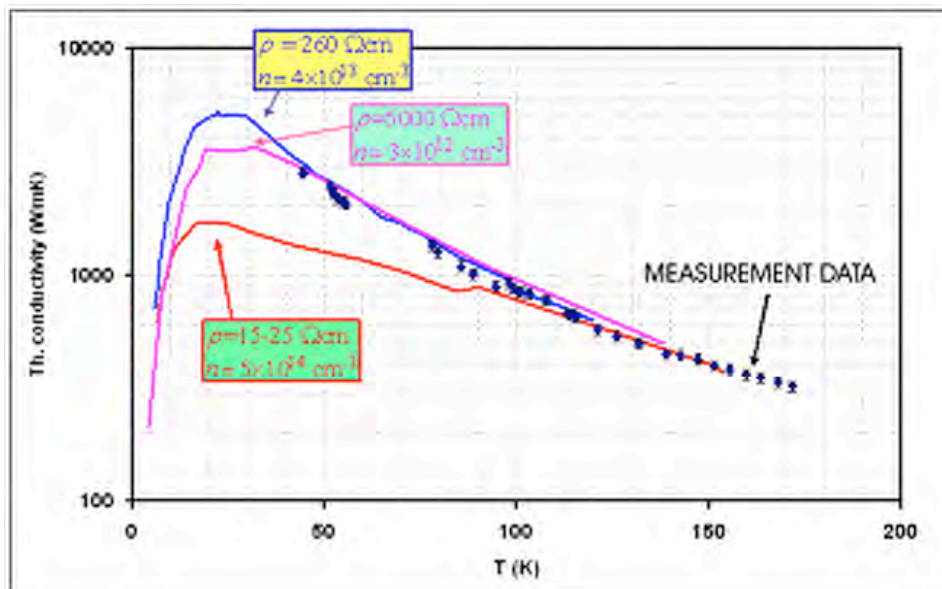


Figure 5.10: The measured values of $\kappa(T)$ for the high purity silicon reed are compared with three curves taken from literature [137]. The comparing curves have been chosen to be obtained with specimens as similar as possible to the measured reed. The measured resistivity of the latter is $42 \Omega\text{cm}$.

Experimental results are sketched in figure (5.10) and compared with literature data. The dominant contribution to the error on $\kappa(T)$ is due to the bad knowledge of the distance L and of the cross sectional radius r needed for computing $\Sigma = \pi r^2$, which have been evaluated with a caliper. Measurement relative error is of the order of 5%. Due to a technical

problem in depleting nitrogen from the inner tank of the cryostat, a little quantity of nitrogen mixed to the liquid helium, thus for this test run it has been impossible to push T below 40 K. This problem has been fixed after the run.

Nevertheless, measurements result to be in rather good agreement with literature data in the temperature region over 100 K, where *Umklapp* scattering makes κ almost independent from purity, shape and handling.

5.4 The silicate bonding technique

Monolithic arrangement discussed in section (3.1) requires the suspension elements (ribbons, fibres) to be attached to the test masses. The technique currently indicated for connecting mirrors and suspensions is the so called *silicate bonding* technique [112], [85].

Silicate bonding is a chemical gluing which has been firstly developed and patented at Stanford University by D.H. Gwo, for the Gravity Probe B experiment [138], [139].

5.4.1 Chemistry of the silicate bonding

Silicate bonding is often referred to as *hydroxide-catalyzed hydration-dehydration process* [140]. Hydroxy-catalysis bonding is typically used for joining oxide materials. The bonding is realized with a strong, rigid, very thin layer of oxide settled among two surfaces with high flatness (that is, flat within $\lambda/10$ where $\lambda = 633$ nm). A drop of aqueous hydroxide solution such as KOH or NaOH is deposited among the surfaces; a silicate gel is formed, that solidifies over time.

The first step in the process is the hydration of the surface of silica. Silicon surfaces must be oxidized, so that a silica layer about 100 nm thick is disposable for the bonding. Since the silica surface is hydrophilic, OH^- ions present in solution match the silica open bonds for forming silanol Si-OH groups (refer to figure (5.11)). The role of KOH or NaOH is to speed up this process, enhancing the basicity of the solution.

An etching of the surface occurs, due to the high concentration of OH^- in solution. Since the OH^- ions create additional bonds with the Si atoms, as a consequence the original lattice bonds weaken; therefore a certain amount of Si atoms are separated from the surface. This etch releases in solution $\text{Si}(\text{OH})_5^-$ and $\text{Si}(\text{OH})_3^{2-}$ silicates.

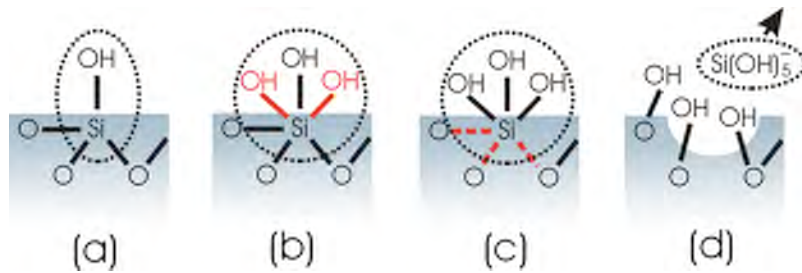


Figure 5.11: Scheme of the steps of hydration and etching of the silica substrate during the silicate bonding process. (a) Hydration of the silica surface. (b) Creation of additional bonds between Si and OH^- ions in solution. (c) Consequent weakening of some bulk Si-O bonds. (d) Silicates are extracted from the surface causing the etching of the substrate.

The OH^- ions also strip the H^+ ions from the silanol groups, forming water. This is the dehydration step. The Si-OH groups dehydration causes the formation of Si-O-Si bridges at the surfaces. Then, silicates chains connect the two surfaces. This occurs because silicates are dissociated in monomers which tend to form chains starting from silanol bridges and connecting the two surfaces. A definite settling time which depends on the initial pH of the solution is necessary for the silica gel layer to become rigid. Usually, settling time is of the order of hundreds of seconds. Then, a curing phase of the bonding follows which lasts for a time of the order of months.

5.4.2 Silicate bonding characteristics

Mechanical characteristics of silicate bonding have been measured in many experiments. The silica to silica bonding layer obtained with the described method is usually about 100 nm thick [141], [142], [143].

Quality factors of mirrors and fused silica masses with silicate bonded silica ears have been evaluated, showing that the bond does not spoil the overall performances [144], [145]. Nonetheless, estimations of intrinsic loss angle of the bonding materials give values around 10^{-1} [141]; this high level of dissipation suggests that the bonding material is substantially different with respect to well-formed glass or silica. The silicate bonding layer can be thought as forming a very imperfect glass with many vacancies, dislocations and incomplete bonds.

Breaking stress of silicate bonded silica masses proved to be high, of the order of MPa [87], [143].

Silicon to silicon bonds are currently under study, they seem to show a very similar behaviour to that of silica to silica ones. One interesting point to note is that electron microscope imaging suggests that bonds can lie in the range of thicknesses $40 \div 100$ nm [146]. Breaking stress is almost independent on crystallographic orientation of silicon, and can be as high as 8 MPa [147].

In a future silicon monolithic suspensions arrangement, heat extraction capability is a main issue. Therefore, the thermal conductance of silicate bonds must be high enough for avoiding spoiling that of silicon at low temperatures. Thermal conduction measurements would allow not only to evaluate the conductive properties and homogeneity of the layer, but also its compactness, by comparing the conductivity obtained for the layer with that of bulky silica.

5.5 Measurement of silicate bonded high purity silicon disks and effects of inhomogeneities

Pairs of 1' in diameter, 6 mm thick silicon disks have been bonded (see figure (5.12)) at the University of Glasgow using different volumes of sodium silicate bonding solution, 1 part commercial sodium silicate solution to 6 parts water, dropping volumes in the range $0.1 \div 0.4 \mu\text{l}/\text{cm}^2$. Six of these samples, after 2-3 months curing, were selected for thermal conductivity measurement.

Initial mechanical testing at room temperature of the bonded disks showed that a 5 cm^2 silicon to silicon bond is capable of supporting a 1 MPa shear stress over two weeks without breaking or distortion [148]. Tests have been performed showing that successful bonds can overcome temperature cycles down to cryogenic measurements without significant damages [147]. A similar test carried in our lab immersing one of two bonded silicon disks directly in liquid nitrogen, while the other was in air, proved that high thermal gradients can be supported by the bond without breaking.

Taking into account the oxide layers deposited on silicon disks for allowing the silicate bonding, the layer among the disks is expected to be about 300 nm thick. Taking for the bonding material a conductivity similar to that of glass, the effect of such a thin homogeneous layer on the overall conductance of the sample is expected to be within the mea-



Figure 5.12: Picture of a couple of silicate bonded silicon disks 1' in diameter, 6 mm thick, produced at the University of Glasgow.

surement error except at low T (see figure (5.18)). The conductance of a single silicon disk is as high as ~ 12 W/K at room temperature, so that a power of about 0.05 W is needed for having a $\Delta T \sim 4$ mK across the disk. At cryogenic temperatures, the conductance is more than ten times greater. These numbers give an idea of how challenging is measuring the conductivity for these samples. Necessarily, the setup realized for the test measurement had to be modified. In the following sections, the modified apparatus used for measuring the disks is described and the obtained conductivity curve down to about 60 K is presented and discussed.

5.5.1 Modified apparatus

The apparatus employed for the conductivity measurements on bonded disks is represented schematically in figure (5.13), and a picture of it is shown in figure (5.14). The modifications to each part with respect to the test setup are separately discussed.

Heat sink and support

A massive copper block in thermal contact with the cold plate is used as heat sink. All thermal contacts are realized by inserting in between a cryogenic conductive vacuum grease. The sample flat face is placed between the vertical flat surface of the sink and an aluminium cylinder used as heater, pressed by a PVC screw-tightened block. For avoiding

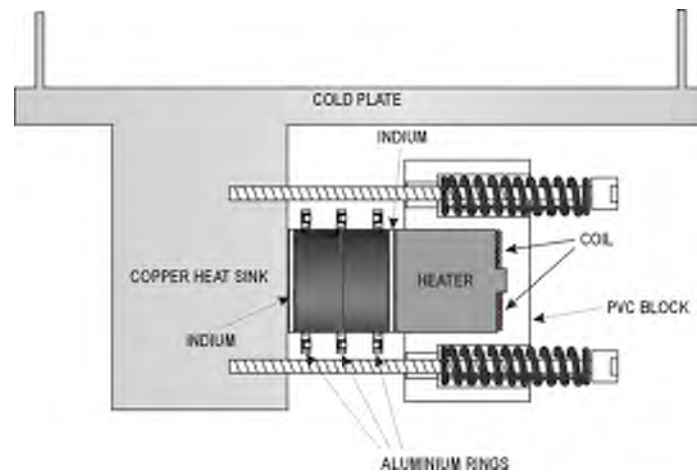


Figure 5.13: Cross sectional scheme of the apparatus realized for measuring the thermal conductivity across silicate bonded silicon disks. The various parts of the apparatus are described in the text.

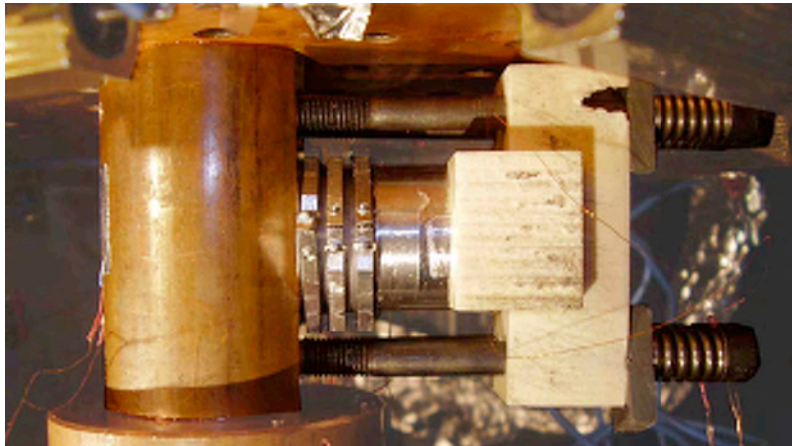


Figure 5.14: Picture of the apparatus schematized in figure 5.13.

mechanical damage to the sample, springs have been inserted among the PVC block and the head of the steel screws. Thermal contraction of the support structure at low temperature proved to be negligible.

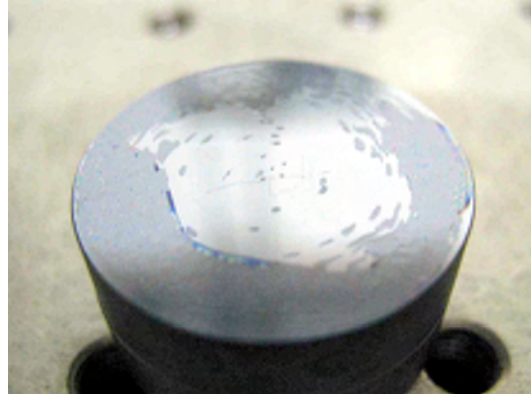


Figure 5.15: The thermal contact among the sample and the sink has been tested with oil. In the picture, a lack of contact in the central region is evident.

Evidence has been found that thermal contact among the sample and the flattened surfaces of the sink and the heater was not good, even using the conductive grease, see figure (5.15). That is due to the fact that, while the silicon disks have been flattened to an high degree of accuracy ($\lambda/10$), the machining of the flat faces on sink and heater is at the level of tenths of a mm. The problem has been fixed by placing indium thin disks among the sample and the contact faces. When the PVC block is tightened, indium is squeezed assuring a good thermal contact everywhere on the surface.

Due to the small emitting surfaces of the sample and to the very low values of thermal gradients, radiation losses are negligible, therefore the thermostatic copper box around the apparatus has been removed.

The temperature of the sink is registered by a PT1000 sensor.

Temperature sensors

As discussed in section (5.2.1), high sensitivity in the measurement of the thermal gradient along the sample is achieved by mounting PT1000 in a bridge configuration. Nevertheless, in the case of bonded disks, this sensitivity is somehow spoiled by geometry uncertainties, since the contact regions of temperature sensors will be no longer point-like with respect to the length of the sample. The sensed temperature is a sort of spatial average.

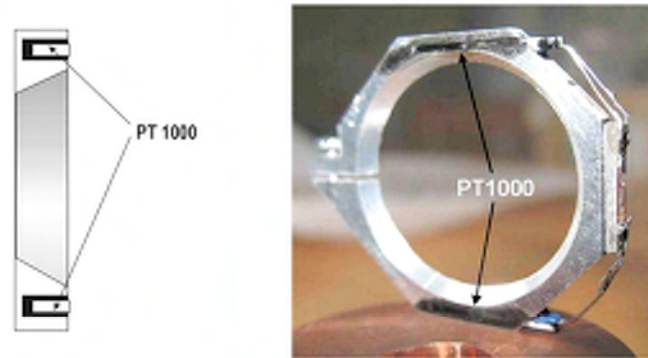


Figure 5.16: Picture and cross sectional view of an aluminium ring hosting 2 PT1000, to be employed for sensing the temperature on the sample.

For avoiding the contact region to be too wide, PT1000 sensors are placed on aluminum rings whose inner edge is sharp (see figure (5.16)). Each ring hosts 2 PT1000, which are glued in grooves machined in the rings, by means of a conductive cement. The sensitivity of the resulting ring sensor is doubled with respect to the single PT1000. The aluminum rings are tightened around the sample, with the aid of precise spacers, so that they touch it at the edges of selected cross sections. This solution allows the temperature to be measured by averaging on a circle around the disk⁴, while the distance among two rings along the sample is well defined and precisely measurable.

Three such rings have been realized and connected in such a way that two resistive bridges are obtained, sharing a branch. A couple of sensors at a distance $L_1 \simeq 4$ mm is placed across a single, pure silicon disk, while the third ring is placed around the other disk, $L_2 \simeq 6$ mm apart. In this way the measurement of conductivity across the bonding layer is made, while the conductivity of pure silicon is also obtained at the same time. The latter will allow the quality of the measurement to be checked, by comparing with the known curve of crystalline Si for $T > 100$ K.

Heater block

A fundamental request for the measurement to be feasible is that the heat flux must be homogeneous within the sample. In case of inhomogeneities, the measured κ values are expected to be severely affected as discussed below in section (5.5.3). Therefore, considering the peculiar concerned

⁴Of course, this operation is meaningful only if the heat flux has an axial symmetry.

geometry, care must be taken in heating homogeneously the flat face of the specimen.

With this aim, a uniplanar constantane coil is stuck on an aluminum cylinder 3 cm long with diameter matching that of the disks, as drawn in figure (5.13). The thermal contact with the sample is assured by an indium foil. The aluminium cylinder is long enough for uniforming the heat flux before it reaches the silicon disks.

5.5.2 Measurements

Measurements of conductivity across both pure silicon disk and bonding layer have been performed down to 77 K using liquid nitrogen. The measurement technique is basically the same as described in section (5.3). Both the bridges have been calibrated by inserting the 100 k Ω resistance in parallel to PT1000. Furthermore, the measurement has been pushed down to about 60 K by removing the nitrogen vapour out of the inner tank with a rotative pump.

The error associated with the values of k is evaluated in this case as:

$$\frac{\Delta\kappa}{\kappa} = \frac{\Delta c}{c} + \frac{\Delta P}{P} + \frac{\Delta(\Sigma/L_i)}{(\Sigma/L_i)} + \frac{\Delta c_{PT1000}}{c_{PT1000}} \quad (5.8)$$

where $\Delta c/c$ is the relative error due to the calibration, $\Delta P/P$, $\Delta(\frac{\Sigma}{L_i})/(\frac{\Sigma}{L_i})$ and $\Delta c_{PT1000}/c_{PT1000}$ are due respectively to the measurement of the power, the geometry and the linearity error of PT1000 declared by the manufacturer. It turns out that the dominating contribution is that coming from the geometry. For all the measured values, $\Delta\kappa/\kappa \simeq 8\%$.

The measurement setup proved to reach an high level of sensitivity in measuring temperature differences on the sample, of the order of few tens of μK , as shown in figure (5.17).

The obtained curves for the conductivity $\kappa(T)$ in silicon and across the bonding layer are shown in figure (5.18), where the reference literature values of $\kappa(T)$ in pure silicon are also reported. Moreover, the computed curve modeling the layer among the two disks as a glass layer 300 nm thick is plotted.

At a first glance, it is clear that there is a discrepancy between the literature curve for pure Si and the measured one. Anyway, the ratio among them is constant throughout the temperature range inspected, and it is about 1.2. This fact has to be related to heat flux inhomogeneities probably due to a non perfectly uniform bonding, as discussed in section (5.5.3).

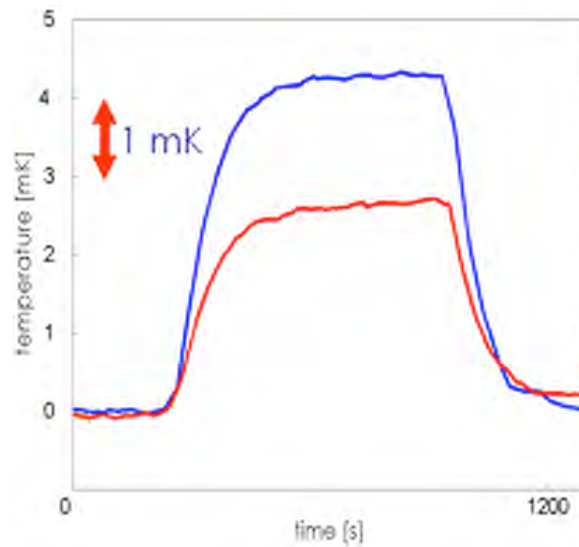


Figure 5.17: Heating curves at room temperature with feeded power 50 mWatts, across the bonding (blue curve) and across pure silicon (red curve). The setup sensitivity is remarkably high, at the level of few tens of μK .

The values of $\kappa(T)$ across the bonding are significantly lower than what is expected. Here, the ratio between the computed curve and the measured one is not constant, becoming larger at low temperatures. This suggests that in addition to flux distortion there could be a different behaviour of the bonding with respect to compact glass.

Nevertheless, the measurement has proved to be definitively affected by inhomogeneities. All the hints obtained with the measurement on bonded disks have thus to be confirmed. As the next step, new samples with a geometry suitable to reduce the crucialness of heat flow uniformity will be produced and measured. Section (5.6) illustrates the present status of the design of new bonded silicon bars.

5.5.3 Effects of inhomogeneities

The method here presented for measuring the thermal conductivity relies on the hypothesis that the heat flows uniformly within the specimen. Nevertheless, in the case of the bonded disks, while the homogeneity of silicon in each disk is almost certain, the bonding layer can be affected by impurities or detachment in small regions. The bonding layer defects can be thought as shields against the heat flux. The effect of such shields is to deform the flux pattern in such a way that cross sectional surfaces

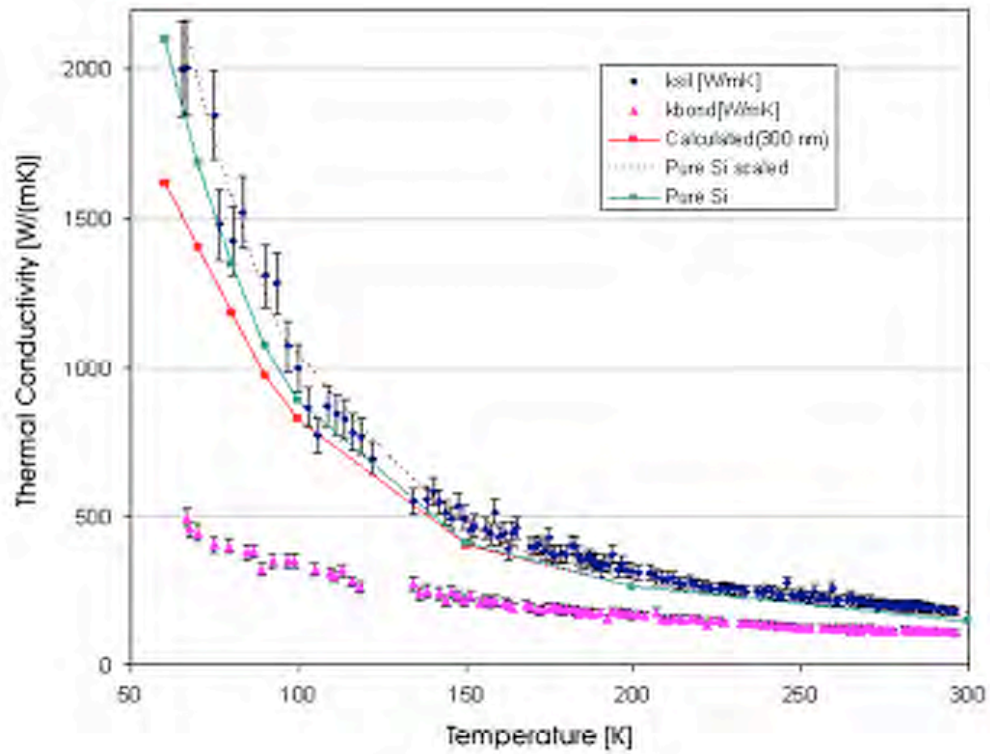


Figure 5.18: Plot of the measured values of $\kappa(T)$ for a silicon disk (blue markers) and across the bonding (pink triangles). The green curve for pure silicon is taken from literature data [111]. The dotted curve is obtained multiplying the green values by 1.2. The red curve is obtained supposing a layer thickness of 300 nm, and assuming the conductivity of glass [149] for the bond.

are no longer isothermal.

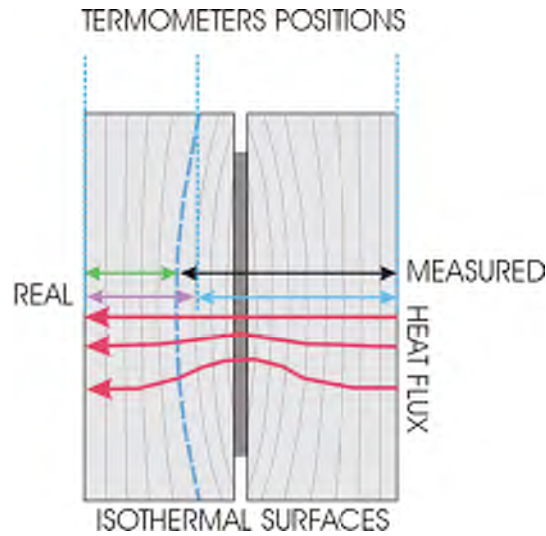


Figure 5.19: Sectional view of a bonded sample with a bonding layer detachment in correspondence of the disks edge. The resulting isothermal bent surfaces and the position of temperature sensors are indicated. The effect of the detachment on the measurement is to underestimate $\kappa(T)$ across the bonding and to overestimate it over the silicon disk, as explained in the text.

Refer to figure (5.19), where a detachment of the bond in correspondence with the edge of the disks is supposed. The resulting isothermal surfaces are bent symmetrically with respect to the layer. Note that the heat flux is almost unperturbed near the central axis of the sample. Here, the conductance is correctly obtained by measuring the temperature gradients indicated by the cyan and purple arrows. Temperature sensors yet record the value of T on the external surface of the specimen. Therefore, we are led to associate the positions of sensors with the wrong temperature gradients, marked with the black and red arrows. In this way, the conductance is overestimated within the silicon disk, while it is underestimated across the bond. It must be noticed that the pattern of isothermal surfaces does not depend upon $\kappa(T)$ provided that the conductivity is independent with respect to the position inside the silicon. Therefore, the ratio between the measured $\kappa(T)$ across pure Si and the conductivity of pure silicon from literature data would not depend upon T .

Different types of inhomogeneities could be present in the bonding layer, giving rise to similar effects, always characterized by a constant ratio between measured and expected curve. In figure (5.20) a simulation

performed with a finite element analysis (FEA) software is shown, where the effect on the temperature field of a small cut 2 mm deep in the bonding layer is considered. In particular, the temperature field is drawn on an aluminum ring with sharp inner edge, very similar to that used in the measurement for sensing T , in contact with the sample. It results in a 30 mK spread of T over a 1K temperature gradient on the whole sample. Depending on the position of PT1000s on the ring, that leads to an error in determining T as high as 3%.

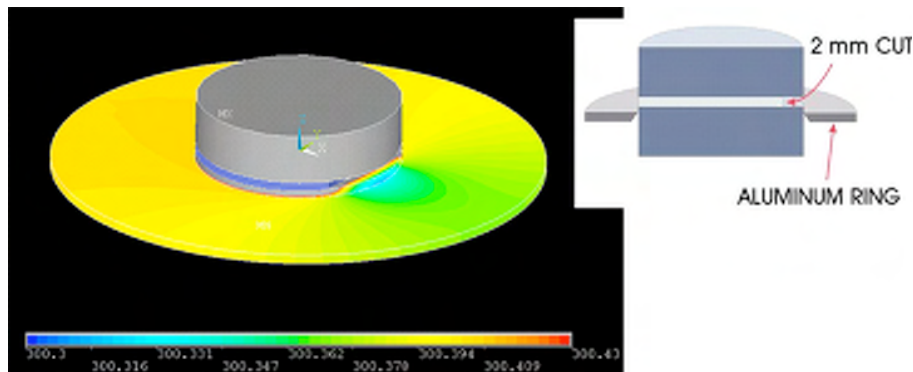


Figure 5.20: Simulation of the temperature field on an aluminum ring with sharp inner edge in contact with one disk, where a small cut 2 mm deep in the bonding layer is made and a $\Delta T = 1$ K is set across the sample at room temperature. A schematic cross section view of the arrangement is shown for clarity.

The uniformity of the heat flow is therefore a basic requirement for measuring κ .

5.6 Simulations on suitable geometry samples

As discussed in the previous section, the next necessary step is to obtain bonded samples with a geometry suitable to get rid of the problem of local inhomogeneities in the bonding layer. Therefore, different possible solutions have been investigated by a finite element analysis. In all these simulations, the bonded surface is of the order of 1 squared inch, similar to that of the disks. The silicon disks are replaced with long silicon reeds with constant cross section, and the profile of temperature along a line on the lateral surface is obtained, for a fixed $\Delta T = 1$ K among the ends of the sample. Then, different types of cuts in the bonding layer are simulated

working out the relative temperature profiles. The bonding layer, too sharp for being simulated in its real dimensions, has been replaced in this computations with a thicker (0.1 mm) layer of a fictitious material, whose conductance has been set to fit that of corresponding bonding layer.

A prospect of the considered geometries and of the simulated bonding layer defects is shown in figure (5.21). A set of temperature profiles, obtained for the geometry labeled *CYL RING* at room temperature, are plotted in figure (5.22). The profiles are drawn for different values of the parameter δ , which is the difference between the radius of the silicon reed cross section and the radius of the circular bonding layer. Very similar results are obtained for the other geometries, even at cryogenic temperatures.

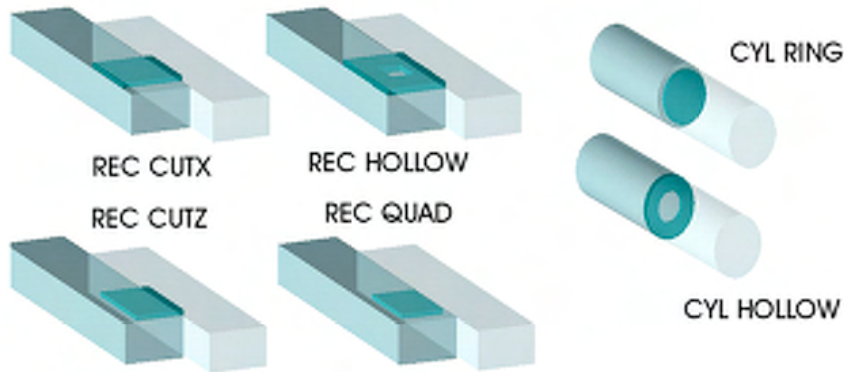


Figure 5.21: Schematic view of the different bonded silicon reeds configurations simulated to be realized for the next measurement runs. For each configuration, one of the two reeds is made transparent for allowing the bonding layer (represented in thick cyan) to be seen. Also reeds faced by side have been considered, since $\lambda/10$ flattening is simpler for lateral longer surfaces.

The simulation proved that at a distance of more than 2 cm from the inhomogeneity, the high value of the silicon conductivity makes the heat flux homogeneous, and the temperature profile is a line. Considering to place two aluminium rings before the layer and two after, and taking into account the fact that also the thermal contact between the sample and the heater or the sink can give rise to inhomogeneities, leads to a conservative reed length of at least 7 – 8 cm. Therefore, samples for next measurements will be supplied by the Glasgow University, which will be realized by silicate bonding two ~ 8 cm long silicon reeds with

cross sectional area $\Sigma \sim 1$ squared inch.

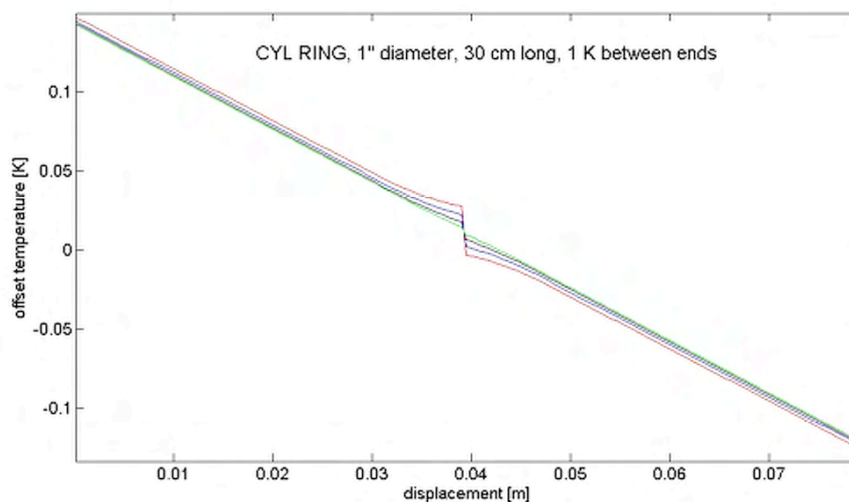


Figure 5.22: Curves of T along a line on the cylinder lateral surface, with model CYL RING and δ ranging from 1 mm (green line) to 5 mm (red line). The layer is placed at 4 cm on x axis. Offset T refers to a mean value $T_0 = 300.5$ K.

5.7 A facility for the measurement of small displacements

In a complete plan for characterizing a silicon suspension element, such as a fibre, one would measure the thermal expansion coefficient $\alpha(T)$ down to cryogenic temperatures and especially at those temperatures where it is expected to vanish. Anyway, α is much less dependent on impurities or defects than κ . A curve like that in figure (4.1) is quite general. Therefore, we planned to realize a facility aimed at measuring α in thin, long samples, but which could be advantageously used more generally in all the phenomena which would involve a measurement of very small displacements. Creep, i.e., sudden release of internal mechanical stresses in suspending fibres, is an example. The test mass motion due to creep events could mimic a gravitational waves burst in a GW detector, therefore it represents a main issue in the noise budget.

The facility is conceived to measure down to cryogenic temperatures, by placing the specimen in a cryostat. In the following, a conceptual

design of the facility is presented; also, the up to now realized part of the facility (that is, the temperature stabilization) is described.

Michelson interferometer and single cavity Fabry-Perot (FP) interferometer have proved to be too poorly sensitive to be employed in silicon α measurement (especially near its zero points); so the adopted strategy turned out to be a double FP cavity. A sketch of that system is shown in figure (5.23). While a reference FP cavity is used to lock the laser at a given frequency, two mirrors placed at the opposite ends of the concerned thin, long sample form a second cavity whose length varies as the sample length varies. It is possible to keep the second cavity in resonance, by changing the reference cavity length with a piezo actuator: the error signal fed to that piezo device can be read as a measurement of the thermal expansion.

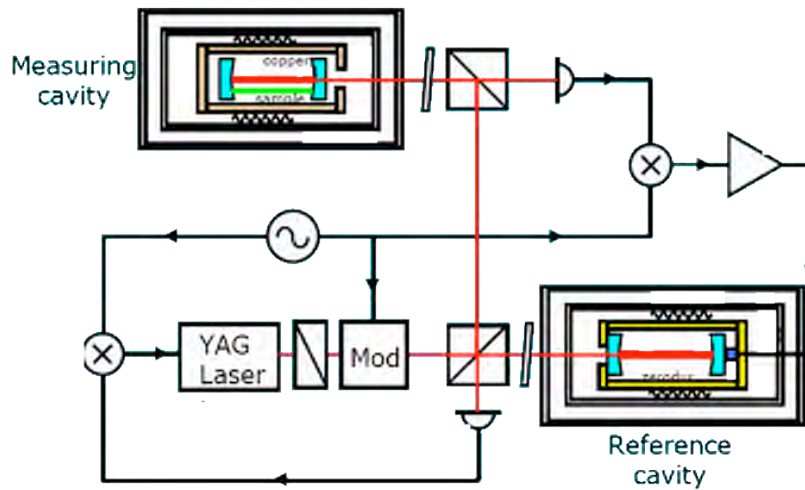


Figure 5.23: Sketch of the FP interferometric setup that will be employed for measuring α in thin rods.

As pointed out, in order to realize such interferometer the laser light that will be employed should be made as frequency stable as possible. A good stabilization can be attained by means of a suitable reference cavity: that is, a fixed-length FP cavity. The cavity resonance condition being maintained by a control loop which acts directly on the laser frequency tuning, it is possible to lock the laser light at a given wavelength, provided that the cavity length remains constant. It is clear that a very rigid and thermal stable support must be chosen for blocking⁵ the mirrors at the

⁵Actually, since the measurement of thermal expansion will request an active con-

ends of the cavity. A simplified scheme of the support realized with this aim is sketched in figure (5.24).



Figure 5.24: Scheme of the reference Fabry-Perot cavity, to be used for laser frequency stabilization.

Mirrors are stuck at the ends of a zerodur hollow cylinder, rigidly clamped on a V-shaped aluminium block. Clamping occurs in the cylinder middle point, by means of a screw-tightened collar. The reference cavity must be kept at very low pressure for avoiding refraction index fluctuation in air.

Zerodur glass ceramic has a very low expansion coefficient, that is roughly $\alpha < 10^{-7} \text{ K}^{-1}$; though this fact would guarantee a very small variation of cavity length with temperature fluctuations, a thermal stabilization of the support will be needed for making thermal expansion effects negligible. It is possible to simply estimate the stabilization goal, once few reasonable assumptions are made on system dimensions and typical α values. Let us suppose the sample length equal to that of the cavity, and take $\alpha \simeq 10^{-7} \text{ K}^{-1}$ in silicon at low temperatures (for instance, near zero points). In order to neglect the length variations of the reference cylinder, the condition:

$$\Delta L_R \ll \Delta L_S \quad (5.9)$$

must hold, where subscripts S and R refer to the sample and the reference. That is:

$$\Delta T_R \ll \frac{\alpha_S \Delta T_S}{\alpha_R} \quad (5.10)$$

Measurement will be performed by heating the sample at a given temperature, by an amount $\Delta T_S \simeq 1 \text{ K}$, thus:

$$\Delta T_R \ll 1K \quad (5.11)$$

control on end mirror displacement, a piezoelectric actuator will be placed against one of the end mirrors.

Therefore, the temperature should be stabilized within fluctuations of $\Delta T_R \sim 10^{-2}$ K during a measurement time (of the order of ten minutes).

The temperature stabilization system is the only part of the facility which is completed, and it will be described below. As detailed in the following, the stabilization has been reached at about 316 K, with residual oscillations within $\pm 2 \cdot 10^{-3}$ K.

5.7.1 Setup

In order to achieve the designed vacuum level inside the cavity, the zerodur cylinder has been placed in a vacuum tank (refer to figure (5.25)), together with mirrors, piezoelectric device and ancillary parts.

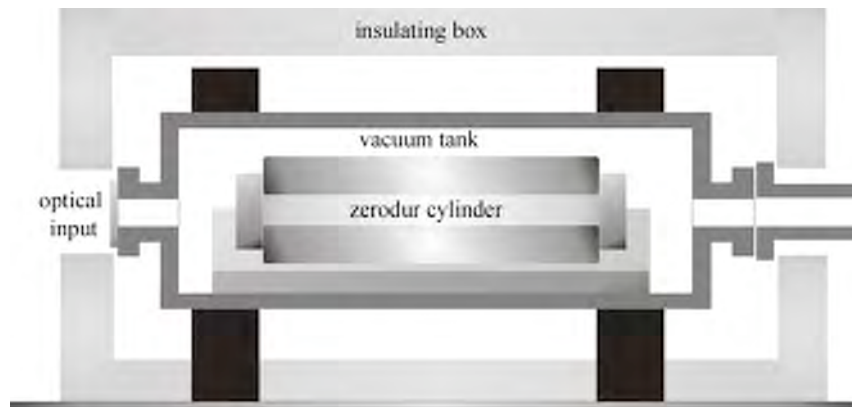


Figure 5.25: Scheme of the reference Fabry-Perot cavity, to be used for laser frequency stabilization.

A specific support structure for cylinder and mirrors has been designed and realized, and it is shown in figures (5.26), (5.27); that is, a V-shaped aluminium block hosts the cylinder and two shaped springs mounted on it keep the mirrors in place. The whole support is blocked inside the tank by pressing screws.

The vacuum tank is connected by flexible pipes to a vacuum pumping stage; a pressure of less than 10^{-3} mbar at room temperature can be rapidly reached.

The cavity temperature can be more easily stabilized if the tank is thermally insulated from the environment. That results in a poor heat flux toward the exterior, that is the heat power needed to maintain the cavity at a given temperature is minimized. For obtaining a good insulation, the steel tank is supported by two PVC blocks inside a polyurethane

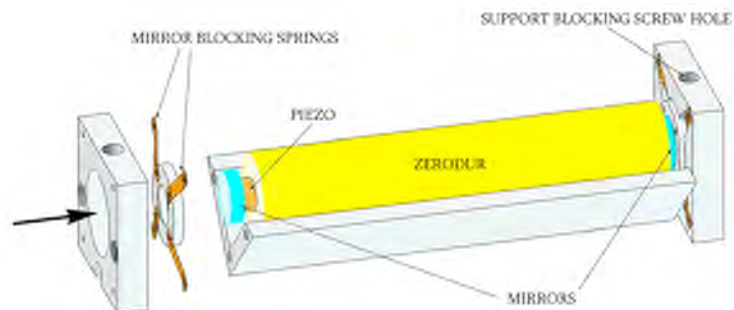


Figure 5.26: Support system for assembling the reference cavity inside the vacuum tank.

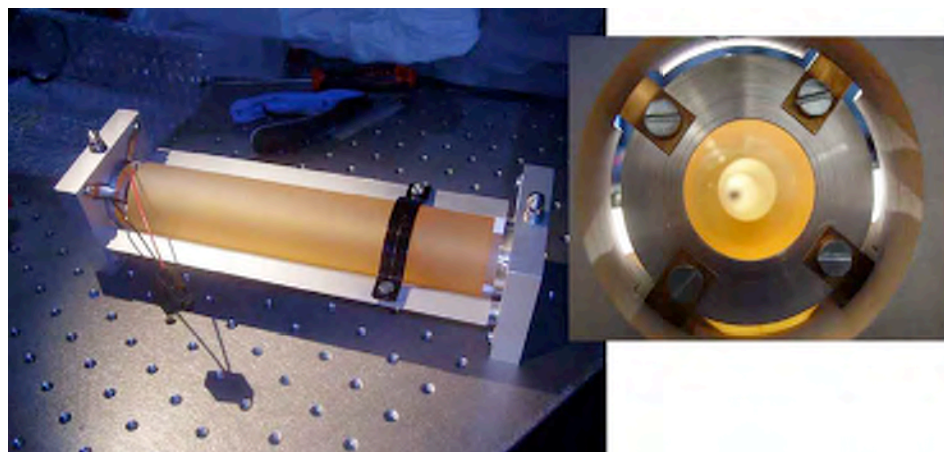


Figure 5.27: Pictures of the zerodur cylinder assembly.

3 cm thick box. Thus the whole system should behave roughly according to the equation (see (5.2)):

$$C\dot{\theta}(t) + k\theta(t) = P(t) \quad (5.12)$$

where $\theta(t) = T - 295$ is the difference between the temperature of the tank and the room temperature. A power $P(t)$ poured in the tank leads to a (positive) variation of θ that is determined by two parameters: the capacity C which fixes the initial rate of the system response to a power change, and the effective conductivity k which select the regime level. Actually, for the cavity θ does not follow exactly the law in equation (5.12) (as it will be discussed below), but the deviations are small enough to allow the use of (5.12) for estimating C and k .

Active control is needed to reach the requested temperature stabilization (refer to figure (5.28)): that is, a feedback able to deliver to the tank the right amount of power for compensating environmental variations of T . The cavity has to be kept at a temperature different from that of the room, in order to have a stiff control (or, in other words, a regime power different from zero).

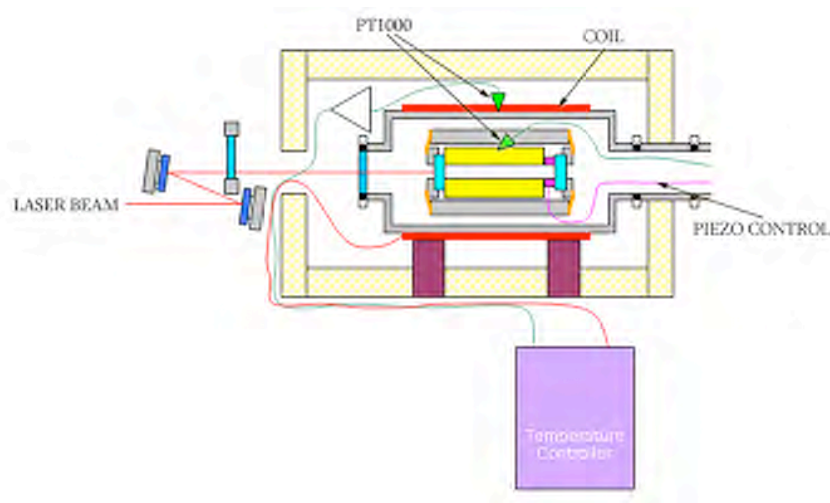


Figure 5.28: Feed-back assembly for stabilizing the reference cavity temperature. PT1000 temperature sensors are placed on the tank surface and inside it, in touch with the zerodur cylinder. A control circuitry feeds the copper coil heater.

Power is provided by means of Joule current dissipation: around the steel tank a $200 \mu\text{m}$ insulated copper wire has been coiled (see figure (5.29)), with a total electrical resistance of $\sim 9.2 \Omega$ (it depends slightly on the temperature). The coil has been wrapped in a polystyrene layer

for shielding outward losses. The maximum power to be transferred to the cavity by Joule effect on the wire is limited by the maximum current the generator can supply, that is 1 A in this case. Thus:

$$P_M = (1A)^2 \cdot (9.2 \Omega) = 9.2 W \quad (5.13)$$



Figure 5.29: A picture of the steel vacuum tank with the coiled copper wire.

The cavity inner and outer temperature is acquired by means of PT1000 sensors. While a PT1000 is placed in contact with the outward surface of the vacuum tank, the other stays inside, pressed against the zerodur cylinder. Each resistor is connected in a bridge for measuring its resistance, thus allowing a very sensitive evaluation of the temperature, provided that the characteristic PT1000 curve is known. Only the outer PT1000 is employed in the feedback.

In the following the controller design procedure is presented, and the resulting stabilization performances are reported and commented.

5.7.2 Controller design and test

Once a set point θ_R for the cavity temperature has been chosen such that the required regime power is less than 9.2 W, and the system response to a power variation (its power to temperature transfer function) has been obtained, it becomes possible to design a loop which takes as error signal

the difference between measured temperature and set point, and consequently controls the current injected in the coil; the transfer function can be either extracted from a physical model of the cavity by fitting model parameters, or worked out from a measurement.

Let us firstly consider equation (5.12). If the system is initially at $\theta = \theta_0$, and the power provided to the coil raises suddenly to a level P_0 :

$$P(t) = P_0 \Theta_H(t) \quad (5.14)$$

accordingly to that equation the subsequent behavior of $\theta(t)$ is:

$$\theta(t > 0) = \frac{P_0}{k} + \left(\theta_0 - \frac{P_0}{k}\right)e^{-\frac{k}{C}t} \quad (5.15)$$

The knowledge of the two quantities k and C determines the system; these values can be experimentally evaluated.

Regarding the equation (5.15) as valid for the cavity, it is clear that, as the power is switched on, the slope of θ depends on both k and C :

$$\dot{\theta}(t = 0) = -\theta_0 \frac{k}{C} + \frac{P_0}{C} \quad (5.16)$$

but in the case $\theta_0 = 0$ it is fixed only by C (and of course P_0). Furthermore, the regime value turns to be:

$$\theta(t \rightarrow \infty) = \frac{P_0}{k} \quad (5.17)$$

Therefore, a measurement can be performed by switching on the power in the coil and acquiring θ . This has been done and led to the k and C values reported in table (5.2).

P_0	k	C
9.2 W	0.33 W/K	3000 W s/K

Table 5.2: Values of k and C measured for the cavity stabilization assembly.

By using values in table (5.2), the system behavior with a given θ_0 can be computed and compared with the experiment. As it can be seen in figure (5.30) ($\theta_0 = 25.44K$), the agreement is not good, suggesting that equation (5.12) should be somehow discarded; however, the overall trend is reproduced, so the simple model with C and k can be regarded as roughly correct.

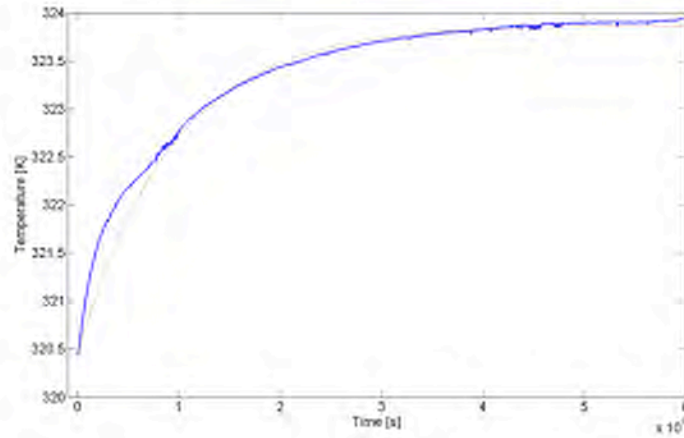


Figure 5.30: Temperature response of the system to a power step, with initial condition $\theta_0 = 25.44$ K (solid line). Experimental result is compared with the prediction of the simple model of equation 5.12 (dashed line).

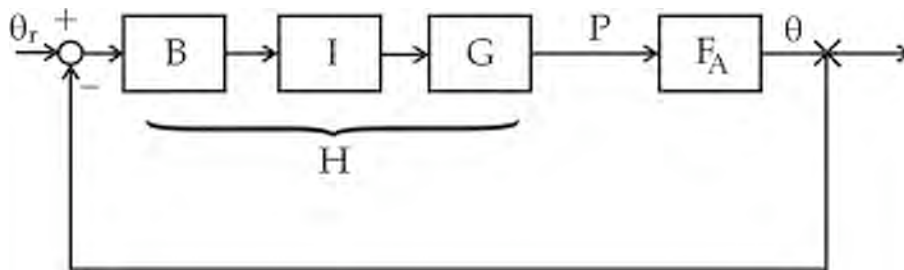


Figure 5.31: Block diagram of the feed-back loop realized for the cavity.

Once k and C are known, the feed-back loop has been designed; the control strategy has been decided to involve a PI controller. The basic scheme of the complete feed-back loop is reported in figure (5.31).

The assembly is represented by the measured transfer function F_A ; in order to obtain the overall transfer function, the power injected P must be linearized around the working temperature:

$$\delta P = \delta(I^2) R_c \simeq 2I_0 \delta I R_c$$

where I_0 depends on the chosen set point ($I_0=0.88$ A for $T=316$ K), R_c is the coil resistance. The B labeled block contains the bridge for converting the temperature in a voltage signal ΔV , while the G block represents the overall gain of the proportional controller. The integral controller I has a time constant $\tau = R_I C$, so the controlling chain has a transfer function given by:

$$H(s) = 2I_0 R_c B \frac{1}{R_I C s} G \quad (5.18)$$

The feed-back stability is granted by choosing a suitable value for τ : we set $\tau = 220$ s. Thus the open loop transfer function turns to be:

$$H_{OL} = F_A H \quad (5.19)$$

while the closed loop transfer function is:

$$H_{CL} = \frac{F_A H}{1 + F_A H} \quad (5.20)$$

Transfer functions H_{OL} and H_{CL} are plotted in figures (5.32) and (5.33). As it can be seen, the loop resonance is well damped; and the proportional controller gain can be reduced with a potentiometer for further resonance damping.

The control parameters are thus determined for the system; however, such determination has been obtained by means of equation (5.12), which we know to be incorrect. Though the temperature stabilization can be reached by using the PI controller described, as it will be shown in the following by experimental proof, we performed a direct measurement of the transfer function in order to fully characterize the system.

Let us inject in the system a power P_0 and wait for the regime temperature to be reached; then, let switch suddenly off the power. The system response is:

$$\theta(t) = P_0 \int_{-\infty}^t h(t-s)(1 - \Theta_H(s)) ds \quad (5.21)$$

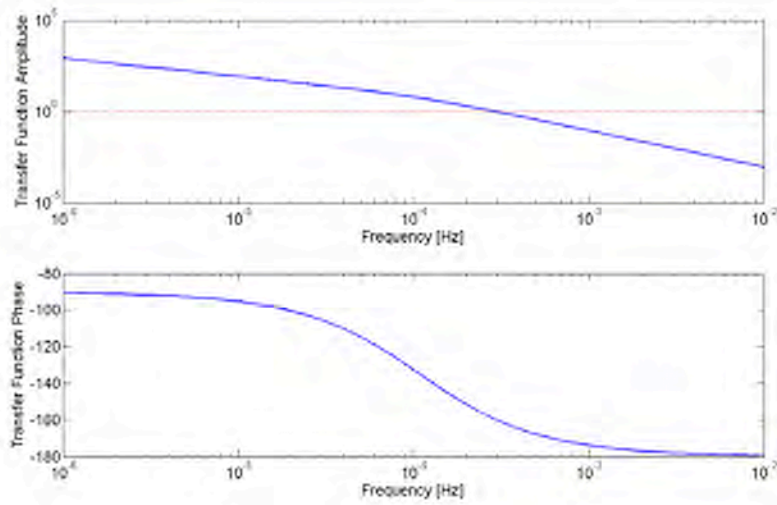


Figure 5.32: Open loop transfer function H_{OL} of the control system. Red dashed curve corresponds to unity gain condition $H_{OL}=1$.

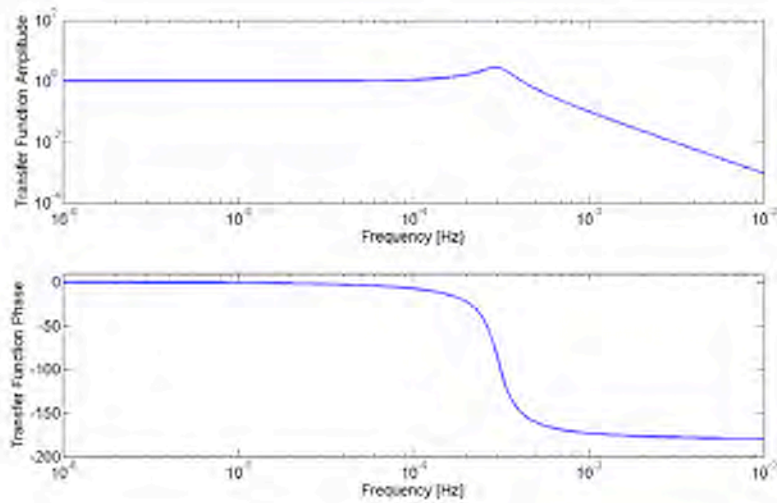


Figure 5.33: Closed loop transfer function H_{CL} of the control system.

with initial condition $\theta = \theta_0$, where $h(t)$ is the impulse response. Since F_A is equal to the Laplace transform of $h(t)$, once $\theta(t)$ has been measured, the transfer function can be worked out:

$$F_A \equiv \mathcal{L}(h(t)) = \frac{\mathcal{L}\left(-\frac{d\theta(t)}{dt}\right)}{P_0} \quad (5.22)$$

In figure (5.34) a fit of measured $\theta(t)$ using a sum of three exponentials is shown. The agreement is quite good, so the fit parameters (reported in table (5.3)) allow the determination of F_A as in equation (5.22).

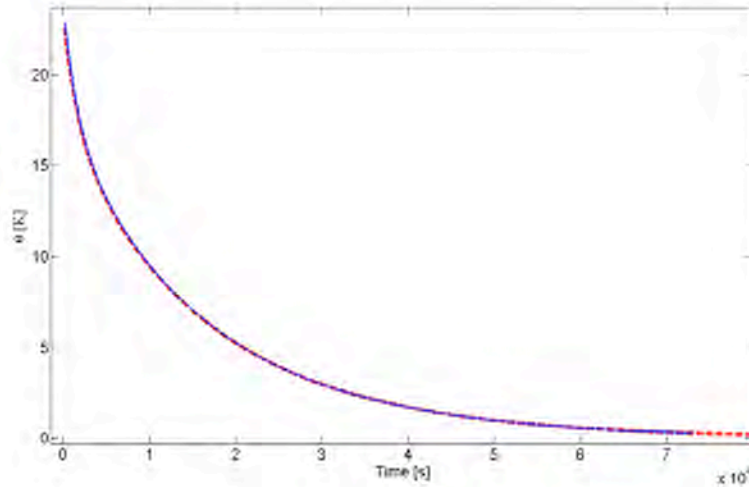


Figure 5.34: System response to a power off switching: measured (solid line) and fit (dashed line).

$$\theta(t) = Ae^{at} + Be^{bt} + Ce^{ct} + D$$

A	a	B	b	C	c	D
-3.8	$-1.1 \cdot 10^{-4}$	-5.4	$-6.4 \cdot 10^{-4}$	-13.9	$-5.3 \cdot 10^{-5}$	22.67

Table 5.3: Fitted parameters for the system response to a power off switching.

For testing the validity of that evaluation of F_A , the feed-back has been enabled with the cavity at a temperature $\theta_1=18.75$ K, and with set point $\theta_0=20.8$. If the feed-back set point is changed suddenly by a finite amount $\Delta\theta = \theta_0 - \theta_1$ at $t = 0$, after it reached a regime condition, then:

$$\theta(t) = \Delta\theta S(t) + \theta_1 \quad (5.23)$$

where:

$$S(t) = \int_0^t H_{CL}(Y) dY \quad (5.24)$$

is the unit step response of the system. This $\theta(t)$ is compared with experimental record in figure (5.35). As it can be seen, except for the initial slope, the measured response is quite similar to that in equation (5.23). Initial discrepancy can be thought as due to the fact that, instead of changing the set point, the control loop has been turned from inactive to active. In addition, enabling occurred when the cavity temperature was dropping freely after a pre-heating phase.

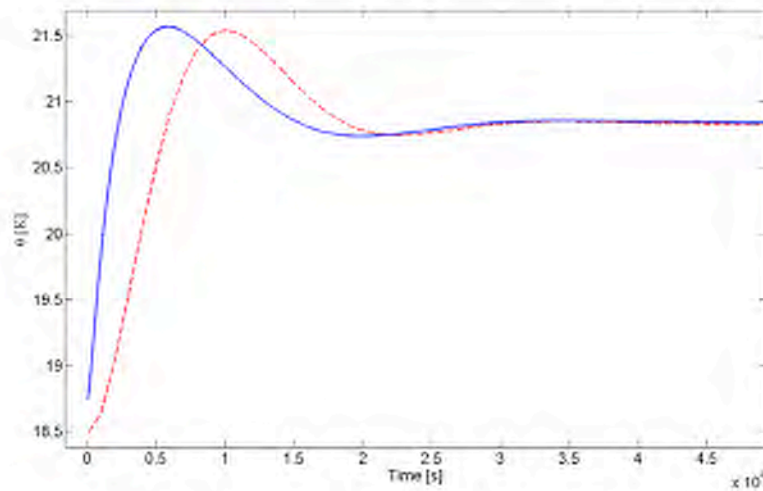


Figure 5.35: System behavior after enabling the closed loop control (solid line). The dashed line draws the step response as computed by using the measured transfer function F_A .

The designed controller has been tested, by switching on the control and collecting temperature values on the cavity tank and at the zerodur surface, in vacuum conditions ($\sim 10^{-3}$ mbar), for a period of several hours after the stabilization. As it can be seen in figure (5.36), the stability is granted within less than 10^{-2} K for both inner and outer temperatures; inside the tank T has residual oscillations of about $4 \cdot 10^{-3}$ K at a temperature of 315.7 K.

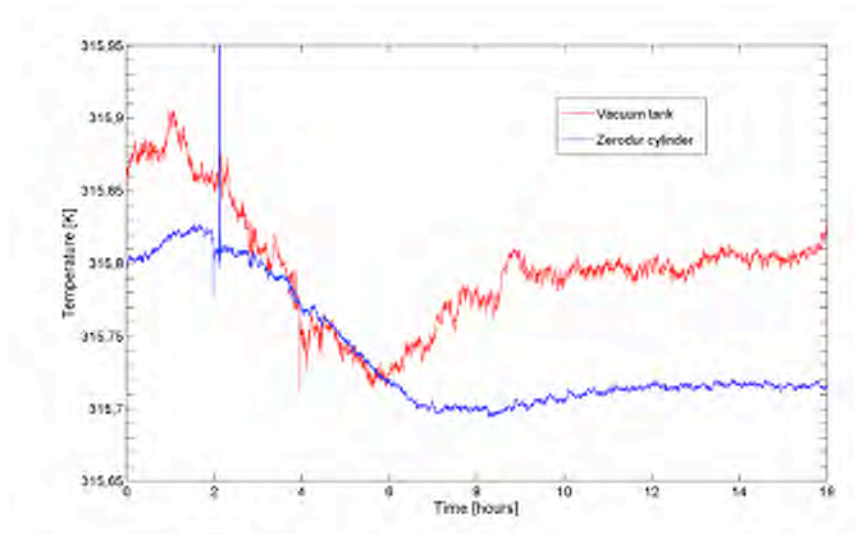


Figure 5.36: Temperatures measured on the vacuum tank (red line) and on the zerodur cylinder (blue line) after the stabilization set point has been reached.

5.8 Conclusions

The realized apparatus for the thermal conductivity measurement proved to be able to reach a very good sensitivity down to LHe temperatures, so that it can be employed in many applications in the research and development activity for cryogenic suspensions. The facility is now at disposal of the international European community working on the third generation GW detectors; the design study for a third generation European interferometer (ET) is now beginning. Moreover, a facility for the measurement of small displacements is being realized in our laboratories.

Concerning the silicon to silicon silicate bonding conductivity, our activity primarily proved the importance of the bonding homogeneity in regulating the heat flux; though the measurements need to be repeated with more suitable samples, our investigation on silicate bonding with $\sim 1'$ area suggests that conductivity measurements could be advantageously used for testing the goodness and homogeneity of the bond layer.

Bibliography

- [1] S. Bonazzola and E. Gourgoulhon, *Experimental Physics of Gravitational Waves*, ch. Physics of Sources of Gravitational Waves, pp. 62–106. World Scientific, 1999. Ed. by M. Barone, G. Calamai, M. Mazzoni, R. Stanga and F. Vetrano.
- [2] A. Giazotto *Phys. Rep. C*, vol. 182, p. 365, 1989.
- [3] A. Abramovici et al. *Science*, vol. 256, p. 352, 1992.
- [4] K. Danzmann et al., “GEO600: Proposal for a 600m Laser Interferometric Gravitational Wave Antenna,” *Max-Planck Institut für Quantenoptik Report No. 190*, 1994. Garching, Germany.
- [5] K. T. et al., *Proceedings of the International Conference on Gravitational Waves, Sources and Detectors*. Edited by I. Ciufolini and F. Fiducaro.
- [6] A. Einstein *Königlich Preußischen Akademie der Wissenschaften zu Berlin, Sitzungsberichte*, p. 688, 1916.
- [7] I.R. Kenyon, *General Relativity*. Oxford University Press, 1990.
- [8] P.R. Saulson, *Fundamentals of Interferometric Gravitational Wave Detectors*. World Scientific, Singapore, 1994.
- [9] R.A. Hulse and J.H. Taylor *Astroph. Journ.*, vol. 195, pp. L51–L53, 1975.
- [10] V.B. Braginsky and A.B. Manukin, *Measurements of Weak Forces in Physics Experiments*. University of Chicago Press, 1977.
- [11] J. Weber *Phys. Rev.*, vol. 117, p. 306, 1960.
- [12] M. Cerdonio et al. *Phys. Rev. Lett.*, vol. 87, 2001. 031101.
- [13] L. Ju, D.G. Blair and C. Zhao *Rep. Prog. Phys.*, vol. 63, pp. 1317–1427, 2000.
- [14] B.F. Schutz *Class. Quantum Grav.*, vol. 13, pp. A219–A238, 1996.

- [15] R.V. Wagoner *Astrophys. J.*, vol. 278, p. 345, 1984.
- [16] B.F. Schutz *Nature*, vol. 323, p. 310, 1986.
- [17] B.F. Schutz *Class. Quantum Grav.*, vol. 16, pp. A131–A156, 1999.
- [18] M. Burgay, N. D’Amico, A. Possenti, R.N. Manchester, A.G. Lyne, B.C. Joshi, M.A. McLaughlin, M. Kramer, J.M. Sarkisian, F. Camilo, V. Kalogera, C. Kim and D.R. Lorimer *Astroph. Journ.*, vol. 1, 2003.
- [19] A.G. Lyne, M. Burgay, M. Kramer, A. Possenti, R.N. Manchester, F. Camilo, M.A. McLaughlin, D.R. Lorimer, N. D’Amico, B.C. Joshi, J. Reynolds and P.C.C. Freire *Astroph. Journ.*, vol. 1, 2004.
- [20] J.A. de Freitas Pacheco, T. Regimbau, S. Vincent and A. Spallicci *Int. J. Mod. Phys. D*, vol. 15, pp. 235–250, 2006.
- [21] R. O’Shaughnessy, C. Kim, V. Kalogera and K. Belczynski, “Constraining Population Synthesis Models via Empirical Binary Compact Object Merger and Supernovae Rates,” 2007. arXiv:0610076v6 [astro-ph].
- [22] R.M. O’Leary, R. O’Shaughnessy and F.A. Rasio, “Dynamical Interactions and the Black Hole Merger Rate of the Universe,” 2007. arXiv:0701887v2 [astro-ph].
- [23] K.S. Thorne, *Proceedings of IAU Symposium 165, Compact Stars in Binaries*, ch. Gravitational Waves from Compact Bodies. 1995.
- [24] G. Losurdo, *Ultra-Low Frequency Inverted Pendulum for the Virgo Test Mass Suspension*. PhD thesis, Scuola normale superiore di Pisa, 1998.
- [25] E.D. Black, “Notes on thermal noise, with a bibliography,” 2003. LIGO technical note, LIGO-T030142-00-R.
- [26] G. Cella et al. *Class. Quantum Grav.*, vol. 15, no. 11, pp. 3339–, 1998.
- [27] F. Acernese et al. *Journ. Phys.*, vol. 32, pp. 223–229, 2006.
- [28] The Virgo Collaboration, “Advanced virgo conceptual design,” 2007. VIR-042A-07.
- [29] H.B. Callen and T.A. Welton *Phys. Rev.*, vol. 83, p. 34, 1951.
- [30] H.B. Callen and R.F. Greene *Phys. Rev.*, vol. 86, p. 702, 1952.
- [31] L.E. Reichl, *A Modern Course in Statistical Physics*. Univ. Texas Press, Austin, 1980.

- [32] L.D. Landau and E.M. Lifshitz, *Statistical Physics*. Pergamon Press, Oxford, 1980.
- [33] R. Brown *Phil. Mag.*, vol. 61, 1828.
- [34] A. Einstein *Ann. d. Phys.*, vol. 17, p. 549, 1905.
- [35] A. Einstein *Ann. d. Phys.*, vol. 19, pp. 371–381, 1906.
- [36] A. Gillespie and F. Raab *Phys. Rev. D*, vol. 52, no. 2, pp. 577–585, 1995.
- [37] N. Nakagawa, A.M. Gretarsson, E.K. Gustafson and M.M. Fejer *Phys. Rev. D*, vol. 65, pp. 1–7, 2002.
- [38] Y. Levin *Phys. Rev. D*, vol. 57, no. 2, pp. 659–663, 1998.
- [39] A.S. Nowick and B.S. Berry, *Anelastic Relaxation in Crystalline Solids*. Academic Press, New York, 1972.
- [40] R.D. Peters, “Model of Internal Friction Damping in Solids,” 2002. arXiv:physics/0210121v1 [physics.class-ph].
- [41] L. Onsager *Phys. Rev.*, vol. 32, pp. 405–426, 1931.
- [42] G. Cagnoli, J. Hough, D. DeBra, M.M. Fejer, E. Gustafson, S. Rowan and V. Mitrofanov *Phys. Lett. A*, vol. 272, pp. 39–45, 2000.
- [43] A.L. Kimball and D.E. Lovell *Phys. Rev.*, vol. 30, p. 948, 1927.
- [44] C. Zener *Phys. Rev.*, vol. 52, p. 230, 1937.
- [45] C. Zener *Phys. Rev.*, vol. 53, p. 90, 1938.
- [46] C. Zener, *Elasticity and Anelasticity of Metals*. University of Chicago Press, Chicago, 1948.
- [47] J. Ferreira, *The Detection of Gravitational Waves*, ch. Internal Friction in High Q Materials, pp. 116–168. Cambridge University Press, 1991. Ed. by D. Blair.
- [48] G. Cagnoli and P.A. Willems *Phys. Rev. B*, vol. 65, p. 174111, 2002.
- [49] P.R. Saulson, R.T. Stebbins, F.D. Dumont and S.E. Mock *Rev. Sci. Instrum.*, vol. 65, p. 182, 1994.
- [50] F. Marchesoni, G. Cagnoli and L. Gammaitoni *Phys. Lett. A*, vol. 187, pp. 359–364, 1994.
- [51] A. Gillespie and F. Raab *Phys. Lett. A*, vol. 178, p. 357, 1993.

- [52] C.C. Speake, T.J. Quinn, R.S. Davis and S.J. Richmann *Meas. Sci. Technol.*, vol. 10, pp. 430–434, 1999.
- [53] V.B. Braginsky, V.P. Mitrofanov and V.I. Panov, *Systems with Small Dissipation*. University of Chicago, Chicago, 1985.
- [54] N.W. Ashcroft and N.D. Mermin, *Solid State Physics*. Holt, Reinhart and Winston, New York, 1976.
- [55] H.J. Maris *Phys. Rev.*, vol. 188, no. 3, p. 1303, 1969.
- [56] H.J. Maris, *Physical Acoustics*, vol. VIII. Edited by W.P. Mason.
- [57] T.O. Woodruff and H. Ehrenreich *Phys. Rev.*, vol. 123, p. 1553, 1961.
- [58] M. Usui and S. Asano *Scripta Mater.*, vol. 34, no. 1, pp. 97–101, 1996.
- [59] J.L. Snoek *Physica*, vol. 6, p. 591, 1939.
- [60] A.V. Granato and K. Lücke *J. Appl. Phys.*, vol. 27, no. 6, p. 583 and 789, 1956.
- [61] Y. Nishino, Y. Ota and T. Kawazoe *Mater. Sci. Eng. A*, vol. 370, pp. 146–149, 2004.
- [62] F. Marchesoni and F. Patriarca *Phys. Rev. Lett.*, vol. 72, p. 4101, 1994.
- [63] A.V. Granato and K. Lücke *Phys. Rev. B*, vol. 24, p. 6991, 1981.
- [64] A.V. Granato and K. Lücke *Phys. Rev. B*, vol. 24, no. 15, pp. 7007–7017, 1981.
- [65] J.P. Hirth and J. Lothe, *Theory of Dislocations*. Jhon Wiley, New York, 1982.
- [66] A. Seeger and C. Wüthrich *Nuovo Cim.*, vol. 33B, p. 38, 1976.
- [67] A.M. Gretarsson and G.M. Harry *Rev. Sci. Instrum.*, vol. 70, no. 10, pp. 4081–4087, 1999.
- [68] P.R. Saulson *Phys. Rev. D*, vol. 42, no. 8, pp. 2437–2445, 1990.
- [69] A. Gillespie and F. Raab *Phys. Lett. A*, vol. 190, p. 213, 1994.
- [70] J.E. Logan, J. Hough and N.A. Robertson *Phys. Lett. A*, vol. 183, p. 145, 1993.
- [71] C. Brif, “Notes on anelastic effects and thermal noise in suspensions of test masses in interferometric gravitational wave detectors,” 1999. LIGO technical note, LIGO-T990041-00-R.

- [72] V.B. Braginsky, V.P. Mitrofanov and K.V. Tokmakov *Phys. Lett. A*, vol. 218, p. 164, 1996.
- [73] V.B. Braginsky, V.P. Mitrofanov and K.V. Tokmakov *Phys. Lett. A*, vol. 186, p. 18, 1994.
- [74] J.E. Logan, J.Hough and R.D. Thomson *Phys. Lett. A*, vol. 218, pp. 181–189, 1996.
- [75] V.B. Braginsky, V.P. Mitrofanov and S.P. Vyatchanin *Rev. Sci. Instrum.*, vol. 65, p. 3771, 1994.
- [76] G.I. Gonzalez and P.R. Saulson *J. Acoust. Soc. Am.*, vol. 96, p. 207, 1994.
- [77] F. Bondu and J.Y. Vinet *Phys. Lett. A*, vol. 198, pp. 74–78, 1995.
- [78] E. Campagna, *Modeling some Sources of Thermal Noise through Finite Element Analysis: Application to the Virgo Interferometric Antenna*. PhD thesis, Galileo Galilei School of Graduate Studies, Università di Pisa, 2004.
- [79] S.D. Penn, A. Ageev, D. Busby, G.M. Harry, A.M. Gretarsson, K. Numata and P. Willems *Phys. Lett. A*, vol. 352, pp. 3–6, 2006.
- [80] E.R.M. Crooks et al. *Class. Quantum Grav.*, vol. 19, pp. 883–896, 2002.
- [81] S.D. Penn et al. *Class. Quantum Grav.*, vol. 20, pp. 2917–2928, 2003.
- [82] V.B. Braginsky and A.A. Samoilenko *Phys. Lett. A*, vol. 315, no. 3-4, pp. 175–177, 2003.
- [83] L. Ju, M. Notcutt, D. Blair, F. Bondu and C.N. Zhao *Phys. Lett. A*, vol. 218, pp. 197–206, 1996.
- [84] S. Rowan, J. Hough and D.R.M. Crooks *Phys. Lett. A*, vol. 347, pp. 25–32, 2005.
- [85] G. Cagnoli, L. Gammaitoni, J. Hough, J. Kovalik, S. McIntosh, M. Punturo and S. Rowan *Phys. Rev. Lett.*, vol. 85, no. 12, p. 2442, 2000.
- [86] P. Amico, L. Bosi, L. Carbone, L. Gammaitoni, F. Marchesoni, M. Punturo, F. Travasso and H. Vocca *Rev. Sci. Instrum.*, vol. 73, no. 9, pp. 3318–3323, 2002.
- [87] H. Vocca, *Studio del rumore termico in regime di stazionarietà e di non-stazionarietà per l'interferometro Virgo*. PhD thesis, Università degli Studi di Perugia, 2003.

- [88] A.M. Gretarsson, G.M. Harry, S.D. Penn, P.R. Saulson, W.J. Startin, S. Rowan, G. Cagnoli and J.Hough *Phys. Lett. A*, vol. 270, pp. 108–114, 2000.
- [89] S. Rowan, R. Hutchins, A. McLaren, N.A. Robertson, S.M. Twyford and J. Hough *Phys. Lett. A*, vol. 227, pp. 153–158, 1997.
- [90] G. Cagnoli, L. Gammaitoni, J. Kovalik, F. Marchesoni and M. Punturo *Phys. Lett. A*, vol. 255, pp. 230–235, 1999.
- [91] S. Rowan, S.M. Twyford, R. Hutchins, J. Kovalik, J.E. Logan, A. McLaren, N.A. Robertson and J. Hough *Phys. Lett. A*, vol. 233, pp. 303–308, 1997.
- [92] A. Heptonstall, G. Cagnoli, J. Hough and S. Rowan *Phys. Lett. A*, vol. 354, pp. 353–359, 2006.
- [93] S.D. Penn, G.M. Harry, A.M. Gretarsson, S.E. Kittelberger, P.R. Saulson, J.J. Schiller, J.R. Smith and S.O. Swords *Rev. Sci. Instrum.*, vol. 72, pp. 3670–3673, 2001.
- [94] G. White *J. Phys. D: Appl. Phys.*, vol. 6, p. 2070, 1973.
- [95] M. Fukuhara, A. Sanpei and K. Shibuki *J. Materials Science*, vol. 32, p. 1207, 1997.
- [96] M. Fukuhara and A. Sanpei *J. Materials Science Lett.*, vol. 18, p. 751, 1999.
- [97] A. Heptonstall, I. Martin, A. Cumming, C.A. Cantley, G. Cagnoli, R. Jones and D.R.M. Crooks, “Production and characterization of synthetic fused silica ribbons for advanced ligo suspensions,” 2005. LIGO technical note, LIGO-T050206-00-K.
- [98] W.N. Findley et al., *Creep and Relaxation of Nonlinear Viscoelastic Materials*. Dover Publications, 1994.
- [99] B. Willke et al. *Class. Quantum Grav.*, vol. 21, pp. S417–S423, 2004.
- [100] S. Rowan 1999. Presentation at the Aspen Winter Conference on Gravitational Waves, available at www.ligo.caltech.edu/docs/G/G000069-00.pdf.
- [101] S. Reid, G. Cagnoli, D.R.M. Crooks, J. Hough, P. Murray, S. Rowan, M.M. Fejer, R. Route and S. Zappe *Phys. Lett. A*, vol. 351, no. 4-5, pp. 205–211, 2006.

- [102] M. Punturo and G. Cagnoli, “Report on WP1/M5: Status of the designing of monolithic suspensions,” 2007.
- [103] G. Cagnoli, “R&D on thermal noise in Europe: the STREGA Project,” *Journal of Physics: Conference Series*, vol. 32, pp. 294–300, 2006.
- [104] W. Winkler, K. Danzmann, A. Rüdiger and R. Schilling *Phys. Rev. A*, 1991. 7022.
- [105] P. Amico et al. *Class. Quantum Grav.*, vol. 21, pp. S1009–S1013, 2004.
- [106] S.M. Hu *J. Appl. Phys.*, vol. 53, p. 3576, 1982.
- [107] C.C. Lam and D.H. Douglas *Phys. Lett.*, vol. 85, p. 41, 1981.
- [108] D.F. McGuigan, C.C. Lam, R.Q. Gram, A.W. Hoffman, D.H. Douglas and H.W. Gutche *J. Low Temp. Phys.*, vol. 30, p. 621, 1978.
- [109] C.A. Swenson *J. Phys. Chem. Ref. Data*, vol. 12, p. 179, 1983.
- [110] C.Y. Ho, R.W. Powell and P.E. Liley *J. Phys. Chem. Ref. Data*, vol. 1, p. 279, 1972.
- [111] Material properties Database (MPDB). www.jahm.com.
- [112] S. Reid, *Studies of materials for future ground-based and space-based interferometric gravitational wave detectors*. PhD thesis, University of Glasgow, 2006.
- [113] P. Amico et al. *Nucl. Instrum. Meth. A*, vol. 518, pp. 240–243, 2004.
- [114] R.I. Epstein, M.I. Buchwald, B.C. Edwards, T.R. Gosnell and C.E. Mungan *Nature*, vol. 377, pp. 500–503, 1995.
- [115] B.C. Edwards, J.E. Anderson, R.I. Epstein, G.L. Mills and A.J. Mord *Journ. Appl. Phys.*, vol. 86, pp. 6489–6493, 1999.
- [116] S.R. Bowman and C.E. Mungan *Appl. Phys. B*, vol. 71, pp. 807–811, 2000.
- [117] T. Gosnell *Opt. Lett.*, vol. 24, pp. 1041–1043, 1999.
- [118] K. Numata, G. B. Bianc, M. Tanaka, S. Otsuka, K. Kawabe, M. Ando and K. Tsubono *Phys. Lett. A*, vol. 284, pp. 162–171, 2001.
- [119] J.E. Logan, N.A. Robertson, J. Hough and P.J. Veitch *Phys. Lett. A*, vol. 161, p. 101, 1991.

- [120] A. Bunkowski, O. Burmeister, K. Danzmann, R. Schnabel, T. Clausnitzer, E.-B. Kley and A. Tünnermann *Journal of Physics Conference Series*, vol. 32, p. 333, 2006.
- [121] J. Czochralski *Z. Phys. Chem.*, vol. 92, pp. 219–221, 1918.
- [122] M. Alshourbagy, P. Amico, L. Bosi, G. Cagnoli, E. Campagna, F. Cottone, A. Dari, L. Gammaitoni, M. Lorenzini, G. Losurdo, F. Marchesoni, F. Martelli, F. Piergiovanni, M. Punturo, A. Toncelli, M. Tonelli, F. Travasso, F. Vetrano and H. Vocca *Rev. Sci. Instrum.*, vol. 77, 2006. 044502-1.
- [123] G. Cagnoli, J. Kovalik, L. Gammaitoni, F. Marchesoni and M. Punturo *Phys. Lett. A*, vol. 213, pp. 245–252, 1996.
- [124] T.J. Quinn, C.C. Speake, W. Tew and R.S. Davis *Phys. Lett. A*, vol. 197, p. 197, 1995.
- [125] Y.L. Huang and P.R. Saulson *Rev. Sci. Instrum.*, vol. 69, p. 544, 1998.
- [126] P.M. Morse, *Vibration and Sound*. McGraw-Hill, New York, 1948.
- [127] A.G. Andreou, “Wet Etching, Lecture Notes from Wet Etching by R. Darling,” 2000. 520/580.495, www.engr.washington.edu/~cam/PROCESSES.
- [128] L.D. Landau and E.M. Lifshitz, *Theory of Elasticity*. Pergamon Press, Oxford, 1959.
- [129] www.cryogenics.nist.gov.
- [130] J.F. Nye, *Physical Properties of Crystals*. Clarendon Press, Oxford, 1957.
- [131] P. Chantrenne, J.L. Barrat, X. Blase and J.D. Gale *J. Appl. Phys.*, vol. 97, 2005. 104318-1.
- [132] T. Ruf et al. *Solid State Comm.*, vol. 115, no. 5, p. 243, 2000.
- [133] R.K. Kremer, K. Graf, G.G. Devyatikh, A.V. Gusev, A.M. Gibin, A.V. Inyushkin, A.N. Taldenkov and H.-J. Pohl *Solid State Comm.*, vol. 131, pp. 499–503, 2004.
- [134] A.V. Inyushkin *Inorg. Materials*, vol. 38, no. 5, pp. 427–433, 2002.
- [135] J. Callaway *Phys. Rev.*, vol. 113, no. 4, p. 1046, 1959.
- [136] M.G. Holland *Phys. Rev.*, vol. 132, no. 6, p. 2461, 1963.

- [137] Y.S. Touloukian and E.H. Buyco, *Thermophysical Properties of Materials*. Plenum, New York, 1970.
- [138] D. Gwo, “Ultra-Precision Bonding for Cryogenic Fused Silica Optics,” *Proceedings of SPIE*, p. 3435, 1998.
- [139] D. Gwo, “Hydroxide-Catalized Bonding,” *United States Patent no. US 6-548-176 B1*, 2003.
- [140] C.K.J.D. Mackenzie et al. *J. Mater. Sci.*, vol. 26, pp. 763–768, 1991.
- [141] P.H. Sneddon, S. Bull, G. Cagnoli, D.R.M. Crooks, E.J. Elliffe, J.E. Faller, M.M. Fejer, J.Hough and S. Rowan *Class. Quantum Grav.*, vol. 20, pp. 5025–5037, 2003.
- [142] S. Reid, G. Cagnoli, E.J. Elliffe, J. Faller, J. Hough, I. Martin and S. Rowan *Phys. Lett. A*, vol. 363, pp. 341–345, 2007.
- [143] E.J. Elliffe, J. Bogenstahl, A. Deshpande, J. Hough, C. Killow, S. Reid, D. Robertson, S. Rowan, H. Ward and G. Cagnoli *Class. Quantum Grav.*, vol. 22, pp. S257–S267, 2005.
- [144] S. Rowan, S.M. Twyford, J. Hough, D.H. Gwo and R. Route *Phys. Lett. A*, vol. 246, p. 471, 1998.
- [145] J.R. Smith, G. Cagnoli, D.R.M. Crooks, M.M. Fejer, S. Goßler, H. Lück, S. Rowan, J. Hough and K. Danzmann *Class. Quantum Grav.*, vol. 21, pp. S1091–S1098, 2004.
- [146] S. Reid , personal communication.
- [147] F. Travasso, “Review on Thermal Noise Related Activites in Perugia,” 2007.
www.ego-gw.it/ILIAS-GW/documents/Tubingen_talks/luned%EC/travasso.ppt.
- [148] S. Reid, “Silicate Bonding on Silicon and Silica,” 2007.
www.ego-gw.it/ILIAS-GW/documents/Tubingen_talks/luned%EC/reid.ppt.
- [149] D.H.J. Goodall, “Cryogenic Data,” 1970. A.P.T. Division, Culham Laboratory.